ISSN 1694-7398
journals.manas.edu.kg

April 2021
Volume 9, Special Issue 1

MANAS JOURNAL OF ENGINEERING

MJEN

Special Issue is dedicated to 25th Anniversary of the Establishment of Kyrgyz-Turkish Manas University

BISHKEK 2021

KYRGYZ TURKISH MANAS UNIVERSITY
MANAS JOURNAL OF ENGINEERING (MJEN)

ISSN: 1694- 7398
Year: 2021
Volume: 9
Special Issue: 1
http://journals.manas.edu.kg
journals@manas.edu.kg

PUBLICATION PERIOD

Manas Journal of Engineering (MJEN) is published twice year, MJEN is a peer reviewed journal.

CORRESPONDENCE ADDRESS
Kyrgyz Turkish Manas University
Chyngyz Aitmatov Avenue 56 Bishkek, KYRGYZSTAN
URL: http://journals.manas.edu.kg
e-mail: journals@manas.edu.kg
Tel : +996 312 492763- Fax: +996 312 541935

KYRGYZ TURKISH MANAS UNIVERSITY
MANAS JOURNAL OF ENGINEERING (MJEN)

CONTENT

MANAS Journal of Engineering
ISSN 1694-7398 | e-ISSN 1694-7398

Volume 9, Special Issue 1, (2021) Pages 1-9
https://doi.org/10.51354/mjen.804338

An optimization study for bio-removal of lead from aqueous environments by alkali modified *Polyporus Squamosus*

Şakir Yılmaz[1], Ümit Ecer[1,*], Tekin Şahan[1]

[1] Van Yuzuncu Yil University, Faculty of Engineering, Department of Chemical Engineering, 65080 Van, Turkey, umitecer@gmail.com, ORCID: 0000-0001-9797-0959, ORCID: 0000-0002-1824-982X, ORCID: 0000-0001-8776-9338

ABSTRACT

Rapidly increasing industrialization and urbanization cause serious environmental pollution. Discharge of polluting material from various industries such as smelting, mining, ore processing, and metal plating into the environment without treatment causes serious pollution and can have dangerous effects on the environmental balance. The utilization of low-cost adsorbents from biological materials as a replacement for costly traditional methods for adsorption of heavy metal pollutants from wastewater was reviewed. This study aimed to investigate the biosorption of Pb(II) ions from aqueous solutions with NaOH-modified Polyporus squamosus biosorbent and optimize the biosorption conditions. Firstly, the parameters most influencing the response of the biosorption for Pb(II) (initial Pb(II) concentration (C_o), pH, temperature and biomass dose) were determined using Central Composite Design (CCD). The optimum conditions were evaluated as 60.76 mg/L, 6.3, 25 °C, and 0.23 g for Co, initial pH, temperature and biomass dose, respectively. From the optimum conditions, the adsorption yield and the adsorption capacity were obtained as 93.8% and 23.63 mg/g, respectively.

ARTICLE INFO

Research article

Received: 02.11.2020
Accepted: 16.12.2020

Keywords:
biosorption,
lead,
polyporus squamosus,
response surface methodology

**Corresponding author*

1. Introduction

A disadvantage arising from rapidly increasing industrialization, the presence of toxic heavy metals in aqueous environments emerges as an environmental problem that needs to be solved worldwide. Heavy metals are toxic pollutants that pose a risk to life even at very low concentrations [1]. The most common heavy metals in industrial wastewater can be listed as lead, cadmium, mercury, copper and zinc. Among these heavy metals, lead is a common metal that must be removed from industrial wastewater, as it causes serious harm to the peripheral and central nervous system of humans [2]. The permitted drinking water standard for Pb is 10 µg/L according to the World Health Organization (WHO) and 50 µg/L according to the Environmental Protection Agency (EPA) [3]. Leaving the wastewater released by the use of lead in the industrial field to the environment without any treatment increases the lead pollution in natural water resources. Pb; it is one of the raw materials widely used in oil refineries, paint, photographic materials, and battery industry. Organic and inorganic lead contamination is encountered in battery factory wastewater (2.44 mg/L), gold mining (85 mg/L), and electroplating wastewater (11.9 mg/L) [4-6]. Therefore, lead must be removed before the wastewater can be discharged. Over the years, various methods have been used and proposed to remove heavy metals present in wastewater. The most common removal methods are coagulation, chemical precipitation, reverse osmosis, ion exchange, and adsorption/biosorption. However, each of these technologies has its disadvantages, such as high-energy requirements, production of undesirable secondary pollution, incomplete removal, low efficiency, and high costs [7, 8]. These disadvantages show that biosorption as a serious alternative technology. Biosorption is the removal of pollutants from aqueous environments using biological material [9]. Therefore, the biosorption process is increasingly considered as a potential alternative way to remove industrial pollutants. Biosorption of heavy metals onto various microbial biomasses such as fungi, algae and bacteria has been widely studied [10, 11]. The removal potential for heavy metals in industrial wastewater using biological materials is increasingly reported from different parts of the world [10, 12, 13]. Among the biological materials, fungi are one of the most frequently used biosorbents in recent years. Fungi have high potential for use in heavy metal removal due to their high surface area, abundance in nature, and being both economic and

environmentally friendly. Due to all these advantages, fungi have high importance in the treatment of wastewater [14]. Traditionally, it is difficult to observe the simultaneous effect of factors that influence a response, which requires additional experiments. With the traditional methods, one parameter is changed, while others are kept at a constant level [15, 16]. Response Surface Methodology (RSM) is the most satisfying optimization method used by researchers recently with various technologies. This method contains a collection of mathematical and statistical techniques that are beneficial for developing, optimizing, and improving processes. RSM can determine the influence of independent factors either individually or in combination with a process and is able to decrease the number of experiments necessary to analyze the process statistically for a range of factors [17]. RSM basically creates a mathematical model based on the results obtained from experimental data. It is a strong optimization tool which optimizes process conditions [14, 18]. Central composite design (CCD) in RSM with the help of Design Expert Version 7.0 (Stat Ease, USA) was used for this purpose. The statistical design can help to clarify the interaction of the various factors and define the optimum condition of the factors for biosorption/ adsorption [19]. CCD is optimal for sequential trials and provides an adequate amount of data for testing lack of fit while not confusing uncommonly large number of design points.

Due to the serious harmful effects of water contamination by heavy metals, there is an urgent need to find effective methods to eliminate such contamination. This study aimed to determine the optimum conditions for Pb(II) adsorption by NaOH treated *Polyporus squamosus*, a novel biosorbent, from aqueous solutions. For this purpose, naturally abundant and low cost *Polyporus squamosus* was modified with NaOH to enhancement adsorption affinity for Pb(II) ions compared to pure *Polyporus squamosus*. The effect of independent variables (initial Pb(II) concentration (C_o, mg/L), pH, temperature (°C) and biosorbent amount (g)) were examined and optimized using central composite design (CCD). RSM, a statistical and mathematical method used to optimize the biosorption conditions, offers many advantages in terms of time and cost. Also, it supplies more data, tables, and diagrams with very few experiments.

2. Materials and methods

2.1 Materials

2.1.1 Raw biosorbent

Natural *P. Squamosus* fungi (*(Huds.) Fr.*) was collected from the Yüksekova area in Eastern Turkey. *P. Squamosus* fungi were washed with deionized water to remove impurities before use as biosorbent. The biomass was then dried at 60 °C and ground with a mill. It was sieved to select particles of 125 µm size and then stored in a desiccator to be treated with NaOH on the surface.

2.1.2 Chemical modification of P. Squamosus biosorbent

For the modification process, a certain amount of the P. *Squamosus* powder prepared previously was weighed (50 g) and treated with 500 mL of 0.1 M sodium hydroxide (NaOH) solution overnight. Then the slurry was filtered and washed with distilled water. The residues were then dried at 90 ˚C overnight and used for adsorption experiments.

2.1.3. Pb(II) biosorption experiment

Stock solution of Pb(II) was prepared by dissolving a certain amount of analytical grade $Pb(NO_3)_2$ (purity ≥ 99, Sigma-Aldrich) in deionized water. The initial solution pH was set by using 0.1M NaOH and HNO_3 solutions previously available for this purpose. All tests were performed in Erlenmeyer flasks containing 100 mL of Pb (II) solution with a temperature-controlled magnetic stirrer. Biosorption experiments were completed under different conditions including initial concentration (Co, 10–100 mg/L), initial pH (2–7.5), temperature (20-50 °C) and biomass amount (0.05-0.4 g). Samples taken after the desired contact period were filtered with a filter paper (Whatman No. 42) to remove the biosorbent. After biosorption for all solutions, the concentration of un-biosorbed Pb(II) in residual solutions were determined by utilizing an Atomic Absorption Spectrometer (AAS) (THERMO Solar AA Series spectrometer, USA). The removal percentages and adsorption amounts were calculated using Eqs. 1 and 2, respectively.

$$\%\ Biosorption = \frac{(C_o - C_e)}{C_o} \times 100 \quad (1)$$

$$q_e = \frac{(C_i - C_e)\ V}{W} \quad (2)$$

where, q_e is the Pb(II) biosorption capacity (mg/g), C_i is initial and C_e is equilibrium concentration (mg/L), respectively, W is the biosorbent amount (g) and V is the volume of the solution (L).

2.1.4 Experimental design for biosorption studies

Four independent parameters (C_o, initial pH, temperature and biomass amount) were determined for the biosorption optimization of Pb(II) with NaOH-modified P. *Squamosus*. The relationship between these independent parameters and response was determined using CCD in the RSM. The total number of experiments (N) was determined by Eq. 3. Four independent parameters were designed with 3 coded values (-1, 0, +1). The actual levels and ranges are given in Table 1. The obtained experimental data were subjected to the following quadratic model to estimate the response (Eq. 4).

$$N = 2^k + 2k + 6 \quad (3)$$

$$y_p = \beta_o + \sum_{i=1}^{4} \beta_i x_i + \sum_{i=1}^{4} \beta_{ii} x_i^2 + \sum_{i=1}^{4} \sum_{j=i+1}^{4} \beta_{ij} x_i x_j \quad (4)$$

where, k is the number of independent parameters, y_p is the response, β_0 is constant, β_i is linear, β_{ii} is quadratic, and β_{ij} is interaction coefficients. x_i (i=1-4) are the independent parameters.

Table 1. *Levels of parameters for CCD experiments.*

Independent parameters	Unit	Coded	Coded and un-coded values		
			-1	0	+1
Initial conc. (C_o)	mg/L	X_1	10	55	100
Initial pH		X_2	2	4.75	7.5
Temperature (T)	°C	X_3	20	35	50
Biomass amount (m)	g	X_4	0.05	0.225	0.40

3. Results and discussion

3.1. RSM modelling and ANOVA analysis

The effect of independent parameters (C_o, initial pH, temperature, and biomass amount) on the biosorption amount was examined and optimized in a batch system. The purpose of optimization with CCD is to determine the interaction between parameters affecting the response with fewer experiments and thus to easily assign the optimum values of the parameters. For the optimization of Pb(II) biosorption, 30 batch experiments were performed and the obtained responses (amount of biosorption) are given in Table 2. Second-order regression models (with and without code) obtained from CCD for Pb (II) biosorption are given in Eqs. 4 and 5.

Table 2. *Experimental response for CCD of Pb(II) ion removal.*

Run	X_1	X_2	X_3	X_4	Biosorbed Pb(II) amount (mg/g) (Observed)	Biosorbed Pb(II) amount (mg/g) (Predicted)	ε (Predicted-Observed)
1	10 *(-1)*	2 *(-1)*	50 *(+1)*	0.05 *(-1)*	1.42	0.889	-0.531
2	10 *(-1)*	2 *(-1)*	20 *(-1)*	0.4 *(+1)*	0.129	0.588	0.459
3	55 *(0)*	7.5 *(+1)*	35 *(0)*	0.225 *(0)*	23.62	24.962	1.342
4	55 *(0)*	4.75 *(0)*	35 *(0)*	0.225 *(0)*	23.15	21.201	-1.949
5	55 *(0)*	4.75 *(0)*	20 *(-1)*	0.225 *(0)*	23.24	21.834	-1.405
6	100 *(+1)*	2 *(-1)*	50 *(+1)*	0.05 *(-1)*	1.243	1.643	0.401
7	100 *(+1)*	7.5 *(+1)*	50*(+1)*	0.05 *(-1)*	16.75	18.201	1.459
8	10 *(-1)*	2 *(-1)*	20 *(-1)*	0.05 *(-1)*	3.68	2.791	-0.889
9	55 *(0)*	4.75 *(0)*	35 *(0)*	0.225 *(0)*	23.15	23.788	0.638
10	10 *(-1)*	2 *(-1)*	50 *(+1)*	0.4 *(+1)*	3.48	2.272	-1.207
11	100 *(+1)*	2 *(-1)*	20 *(-1)*	0.05 *(-1)*	1.432	1.284	-0.147
12	55 *(0)*	4.75 *(0)*	35 *(0)*	0.225 *(0)*	23.09	24.244	1.154
13	10 *(-1)*	7.5 *(+1)*	20 *(-1)*	0.05 *(-1)*	18.62	20.822	2.203
14	100 *(+1)*	2 *(-1)*	50 *(+1)*	0.4 *(+1)*	2.451	0.857	-1.593
15	10 *(-1)*	4.75 *(0)*	35 *(0)*	0.225 *(0)*	9.74	9.029	-0.710
16	55 *(0)*	4.75 *(0)*	35 *(0)*	0.225 *(0)*	23.52	24.303	0.783
17	100 *(+1)*	7.5 *(+1)*	50 *(+1)*	0.4 *(+1)*	16	13.681	-2.318
18	10 *(-1)*	7.5 *(+1)*	20 *(-1)*	0.4 *(+1)*	2.29	4.604	2.314
19	100 *(+1)*	2 *(-1)*	20 *(-1)*	0.4 *(+1)*	1.76	2.605	0.845
20	100 *(+1)*	4.75 *(0)*	35 *(0)*	0.225 *(0)*	23.08	22.230	-0.849
21	10 *(-1)*	7.5*(+1)*	50 *(+1)*	0.4 *(+1)*	2.287	2.483	0.196
22	55 *(0)*	4.75*(0)*	35 *(0)*	0.05 *(-1)*	21.45	21.248	-0.201
23	100 *(+1)*	7.5 *(+1)*	20 *(-1)*	0.05 *(-1)*	14.74	15.647	0.907
24	55 *(0)*	4.75 *(0)*	50 *(+1)*	0.225 *(0)*	22.84	21.928	-0.911
25	55 *(0)*	4.75 *(0)*	35 *(0)*	0.225 *(0)*	23.01	23.023	0.013
26	55 *(0)*	4.75 *(0)*	35 *(0)*	0.225 *(0)*	22.78	22.793	0.013
27	10 *(-1)*	7.5 *(+1)*	50 *(+1)*	0.05 *(-1)*	18.34	18.332	-0.008
28	55 *(0)*	2 *(-1)*	35 *(0)*	0.225 *(0)*	16.57	16.716	0.146
29	55 *(0)*	4.75 *(0)*	35 *(0)*	0.4 *(+1)*	13.05	13.013	-0.036
30	100 *(+1)*	7.5 *(+1)*	20 *(-1)*	0.4 *(+1)*	15	14.880	-0.119

$$\text{Biosorbed Amount (mg/ g)(uncoded)} = -11.15221 + 0.27816[C_o] + 5.98277[pH] - 0.017148[T] + 73.25179[m] + 0.011503[C_o][pH] + 2.50370\,E\text{-}004[C_o][T] + 0.27714[C_o][m] + 1.71818\,E\text{-}003[pH][T] - 4.27506[pH][m] + 0.13710[T][m] - 3.30759\,E\text{-}003[C_o]^2 - 0.39839[pH]^2 - 3.01598\,E\text{-}004[T]^2 - 191.27705[m]^2 \quad (4)$$

$$\text{Biosorbed Amount (mg / g)(coded)} = +23.11+1.80[X_1]+5.30[X_2]+0.22[X_3]-2.29[X_4]+1.42[X_1X_2]+0.17[X_1X_3] +2.18[X_1X_4]+0.071[X_2X_3]-2.06[X_2X_4]+0.36[X_3X_4]-6.70[X_1]^2 -3.01[X_2]^2 -0.068[X_3]^2 -5.86[X_4]^2 \quad (5)$$

Analysis of variance (ANOVA) was used to verify the significance of the second-order regression model obtained. ANOVA for regression parameters of the quadratic model obtained from CCD for the biosorption of Pb (II) on NaOH-P. *squamosus* is presented in Table 3. The *prob* > *F* (>0.0001) value shows that the second-order quadratic model is significant. The high value of the coefficient of determination (R^2 = *0.947*) indicates that 94.7% of the variability in the response is explained by the model [20]. *p*-value was employed to identify the significance of terms, which are considered as significant to the predicted response when $p < 0.05$. From the ANOVA result, X_1, X_2, X_4 (linear terms), X_1X_4, X_2X_4 (interaction terms), X_1^2, and X_4^2 (quadratic terms) were significant ($p < 0.05$) for the predicted response. The other terms in Table 3 have little effect on the model equation, but even these effects are important [21].

Table 3. *Analysis of variance regression model for Pb(II) biosorption by using NaOH-modified Polyporus squamosus.*

Source	Sum of Squares	df	Mean Square	F Value	p-value Prob > F	
Model	2287.220939	14	163.3729242	19.05933073	< 0.0001	**significant**
X_1-Initial conc.	58.57227222	1	58.57227222	6.833129256	0.0195	
X_2-pH	506.4895736	1	506.4895736	59.08783443	< 0.0001	
X_3-Temperature	0.853688889	1	0.853688889	0.099592628	0.7567	
X_4-Biomass Amount	94.43044356	1	94.43044356	11.01639739	0.0047	
X_1X_2	32.421636	1	32.421636	3.782356755	0.0708	
X_1X_3	0.456976	1	0.456976	0.053311507	0.8205	
X_1X_4	76.2129	1	76.2129	8.89111139	0.0093	
X_2X_3	0.08037225	1	0.08037225	0.009376347	0.9241	
X_2X_4	67.72467025	1	67.72467025	7.900861758	0.0132	
X_3X_4	2.07216025	1	2.07216025	0.241741327	0.6301	
X_1^2	116.2316119	1	116.2316119	13.55975443	0.0022	
X_2^2	23.51851937	1	23.51851937	2.743705796	0.1184	
X_3^2	0.01193096	1	0.01193096	0.001391884	0.9707	
X_4^2	88.90580096	1	88.90580096	10.37188428	0.0057	

Figure 1a shows normal % probability versus residuals. The normal probability plot is a graphical technique to identify whether or not a data set is approximately normally distributed. Since the points on the graph are observed as a

straight line, it can be concluded that the residuals are normally distributed and data transformation is not required. For this reason, it was concluded that the estimation of the experimental data obtained from the second-order model was quite significant [22]. Generally, it is important to check that the proposed model provides an adequate approach to the actual system. If the recommended model does not show sufficient fit, examination, and optimization of the fitted response surface is likely to give misleading results. Residuals play a significant role in evaluating model adequacy. Figure 1b shows that the residuals were randomly distributed between ± 3. It can be concluded that the results obtained are compatible with the experimental data estimated using the quadratic equation.

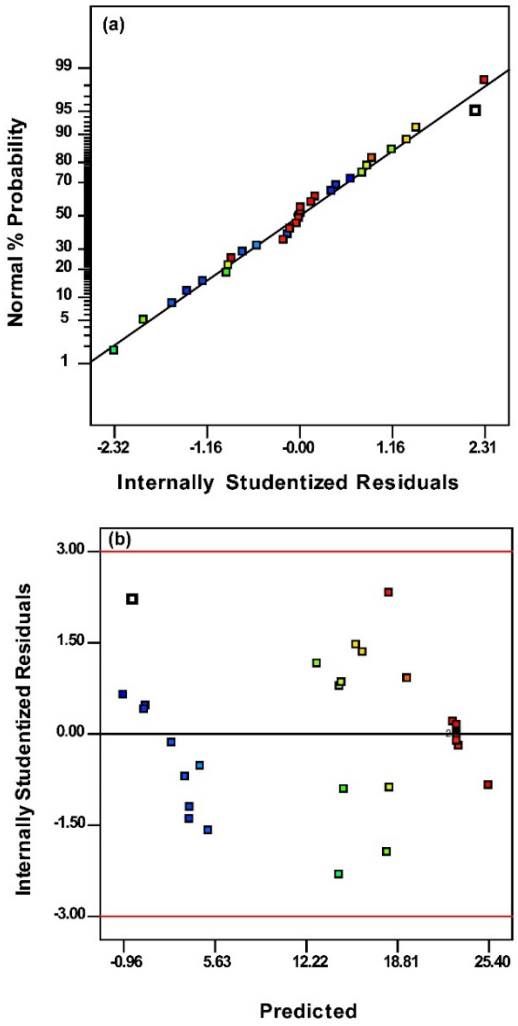

Figure 1 *a) Validation of the prediction of Pb(II) biosorption residuals versus normal % probability and b) Residuals versus predicted values.*

3.2. Effects of process variables on biosorption capacity

Initial pH and Co play a significant role in the biosorption process of heavy metal ions (Figure 2). In this work, the biosorption of Pb(II) ions on NaOH-*P. squamosus* was studied at different pH levels ranging from 2.0 to 7.5. Removal of Pb (II) ions increased by increasing initial pH from 2.0 to 6.0 (Figure 2a). With the initially increasing pH, the active binding sites on the surface of NaOH-*P. squamosus* become negatively charged and electrostatic attraction occurs between the positively-charged Pb (II) ions and these negatively-charged groups. This conclusion can be demonstrated as the reason for the increase in Pb(II) adsorption. When the initial pH was approximately 6.5, more than 90% of the Pb(II) ions in solution were biosorbed by NaOH-*P. squamosus*. The decrease in Pb (II) biosorption at increasing initial pH values can be attributed to the separation of functional groups on NaOH-*P. squamosus* and the change in surface charge. One of the most significant reasons for this is that Pb(II) ions can precipitate as $Pb(OH)_2$ solid that does not dissolve at high pH [18]. The solution pH not only affects the charges on the adsorbent surface but also affects the ionization of the solute or inhibits ions. Therefore, initial metal solution pH values that are too high should be avoided as they may cause the precipitation of metal complexes and interfere with the separation between adsorption and precipitation [23, 24].

Adsorption experiments were conducted for various Pb(II) concentrations ranging from 10 to 100 mg/L using NaOH-*P. squamosus* to study the influence of C_o on biosorption. The results given in Figure 2a show that Pb(II) biosorption increased with rising C_o. The biosorption capacity of NaOH-*P. squamosus* quickly increased by increasing C_o from 10 to 55 mg/L while no change was recorded at higher initial Pb(II) concentrations and a maximum level was approximately reached at 60.0 mg/L. These results show that the pores of NaOH-*P. squamosus* were completely full after a particular period and after that, increasing the metal concentration didn't have a significant effect on biosorption of Pb(II) ions [25, 26]. In addition, the rapid adsorption in the first stage may be due to the presence of a larger surface area, but the adsorption rate decreases due to the occupation of surface areas after adsorption begins [27].

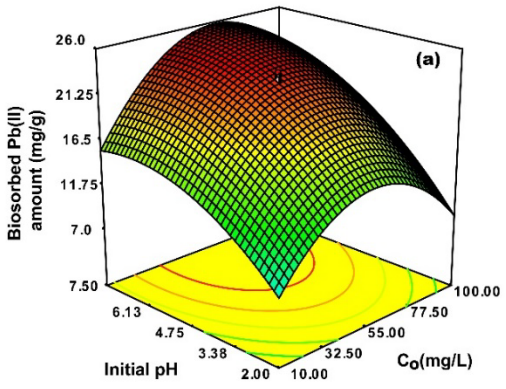

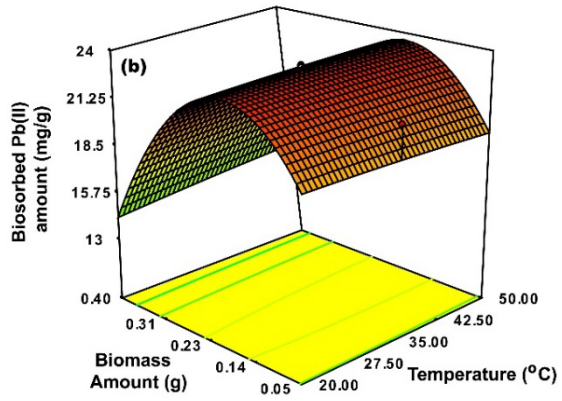

Figure 2. *Simultaneous effects of a) initial concentration (C_o) and initial pH and b) temperature and biomass dosage on Pb(II) biosorption*

The biomass amount is another important parameter, which influences the extent of removal from the solution, and so the effect as shown in Figure 2b. The increase in the dosage of the adsorbent is very effective in heavy metal adsorption. Results obtained from this study describe the adsorption of Pb(II) which increases rapidly when the dose of NaOH-*P. squamosus* powder is increased from 0.04 to 0.5 g; further explained by the large availability of surface area at higher concentrations of adsorbent. This study showed that the optimum biosorbent dose required for maximum adsorption was 0.22 g. Above the optimum amount, the removal efficiency did not change with increasing biomass amount. As expected, the adsorption yield increased by increasing the biomass amount for a given Co, because, for constant Co, increasing biomass amount supplies a larger surface area or more biosorption sites. On the other hand, when the biomass amount increased, the amount adsorbed per unit mass of biosorbent decreased. The reduction in biosorption capacity with a rise in the biomass amount is substantially due to the increase in free biosorption sites for the biosorption reaction [28, 29].

One of the important parameters in biosorption processes is temperature. According to the biosorption theory, adsorption is reduced as molecules adsorbed on the surface at high temperatures tend to desorb from the surface [30]. This work was carried out over a temperature range of 20 °C to 50 °C. The optimum temperature was found to be 20 °C, as shown in Figure 2b. The results obtained show that the increased temperature had an adverse effect on the biosorption capacity. Based on that fact, one may say that Pb(II) biosorption by NaOH-*P. squamosus* is an exothermic process [10, 31].

3.3. Determination of Optimum Biosorption Conditions

For the optimization procedure, the numerical optimization operation in RSM was used to determine optimum conditions for Pb(II) biosorption onto NaOH-*P. squamosus*. With numerical optimization, the optimum values for the response and independent parameters can be identified. For this, each parameter can be selected in the target, minimum, maximum, or range in order to achieve an optimal output for a set of conditions. The main goal to be achieved in the optimization process is to determine the optimum points of the parameters that affect Pb (II) removal by NaOH-*P. squamosus*. While the response was selected as "maximize" to reach the highest value, the independent variables were arranged according to the entire studied range. The optimum values were determined as 60.76 mg/L, 6.3, 25 °C, and 0.23 g for C_o, pH, T (°C), and biomass dosage (g), respectively, and these values were confirmed by obtained data. Under these optimum conditions, the maximum biosorbed Pb(II) amount was found to be 25.68 mg/g and biosorption yield was calculated to be 97.23%. To confirm the validity of the proposed model equation for Pb(II) biosorption by NaOH-*P. squamosus*, several tests were made with the optimum conditions obtained by the program. Based on the experimental results, biosorbed Pb(II) amount was obtained to be 24.39 mg/g, indicating that this result was fairly close to the predicted value obtained by the model at the optimum points.

The comparison between the biological material we used and some materials used in the literature is shown in Table 4. It can be said that NaOH-*P. squamosus* is a natural biosorbent with higher sorption capability than some other biosorbents/adsorbents. In addition, NaOH-*P. squamosus* waste does not pollute the environment after the biosorption process. Due to these properties, it is a biosorbent with high potential to remove heavy metals from aqueous environments. In order to understand the importance of the modification process, experiments were carried out using pure *P. squamosus* under the optimum conditions obtained. Under these conditions, the maximum amount of biosorbed Pb(II) was 12.68 mg/g. In addition, the biosorption efficiency was calculated as 67.23%. These results show that NaOH-modified *P. squamosus* significantly increased the removal of Pb(II) ions.

Table 4. *Comparison of biosorption capacity of NaOH-P. squamosus for Pb(II) ions with different biosorbents/adsorbents*

Biosorbent / Adsorbent	%Pb(II) adsorption / biosorption	Pb(II) adsorption / biosorption amount	Ref.
P. squamosus	89.4	13.65	[10]
Activated carbon prepared from coconut shell	96	26.5	[32]
Litchi pericarp	99.97	163.93	[33]
Banana peels	85.3	2.18	[7]
Pumice	88.49	7.46	[34]
MWCNTs	75.3	91	[35]
Oryza sativa L. husk	98.11	8.60	[36]
NaOH-*P. squamosus*	97.23	25.68	This work

4. Conclusions

In this study, the effects of the initial conc.(C_o), initial pH, temperature and biomass amount on removal were investigated using CCD in RSM for biosorption of Pb(II) from wastewater on NaOH-*P. squamosus*. The results indicated a high correlation among the predicted and experimental values. With the quadratic model obtained from CCD, the optimum biosorption conditions were determined as initial Pb(II) concentration 60.76 mg/L, initial pH 6.3, temperature 25 °C and biomass amount 0.23 g. At these optimum conditions, the optimum biosorbed Pb(II) amount and biosorption yield were found to be 25.68 mg/g and 97.23%, respectively. In addition, the adsorption capacity of *P. squamosus* modified with NaOH increased significantly compared to pure *P. squamosus*. Accordingly, the present results indicate that NaOH-*P. squamosus* is a green technology can be used for the biosorption of heavy metals from wastewater.

Acknowledgments

We would like to thank Prof. Dr. Yusuf Uzun (Van Yuzuncu Yil University) for providing the biosorbent used in this study.

References

[1]. Garg U., Kaur M.P., Jawa G.K., Sud D., Garg V.K., "Removal of cadmium (II) from aqueous solutions by adsorption on agricultural waste biomass", Journal of Hazardous Materials, 154, (2008), 1149-1157.

[2]. Liao S.-W., Lin C.-I., Wang L.-H., "Kinetic study on lead (II) ion removal by adsorption onto peanut hull ash", Journal of the Taiwan Institute of Chemical Engineers, 42, (2011), 166-172.

[3]. Gupta V.K., Ali I., "Removal of lead and chromium from wastewater using bagasse fly ash—a sugar industry waste", Journal of Colloid and Interface Science, 271, (2004), 321-328.

[4]. Poonam, Bharti S.K., Kumar N., "Kinetic study of lead (Pb2+) removal from battery manufacturing wastewater using bagasse biochar as biosorbent", Applied Water Science, 8, (2018), 119.

[5]. Yahya M.D., Yohanna I., Auta M., Obayomi K.S., "Remediation of Pb (II) ions from Kagara gold mining effluent using cotton hull adsorbent", Scientific African, 8, (2020), e00399.

[6]. Kara A., Üstün G.E., Akal Solmaz S.K., Demirbel E., "Removal of Pb(II) Ions in Fixed-Bed Column from Electroplating Wastewater of Bursa, an Industrial City in Turkey", Journal of Chemistry, 2013, (2013), 953968.

[7]. Anwar J., Shafique U., Waheed uz Z., Salman M., Dar A., Anwar S., "Removal of Pb(II) and Cd(II) from water by adsorption on peels of banana", Bioresource Technology, 101, (2010), 1752-1755.

[8]. Yang X., Zhao Z., Yu Y., Shimizu K., Zhang Z., Lei Z., Lee D.-J., "Enhanced biosorption of Cr(VI) from synthetic wastewater using algal-bacterial aerobic granular sludge: Batch experiments, kinetics and mechanisms", Separation and Purification Technology, 251, (2020), 117323.

[9]. Coday B.D., Xu P., Beaudry E.G., Herron J., Lampi K., Hancock N.T., Cath T.Y., "The sweet spot of forward osmosis: Treatment of produced water, drilling wastewater, and other complex and difficult liquid streams", Desalination, 333, (2014), 23-35.

[10]. Ecer U., Şahan T., "A response surface approach for optimization of Pb (II) biosorption conditions from aqueous environment with Polyporus squamosus fungi as a new biosorbent and kinetic, equilibrium and thermodynamic studies", Desalination and Water Treatment, 102, (2018), 229-240.

[11]. Li X., Xu H., Gao B., Shi X., Sun Y., Wu J., "Efficient biosorption of Pb(II) from aqueous solutions by a PAH-degrading strain Herbaspirillum chlorophenolicum FA1", Journal of Industrial and Engineering Chemistry, 57, (2018), 64-71.

[12]. Bano A., Hussain J., Akbar A., Mehmood K., Anwar M., Hasni M.S., Ullah S., Sajid S., Ali I., "Biosorption of heavy metals by obligate halophilic fungi", Chemosphere, 199, (2018), 218-222.

[13]. Shi L., Deng X., Yang Y., Jia Q., Wang C., Shen Z., Chen Y., "A Cr (VI)-tolerant strain, Pisolithus sp1, with a high accumulation capacity of Cr in mycelium and highly efficient assisting Pinus thunbergii for phytoremediation", Chemosphere, 224, (2019), 862-872.

[14]. Şahan T., Ceylan H., Şahiner N., Aktaş N., "Optimization of removal conditions of copper ions from aqueous solutions by Trametes versicolor", Bioresource Technology, 101, (2010), 4520-4526.

[15]. Karri R.R., Sahu J.N., "Modeling and optimization by particle swarm embedded neural network for adsorption of zinc (II) by palm kernel shell based activated carbon

from aqueous environment", Journal of Environmental Management, 206, (2018), 178-191.

[16]. Şahan T., "Application of RSM for Pb(II) and Cu(II) adsorption by bentonite enriched with SH groups and a binary system study", Journal of Water Process Engineering, 31, (2019), 100867.

[17]. Jaafari J., Yaghmaeian K., "Optimization of heavy metal biosorption onto freshwater algae (Chlorella coloniales) using response surface methodology (RSM)", Chemosphere, 217, (2019), 447-455.

[18]. Ecer Ü., Yılmaz Ş., Şahan T., "Highly efficient Cd(II) adsorption using mercapto-modified bentonite as a novel adsorbent: an experimental design application based on response surface methodology for optimization", Water science and technology : a journal of the International Association on Water Pollution Research, 78, (2018), 1348-1360.

[19]. Chowdhury S., Chakraborty S., Saha P.D., "Response surface optimization of a dynamic dye adsorption process: a case study of crystal violet adsorption onto NaOH-modified rice husk", Environmental Science and Pollution Research, 20, (2013), 1698-1705.

[20]. Mona S., Kaushik A., Kaushik C.P., "Biosorption of reactive dye by waste biomass of Nostoc linckia", Ecological Engineering, 37, (2011), 1589-1594.

[21]. Peng Y., Sun Y., Sun R., Zhou Y., Tsang D.C.W., Chen Q., "Optimizing the synthesis of Fe/Al (Hydr)oxides-Biochars to maximize phosphate removal via response surface model", Journal of Cleaner Production, 237, (2019), 117770.

[22]. Hasan S.H., Srivastava P., Talat M., "Biosorption of Pb(II) from water using biomass of Aeromonas hydrophila: Central composite design for optimization of process variables", Journal of Hazardous Materials, 168, (2009), 1155-1162.

[23]. Kubilay Ş., Gürkan R., Savran A., Şahan T., "Removal of Cu(II), Zn(II) and Co(II) ions from aqueous solutions by adsorption onto natural bentonite", Adsorption, 13, (2007), 41-51.

[24]. Ahmed Z., Wu P., Jiang L., Liu J., Ye Q., Yang Q., Zhu N., "Enhanced simultaneous adsorption of Cd(II) and Pb(II) on octylamine functionalized vermiculite", Colloids and Surfaces A: Physicochemical and Engineering Aspects, 604, (2020), 125285.

[25]. Forghani M., Azizi A., Livani M.J., Kafshgari L.A., "Adsorption of lead(II) and chromium(VI) from aqueous environment onto metal-organic framework MIL-100(Fe): Synthesis, kinetics, equilibrium and thermodynamics", Journal of Solid State Chemistry, 291, (2020), 121636.

[26]. Menezes J.M.C., da Silva Bento A.M., da Silva J.H., de Paula Filho F.J., da Costa J.G.M., Coutinho H.D.M., Pereira Teixeira R.N., "Equilibrium, kinetics and thermodynamics of lead (II) adsorption in bioadsorvent composed by Caryocar coriaceum Wittm barks", Chemosphere, 261, (2020), 128144.

[27]. Idris M.N., Ahmad Z.A., Ahmad M.A., "Adsorption equilibrium of malachite green dye onto rubber seed coat based activated carbon", Int J Basic Appl Sci, 11, (2011), 38-43.

[28]. Mousavi H., Hosseynifar A., Jahed V., Dehghani S., "Removal of lead from aqueous solution using waste tire rubber ash as an adsorbent", Brazilian Journal of Chemical Engineering, 27, (2010), 79-87.

[29]. Gapusan R.B., Balela M.D.L., "Adsorption of anionic methyl orange dye and lead(II) heavy metal ion by polyaniline-kapok fiber nanocomposite", Materials Chemistry and Physics, 243, (2020), 122682.

[30]. Bhatti H.N., Khalid R., Hanif M.A., "Dynamic biosorption of Zn(II) and Cu(II) using pretreated Rosa gruss an teplitz (red rose) distillation sludge", Chemical Engineering Journal, 148, (2009), 434-443.

[31]. Albalasmeh A., Gharaibeh M.A., Mohawesh O., Alajlouni M., Quzaih M., Masad M., El Hanandeh A., "Characterization and Artificial Neural Networks Modelling of methylene blue adsorption of biochar derived from agricultural residues: Effect of biomass type, pyrolysis temperature, particle size", Journal of Saudi Chemical Society, 24, (2020) 811-823.

[32]. Sekar M., Sakthi V., Rengaraj S., "Kinetics and equilibrium adsorption study of lead(II) onto activated carbon prepared from coconut shell", Journal of Colloid and Interface Science, 279, (2004), 307-313.

[33]. Sun S., Yang J., Li Y., Wang K., Li X., "Optimizing adsorption of Pb(II) by modified litchi pericarp using the response surface methodology", Ecotoxicology and Environmental Safety, 108, (2014), 29-35.

[34]. Şahan T., Öztürk D., "Investigation of Pb(II) adsorption onto pumice samples: application of optimization

method based on fractional factorial design and response surface methodology", Clean Technologies and Environmental Policy, 16, (2014), 819-831.

[35]. Wang H., Zhou A., Peng F., Yu H., Yang J., "Mechanism study on adsorption of acidified multiwalled carbon nanotubes to Pb(II)", Journal of Colloid and Interface Science, 316, (2007), 277-283.

[36]. Zulkali M.M.D., Ahmad A.L., Norulakmal N.H., "Oryza sativa L. husk as heavy metal adsorbent: Optimization with lead as model solution", Bioresource Technology, 97, (2006), 21-25.

Desalination and Water Treatment

MANAS Journal of Engineering
ISSN 1694-7398 | e-ISSN 1694-7398

Volume 9, Special Issue 1, (2021) Pages 10-23
https://doi.org/10.51354/mjen.807409

Exergy analysis of petroleum refinery hydrogen network integration based on reaction system

Ozben Kutlu[1,*], Fatma Zehra Ozcelik[2]

[1] Institute of Solar Energy, Ege University, 35100, Bornova, Izmir, Turkey, ozben.kutlu@ege.edu.tr, ORCID: 0000-0002-0361-6949

[2] Chemical Engineering Department, Ege University, 35100, Bornova, Izmir, Turkey, zehra.ozcelik@ege.edu.tr, ORCID: 0000-0001-9470-4161

ABSTRACT

High-purity hydrogen is a crucial input in a crude oil refinery to upgrade several products. For this reason, the effective hydrogen management is necessary to satisfy hydrogen requirements. On the other hand, adding exergy analysis to the hydrogen pinch analysis especially for refinery plants, where hydrogen reacts under high temperature and pressure, helps improve the efficiency of unit by overcoming the lack of pinch analysis. The aim of this study is the simulation and exergy analysis of reactors within hydrogen network integration of a petroleum refinery retrofitted by pinch analysis before. Two hydrogen production and four consumption units were considered and simulated by Aspen Plus, and then the exergy efficiencies were calculated. Low exergy efficiencies were determined in the hydrogen production and hydrodesulfurization units, whereas the separation of excess hydrogen from the desired product considerably effected on the efficiency. The results also show that not only the hydrogen demand of reactors has to be reduced, but also the hydrogen recovery and purification is very important for the increase in efficiency. Although the processes are carried out at the high operating conditions, the reactions significantly affect the total exergy flow rate

ARTICLE INFO

Research article

Received: 08.10.2020
Accepted: 25.02.2021

Keywords:
exergy,
hydrogen network,
petroleum refinery,
modeling and simulation

*Corresponding author

Nomenclature

C	carbon
$C_{12}H_{22}$	bicyclohexyl
$C_{12}H_8S$	dibenzothiophene
C_2H_6	ethane
C_2H_6S	ethyl-mercaptans
$C_2H_6S_2$	dimethyl-disulfide
C_3H_8	propane
C_4H_{10}	butane
C_4H_4S	thiophene
C_4H_8	cyclobutane
C_5H_{10}	cyclopentane
C_5H_{12}	pentane
C_6H_{12}	methyl-cyclopentane or cyclohexane
C_6H_{14}	2-methyl-pentane or 2,3-dimethyl-butane
C_6H_6	benzene
C_7H_{14}	methyl-cyclohexane
C_7H_{16}	heptane
C_8H_{16}	ethyl-cyclohexane
C_8H_{18}	octane
C_8H_6S	benzothiophene
CH_4	methane
CO	carbonmonoxide
CO_2	carbondioxide
H_2	hydrogen
H_2O	water
H_2S	hydrogen sulphide
$\dot{E}$	exergy rate (kJ)
$\dot{H}$	enthalpy rate (kJ)
$\dot{S}$	entropy rate (kJ)
$\dot{m}$	mass flow rate (kg/s)
$\bar{e}^{ch}$	standard chemical exergy (kJ/kg)
x	mole fraction

Subscripts

0	reference conditions
k	component
ch	chemical
ph	physical

Acronyms

ISO	isomerization
NHT	naphtha hydrotreating

CCR continuous catalytic reformer
SMR steam–methane reforming
SSR semi-regen reformer
HDS hydrodesulfurization
HC hydrocracker
LVGO light vacuum gas oil
HVGO heavy vacuum gas oil
LPG liquefied petroleum gas

1. Introduction

In a petroleum refining process, crude oil is separated, converted and turned into salable valuable products by using hydrogen. While the main products are white products like gasoline and heavy products like fuel oil, naphtha is an intermediate product of the refinery and used to produce high quality gasoline. Naphtha can be produced at each step of complex, such as atmospheric distillation, hydrocracker, and fluid catalytic cracker. However, each refinery that processes unique composition of crude oil produces its own naphtha composition, which separates as light and heavy naphtha [1]. The naphtha mainly has paraffin-type hydrocarbons that have low octane number. It is possible to increase the octane number by rearranging the molecular structures of the paraffins without changing the carbon numbers, i.e. turning them into isoparaffins by means of isomerization (ISO) process. Isomerization reactions give an important pathway for high-octane components in the gasoline [2]. Separation and recovery of the unconverted normal paraffins from their isomers play another major role in isomerate octane quality [3]. For this process, the sulfur, oxygen and nitrogen compounds in the structure of the naphtha are first removed in the naphtha hydrotreating (NHT) units with the help of a suitable catalyst in a hydrogen environment [4].

After NHT, the light naphtha is upgraded in the ISO, whereas the heavy naphtha, typically contains C7+ hydrocarbons, is sent to the continuous catalytic reformer (CCR) unit to produce hydrogen used in refinery demand [5]. In addition, benzene, toluene and xylene form in the reformer effluent. Hydrogen recovery from CCR unit can satisfy the part of the hydrogen demand in refinery but other external sources are required. Most of the external hydrogen is manufactured either by steam–methane reforming (SMR) or by oxidation processes [6].

Environmental pollution has recently created severe fuel regulations that the levels of sulfur compounds in fuels must be limited to less than 10 ppm [7, 8]. To meet this requirement, more efficient hydrodesulfurization (HDS) technology that remove the sulfur-containing compounds, such as mercaptans, thiophene (C_4H_4S), dibenzothiophene ($C_{12}H_8S$), and other polyaromatic derivatives, has been intensely needed [9]. Similar to naphtha, the sulfur compounds in kerosene and diesel as transportation fuels are also reacted with hydrogen and converted to hydrogen sulfide (H_2S) and other hydrocarbon products (ethylbenzene, butene, bicyclohexyl etc.). While mercaptans generally are present in naphtha, thiophene and other compounds having higher molecular size are situated in kerosene and diesel fuels [6].

Hydrocracker (HC) units is one of the hydrogen consumption units in refinery and uses high pressure hydrogen to upgrade heavier fractions into lighter, more valuable products, through carbon-carbon bond breaking and hydrogen addition [5]. The heavier unsaturated fractions obtained from the crude oil distillation, including residue, applies to hydrocracking and the main products have lower boiling points, are highly saturated, and generally range from heavy diesel to light naphtha.

Hydrogen management in refinery is a typical network issue, in which hydrogen sources need to be matched with hydrogen sinks. As hydrogen at high purity is a crucial input for these units mentioned, its production and consumption should be managed based on economic cost-driven analysis [10]. Since the late 1990s, current methodologies published in extensive researches, can be distinguished in two main categories, which are; (i) targeting and design for minimum hydrogen utility; (ii) mathematical programming for detailed design and retrofit [7]. Pinch based conceptual methodology first proposed by Alves in 1999 [11]. It is easy to understand and has the potential to improve the efficiency of the mathematical approach [12]. In addition to hydrogen pinch analysis, mathematical approach is to formulate the hydrogen network problem as a prevalent optimization problem, using a convenient mathematical programming language [13].

Hydrogen network integration via the pinch analysis approach has been known as an effective way of process optimization [14]. The network integration has become prevalent because of the economic concerns and sustainability. On the other hand, exergy analysis, which takes also into account irreversibility, is more applicable and much more powerful thermodynamic tool [15]. Energy utilization options are restricted by thermodynamic principles and exergy analysis identifies the location, the magnitude, and the sources of the thermodynamic inefficiencies in a thermal system [16]. Exergy analysis has been applied individually in many different hydrogen production systems [17-21]. Although the exergy applications on the NHT process also performed [22-25], each model is a unique due to the unique naphtha composition and simulation. While the exergy analysis of cracking and reforming units has been performed in these models, light-naphtha has been assessed together with heavy naphtha, or only n-heptane has been choosen as a model compound [26-29].

Even though lots of pinch analysis studies on the refinery also performed [7, 30-32], the addition of exergy analysis to hydrogen network has been a new trend for the last years [33-35]. To improve the heat integration efficiency of refinery plant units, the exergy was used instead of enthalpy in pinch analysis [36, 37]. Lou et al. [12] developed the entropy change-based design method for multi-contaminant hydrogen

network by using mathematical approach. Though Wu et al. [38] minimized the number of compressors and total exergy consumption in the refinery hydrogen distribution system, reactors in the network were not taken into account. The exergy as energy performance, environment issue and cost were generally selected as optimization objectives in other previous researches [33, 35].

In typical hydrogen management exercises, the partial pressure of hydrogen is assumed to be constant, as well as other parameters such as reactor feedstock, products, operating temperature, etc. However, the partial pressure in a reactor is a significant parameter for the reaction [7]. Under these approach, the efficiency of the reactor may not be assessed merely by hydrogen pinch analysis. Adding exergy analysis to the hydrogen pinch analysis especially for refinery plants, where hydrogen reacts under high temperature and pressure, will help improve this situation.

In this study, the exergy analysis is performed to current hydrogen network of a petroleum refinery retrofitted by hydrogen pinch analysis before. As the difference from other studies, it is assessed exergy loss of reactors in the hydrogen network. The energy and mass saving in related rafinery was supplied before, and this present study focuses on the reactors especially for investigating the energy bottlenecks. At this point, the exergy analysis applied easily to various systems, is most proper tool able to detect any source of this inefficiency. In other words, it is target to ascertain undetected unit/units that could be created any energy bottleneck at the refinery hydrogen network. The simulation of network, in which hydrogen sources were matched with hydrogen sinks, is first created and then exergetic efficiency of entire reactors is evaluated. Two hydrogen production and four consumption units are designed by Aspen Plus V8 based on the operating feed rates of hydrogen, and so each exergetic efficiency of the reactors are calculated.

2. Process and methods

Process Description

The flowsheet of units in the hydrogen network corresponds to the actual petroleum refinery. However, appropriate changes and assumptions in the process have been made, taking into account privacy policies. In this sense, the hydrogen network comprises of all units that consume or produce the hydrogen. This network is divided into two production units and four main consumer units (Figure 1). While the hydrogen is consumed in hydrotreating, isomerization, hydrodesulphurization and hydrocracking units, catalytic and steam reformer units contribute to these units by hydrogen production. The general flowsheet of hydrogen network is given in Figure 1 and the exergy analysis has been conducted in the boundary of each unit shown as red dashed line.

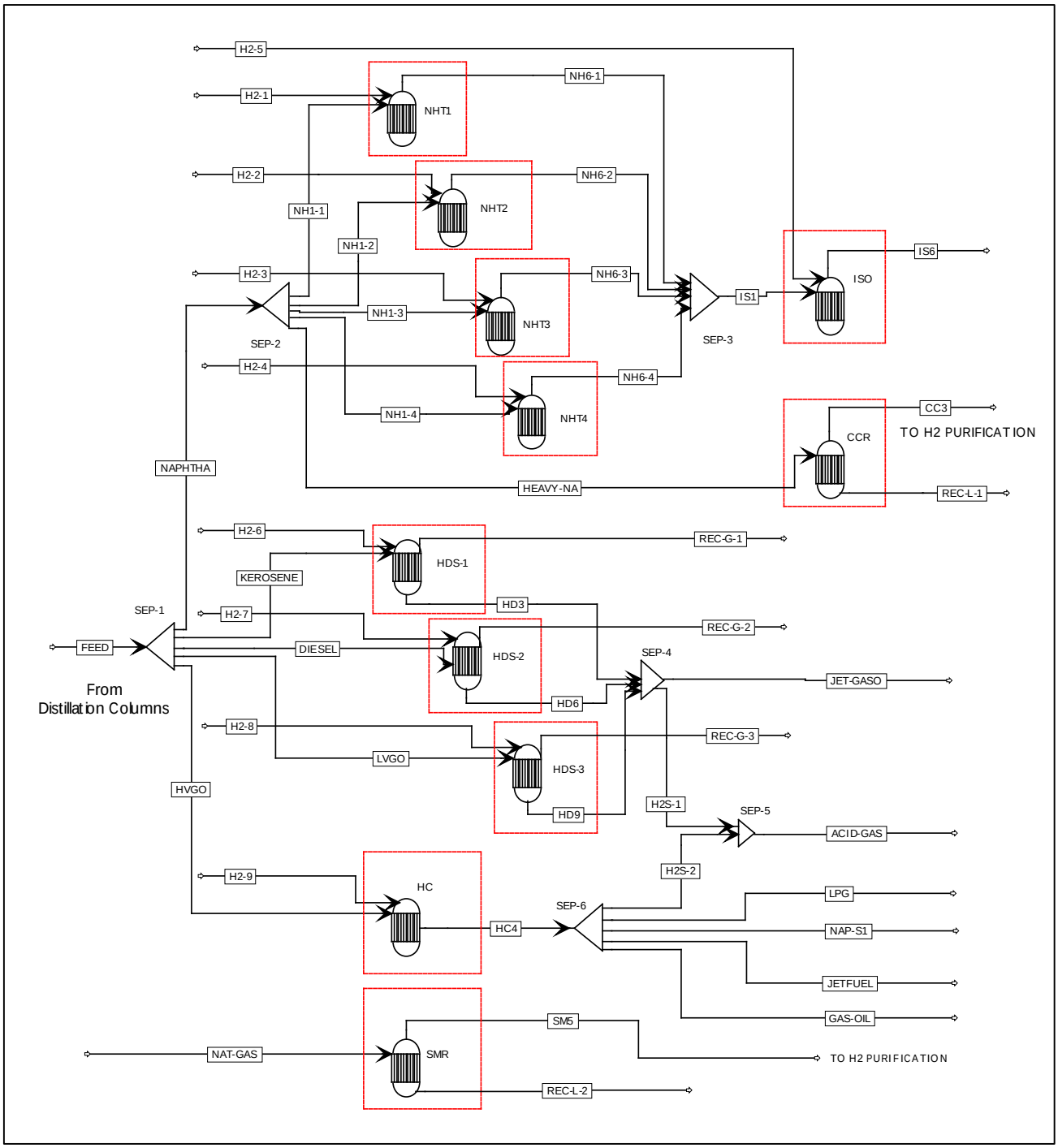

Figure 1. *Flowsheet of reactors on the petroleum refinery hydrogen network*

Figure 1 is also shown the product distribution in the refinery plant generally. Crude oil, signified as feed in Figure 1, is mixture of hydrocarbon molecules containing C1 to C60. Naphtha, kerosene and diesel are mainly produced as side stream products by atmospheric distillation of crude oil, whereas light vacuum gas oil (LVGO in figure) and heavy vacuum gas oil (HVGO in figure) are produced by vacuum distillation unit. NHT and ISO processes are applied to crude light straight run naphtha (C4–C6) for removing undesired compounds and upgrading octane number. In the simulation, the desired products form in vapor phase for these units, and four NHT and one ISO reactors are present in the rafinery (Figure 1). The sulphur compounds in kerosene, diesel and LVGO are removed in the HDS units with the help of a suitable catalyst in a hydrogen environment, and the desired products is obtained in liquid stream. For these three

products, three different HDS reactors are present in Figure 1. Moreover, HVGO is fed to the HC reactor operating at high pressure in hydrogen medium, to crack the heavy molecules into lighter molecular weight compounds, with boiling point ranging from LPG's to gas-oil's. The desired products leave from the cracker with hydrogen in the vapor stream. The compositions of entire feed and hydrogen streams are given in Table 1.

Table 1. *The compositions of entire feed and hydrogen streams*

Unit	Feed	Composition (%vol.)	H_2 consumption (%)
NHT-1 NHT-2 NHT-3 NHT-4	**Naphtha:** C_4H_{10}; C_5H_{12}; C_6H_{14}	30; 30; 30	H_2: 70%; CH_4: 18% C_2H_6: 10%; C_3H_8: 2%
	C_4H_8; C_5H_{10}; C_6H_{12}; C_6H_6	1.4; 1.4; 1.4; 1.8	
	C_2H_6S; $C_2H_6S_2$	2; 2	
ISO	**NHT outlet**		H_2: 90%; CH_4: 6% C_2H_6: 3%; C_3H_8: 1%
HDS-1	**Kerosene:** n-C9; n-C10; n-C11; n-C12; n-C13; n-C14; n-C15; n-C16;	Each comp. 12.2	H_2: 70%; CH_4: 18% C_2H_6: 10%; C_3H_8: 2%
	C_2H_6S; $C_2H_6S_2$; C_4H_4S; C_8H_6S; $C_{12}H_8S$	Each comp. 0.5	
HDS-2	**Diesel:** n-C18; n-C20;	47.5; 50	H_2: 70%; CH_4: 18% C_2H_6: 10%; C_3H_8: 2%
	C_2H_6S; $C_2H_6S_2$; C_4H_4S; C_8H_6S; $C_{12}H_8S$	Each comp. 0.5	
HDS-3	**LVGO:** n-C25;	96;	H_2: 85%; CH_4: 9% C_2H_6: 5%; C_3H_8: 1%
	C_2H_6S; $C_2H_6S_2$; C_4H_4S; C_8H_6S; $C_{12}H_8S$	Each comp. 0.8	
HC	**HVGO:** n-C30;	95;	H_2: 90%; CH_4: 6% C_2H_6: 3%; C_3H_8: 1%
	C_2H_6S; $C_2H_6S_2$; C_4H_4S; C_8H_6S; $C_{12}H_8S$	Each comp. 1	
CCR	**Heavy Naphtha:** C_6H_{12}; C_7H_{14}; C_8H_{16};	1; 21; 46;	-
	C_6H_{14}; C_7H_{16}; C_8H_{18}	19; 8; 5	
SMR	**Natural gas:** CH_4	100	-

High-quality hydrogen is consumed during the HC reactions, and thus SMR is used to satisfy the demand. For production of hydrogen, natural gas is fed to the reactor and the desired product in vapor phase goes to the purification section (Figure 1). Even though the high-quality hydrogen is also used for other consumer processes, CCR and semi-regen reformer (SRR) are main units in the hydrogen network to produce hydrogen. By using CCR and SRR, hydrotreated heavy straight run naphtha (C6–C8) is converted to hydrogen. In this simulation, CCR unit is selected due to produce higher-quality and -capacity hydrogen than SRR in the simulated plant. The compositions of entire feed and hydrogen streams are also chosen within actual refinery data and prototype calculations are carried out. The process conditions and chemical reactions in each unit are given in Table 2 and Table 3.

Table 2. *The operating conditions of each unit*

Unit	Temp. (°C)	Pressure (kg/cm^2g)	Flow rates (m^3/h)	H_2 Flow rates (m^3/h)
NHT-1	200	30	60	600
NHT-2	200	30	150	1500
NHT-3	200	30	100	1000
NHT-4	200	30	60	2100
ISO	130	30	100	4500
HDS-1	340	35	50	2500
HDS-2	340	35	50	2500
HDS-3	340	65	400	40000
HC	390	155	120	37200
CCR	520	42	150	-
SMR	840 and 340	20	43000	-

Table 3. *The reactions defined for each unit*

Unit	Reactions	Unit	Reactions
NHT	$C_6H_6 + 3H_2 \rightarrow C_6H_{12}$ $C_6H_{12} + H_2 \rightarrow C_6H_{14}$ $C_2H_6S + H_2 \rightarrow C_2H_6 + H_2S$ $C_2H_6S_2 + 3H_2 \rightarrow 2CH_4 + 2H_2S$	SMR	$CH_4 + H_2O \rightarrow CO + 3H_2$ $CO + H_2O \leftrightarrows CO_2 + H_2$
ISO	$C_4H_8 + H_2 \rightarrow n - C_4H_{10}$ $C_5H_{10} + H_2 \rightarrow n - C_5H_{12}$ $C_6H_{12} + H_2 \rightarrow n - C_6H_{14}$ $n - C_5H_{10} + H_2 \rightarrow CH_4 + n - C_4H_{10}$ $n - C_4H_{10} \leftrightarrows i - C_4H_{10}$ $n - C_5H_{12} \leftrightarrows i - C_5H_{12}$ $n - C_6H_{14} \leftrightarrows i - C_6H_{14}$ (2-methyl-pentane) $n - C_6H_{14} \leftrightarrows i - C_6H_{14}$ (2,3-dimethyl-butane)	CCR	$C_6H_{12} \rightarrow C_6H_6 + 3H_2$ $C_7H_{14} \rightarrow C_7H_8 + 3H_2$ $C_8H_{16} \rightarrow C_8H_{10} + 3H_2$ $C_6H_{14} \rightarrow C_6H_6 + 4H_2$ $C_6H_{14} + H_2 \rightarrow C_5H_{12} + CH_4$ $C_7H_{16} + H_2 \rightarrow i - C_4H_{10} + C_3H_8$ $C_8H_{18} + H_2 \rightarrow n - C_4H_{10} + i - C_4H_{10}$
HDS	$C_2H_6S + H_2 \rightarrow C_2H_6 + H_2S$ $C_2H_6S_2 + 3H_2 \rightarrow 2CH_4 + 2H_2S$ $C_4H_4S + 3H_2 \rightarrow C_4H_8 + H_2S$ $C_8H_6S + 3H_2 \rightarrow C_8H_{10} + H_2S$ $C_{12}H_8S + 8H_2 \rightarrow C_{12}H_{22} + H_2S$	HC	$C_{30}H_{62} + H_2 \rightarrow n - C_{20}H_{42} + n - C_{10}H_{22}$ $C_{20}H_{42} + H_2 \rightarrow n - C_{10}H_{22} + n - C_{10}H_{22}$ $C_{10}H_{22} + H_2 \rightarrow n - C_5H_{12} + i - C_5H_{12}$ $C_{10}H_{22} + 2H_2 \rightarrow n - C_5H_{12} + n - C_4H_{10} + CH_4$ $C_{10}H_{22} + 3H_2 \rightarrow i - C_4H_{10} + C_3H_8 + C_2H_6 + CH_4$ $C_2H_6S + H_2 \rightarrow C_2H_6 + H_2S$ $C_2H_6S_2 + 3H_2 \rightarrow 2CH_4 + 2H_2S$ $C_4H_4S + 3H_2 \rightarrow C_4H_8 + H_2S$ $C_8H_6S + 3H_2 \rightarrow C_8H_{10} + H_2S$ $C_{12}H_8S + 8H_2 \rightarrow C_{12}H_{22} + H_2S$

Modeling of Hydrogen Network

The cascaded units are simulated in software Aspen Plus V8. The sequential simulation is performed on the boundary of each unit and the inlet compositions are assumed by considering the actual rates of hydrogen feed. RK-SOAVE property method as the most suitable model for refinery applications is chosen. Because each refinery that processes unique composition of crude oil produces its own product composition, the base case of units is provided by the actual plant data at certain time depending on some appropriate changes in operating conditions. In case fractional conversion of reaction is known, RStoic reactor model is used in the modeling. Other case, rigorous equilibrium reactor (REquil) model is selected based on stoichiometric approach. The fractional conversion for the most of the reaction is chosen as minimum 0.90. However, n-hexane conversion to benzene in CCR, n-pentane conversion to methane and butane in ISO, and methylcyclopentane conversion to hexane in NHT are adjusted as 60%, 4% and 40%, respectively. The outlet streams are cooled to 30°C, and the pressure of streams drops to 5 kg cm^{-3}(g) so as to separate the desired product from hydrogen flow.

Exergy Analysis

Considering the exergy analysis for hydrogen network, the kinetic, potential, nuclear, magnetic, and electrical exergies are neglected; therefore, the total exergy rate of each stream is formed by sum of only chemical (E^{ch}) and physical exergies (E^{ph}). The physical exergy rates of streams are determined by Aspen Plus according to the general equation [39], while standard chemical exergy rates of any components in the gas mixture is taken from basis of Szargut's model [40]. As a result, the equations are given as

$$\dot{E}^{ph} = (\dot{H} - \dot{H}_0) - T_0(\dot{S} - \dot{S}_0) \quad (1)$$

$$\dot{E}^{ch} = \dot{m}\bar{e}^{ch} = \dot{m}\left[\sum x_k \bar{e}_k^{ch} + RT_o \sum x_k \ln x_k\right] \quad (2)$$

where H is enthalpy flow rate, S is entropy flow rate, m is mass flow rate, x_k is the mole fraction of k_{th} component, $\bar{e}^{ch}$ is standard chemical exergy of k_{th} substance, R is gas constant, T is the temperature of the environment whose temperature and pressure are chosen as 298 K and 1 atm in present study. Though the standard chemical exergy of most compounds is taken from data of Szargut [40], by using Table II, the remains (C_8H_6S; $C_{12}H_8S$, $C_{12}H_{22}$, C18, C20, C21 and C30) have been calculated according to group contribution by using Table III in the same book. Moreover, the overall efficiency of each unit is calculated by the ratio of the exergy rate of desired outlet stream to that of inlet streams.

3. Results and discussion

The hydrogen network integration is the most important part of crude oil refinery plant because a lot of units consume the hydrogen-rich gas as both make-up gas and reactant. The hydrogen pinch analysis, which creates hydrogen network of a plant, reduces the hydrogen surplus by matching only the hydrogen streams. However, other compounds in the stream are not evaluated. To assess entire compounds, exergy analysis together with pinch analysis is more powerful thermodynamic tool in case the presence of various units. The proposed hydrogen network in this study is thermodynamically analyzed using exergetic approaches. This study creates the cascaded unit simulation with the help of main inlet streams and reactions and examines the network results. The main criteria of simulation were the hydrogen flow rate per unit feed capacity. While the inlet stream properties were assumed as unit operating conditions, the outlet stream were cooled at 30°C and expanded to 6 bars. The stream data of analysis results are given in Table 4. Even though the processes were carried out at the moderate and high operating conditions, the physical exergy flow rates of whole streams were significantly lower than chemical exergy rates. The change in composition between inlet and outlet (Table A1 to A3) by reactions considerably effected chemical exergy rate.

In the proposed network the consumption units of hydrogen consist of HC, HDS, NHT and ISO, whereas the production units are CCR and SMR. The exergy efficiencies of the production units were calculated as 22% and 43%, respectively. Their reactions proceeded at the highest temperature of the network in low and moderate pressure conditions. In addition, the highest physical and chemical exergy rates were determined in SMR unit. The desired flow had the hydrogen molar fraction of 77% (Table A1). It is predicted that adding purification process data to the calculation could also tends to change in exergy efficiency more. Although the hydrogen fraction was not remarked, Silva and Oliveira calculated the exergy efficiency of SMR as about 77% by using pressure swing adsorption [41]. Contrast to SMR unit, adjusting the operating conditions of the outlet stream positively affected the vapor fraction in CCR unit and caused to increase hydrogen purity (88%).

Considering the hydrogen consumption units, it can be remarked that HDS units have the lowest exergy efficiency (24%, 32% and 26%) in the network. In these units, high-molecular-weight hydrocarbons is cleaned from sulphur compounds by hydrogen flow, and thus the desired products can be easily separated from the excess hydrogen flow contrary to other consumption units. HDS unit also has the lowest exergy efficiency in a previous study carried out in a different refinery plant [41]. NHT and ISO units, that involve high-quality naphtha in the desired stream, have high exergetic efficiency because of the absence of hydrogen recovery in the simulation. Naphtha is involving a mixture of hydrocarbon components ranging from C_2 to C_6. In order to the recovery of hydrogen from this mixture, many refiners normally use membrane and pressure swing adsorption (PSA) units. Even though cryogenic recovery is also feasible, the increased complexity in operating cryogenic units makes it unfavorable alternative unless recovery of light hydrocarbons is also desired [5]. If one of these types of recovery systems is added to the simulation, more practical exergetic efficiency could be calculated.

Similarly, the exergetic efficiency of HC unit was also determined as about 99% due to the present of excess hydrogen in the desired product. Considering the desired products of HC unit, the reactor outlet streams are cooled in some exchangers and the vapor and liquid are separated in high-pressure and low-pressure separators to remove light ends in fractionation section. The low-pressure liquid is pumped to the recycle splitter flash drum and after heating in a furnace, it goes to recycle splitter for producing main products [36]. By adding this type of fractionation section to the simulation, the excess hydrogen, naphtha, kerosene, diesel and gasoline can be separated from the desired outlet stream, and thus practical exergetic efficiency could also be obtained.

Table 4. *Stream data of exergy analysis results*

Unit	Stream info	Temperature (°C)	Pressure (bar)	Vapor Fraction	Mole Flow (kmol/h)	Mass Flow (kg/h)	Physical Exergy Rate (MW)	Chemical Exergy Rate (MW)	Unit Efficiency (%)
CCR	In*	520	42	1	6.69	690.52	0.14	8.97	22%
	Desired Out **	30	6	1	15.95	104.20	0.02	1.95	
SMR	In	840	20.6	1	9680.00	155293.92	91.19	2235.91	43%
	In	214	20.6	1	18400.00	331481.15	93.69	4149.64	
	Desired Out	30	6	1	45504.00	486775.07	53.71	2768.58	
HC	In	390	153	0	5.35	2180.45	0.25	28.17	98%
	In	30	30	1	1659.68	6837.73	3.84	113.04	
	Desired Out	30	6	1	1664.40	9018.20	1.99	178.27	
HDS-1	In	340	35	0	2.23	391.86	0.03	5.10	24%
	In	25	35	1	111.54	913.24	0.27	15.72	
	Desired Out	30	6	0	2.26	387.36	0.00	5.07	
HDS-2	In	360	35	0	2.23	591.06	0.06	7.67	32%
	In	25	35	1	111.54	913.24	0.27	15.72	
	Desired Out	30	6	0	2.29	590.49	0.00	7.68	
HDS-3	In	360	65	0	17.85	5160.87	0.48	66.80	26%
	In	30	65	1	1784.60	9104.67	5.06	184.28	
	Desired Out	30	6	0	17.79	5126.81	0.00	66.62	
ISO	In	130	30	0.843	4.46	203.28	0.01	2.74	98%
	In	30	30	1	200.77	444.75	0.47	13.67	
	Desired Out	30	6	1	205.13	648.03	0.25	16.38	
NHT-1	In	200	30	1	2.68	193.84	0.01	2.53	99%
	In	30	30	1	26.77	73.90	0.06	1.99	
	Desired Out	30	6	1	29.27	267.74	0.04	4.50	
NHT-2	In	200	30	1	6.69	484.61	0.02	6.31	99%
	In	30	30	1	66.92	184.75	0.16	4.98	
	Desired Out	30	6	1	73.17	669.36	0.09	11.25	
NHT-3	In	200	30	1	4.46	323.07	0.02	4.21	99%
	In	30	30	1	44.62	123.16	0.10	3.32	
	Desired Out	30	6	1	48.78	446.24	0.06	7.50	
NHT-4	In	200	30	1	2.68	193.84	0.01	2.53	99%
	In	30	30	1	93.69	258.64	0.22	6.97	
	Desired Out	30	6	1	96.19	452.49	0.12	9.51	

* "In" represents to inlet stream,
**"Desired Out" represents to desired outlet streams

4. Conclusions

The proposed hydrogen network was created before by reducing the hydrogen surplus and matching only the hydrogen streams. However, in this study the reactor simulations and the reactions were considered by using exergy analysis. As a result, the chemical exergy flow rates were significantly (about 100 times) higher than physical exergy flow rates. Although the processes were carried out at the moderate and high operating conditions, the exergy efficiency of each unit was clearly affected by reactions in it. On the other hand, the exergy analysis results show that not only the hydrogen demand of units has to be reduced, but also the hydrogen recovery is very important for the efficiency of units. At this point, the purification systems and the new hydrogen recovery stream can be added to the simulation in order to obtain higher exergetic efficiencies.

References

[1]. Singh G., "Applied chemistry", Discovery Publishing House, New Delhi, 2009.

[2]. Liu Y.A., Chang Ai-Fu, Pashikanti K. "Petroleum Refinery Process Modeling", Wiley, ePDF ISBN: 978-3-527-81336-0, 2018.

[3]. Valavarasu G., Sairam B. Light Naphtha Isomerization Process: A Review, Petroleum Science and Technology, 31:6 (2013), 580-595.

[4]. Karadag O., "Automatic gasoline blending system modelling at TUPRAS", MSc. Thesis, Institute of Science, ITU, Istanbul, TR, 2008.

[5]. Treese A. S., Pujado P.R., Jones D.S.J, "Handbook of Petroleum Processing", Springer Cham, Second edition, New York, 2006.

[6]. El-Gendy N.S., Speight J.G., "Handbook of Refinery Desulfurization", CRC Press Taylor & Francis Group, Boca Raton, 2016.

[7]. Zhang N. "Process Integration of an oil refinery hydrogen network", In: Klemes J. editors. Handbook of Process Integration (PI), Woodhead Publishing, 2013.

[8]. Jin Q, Chen B., Ren Z., Liang X., Liu N., Mei D., "A theoretical study on reaction mechanisms and kinetics of thiophene hydrodesulfurization over MoS2 catalysts", Catalysis Today 312 (2018), 158–167.

[9]. Lauritsen J.V., Kibsgaard J., Olesen G.H., Moses P.G., Hinnemann B., Helveg S., Nørskov J.K., Clausen B.S., Topsøe H., Lægsgaard E., "Location and coordination of promoter atoms in Co- and Ni-promoted MoS2-based hydrotreating catalysts", Journal of Catalysis 249, (2007) 220–233.

[10]. Elsherif M., Manan Z.A., Kamsah M.Z., "State-of-the-art of hydrogen management in refinery and industrial process plants", Journal of Natural Gas Science and Engineering 24, (2015) 346-356.

[11]. Alves J.J. "Analysis and design of refinery hydrogen distribution systems", PhD thesis, UMIST, University of Manchester, Manchester, UK, 1999.

[12]. Lou J., Liao Z., Jiang B., Wang J., Yang Y., "A thermodynamic irreversibility based design method for multi-contaminant hydrogen networks", International Journal of Hydrogen Energy 40, (2015) 435–443.

[13]. Marques J.P., Matos H.A., Oliveira N.M.C., Nunes C.P., "State-of-the-art review of targeting and design methodologies for hydrogen network synthesis", International Journal of Hydrogen Energy 42, (2017) 376–404

[14]. Oduola M.K, Oguntola T.B., "Hydrogen pinch analysis of a petroleum refinery as an energy management strategy", American Journal of Chemical Engineering, Special Issue 3, No. 2-1, (2015) 47-54.

[15]. Wall, G., Gong, M., "Exergy analysis versus pinch technology, efficiency, costs, optimization, simulation and environmental aspects of energy systems", in International Symposium on Efficiency, Costs, Optimization, Simulation and Environmental Aspects of Energy Systems (ECOS'96), June 25-27, 1996. Stockholm, 451–455.

[16]. Mert M.S., Dilmaç Ö.F., Özkan S., Karaca F., Bolat E., "Exergoeconomic analysis of a cogeneration plant in an iron and steel factory", Energy 46 (2012), 78-84.

[17]. Dilmaç, Ö.F. and Özkan, S.K. "Energy and exergy analyses of a steam reforming process for hydrogen production", Int. J. Exergy, 5, 2 (2008), 241–248.

[18]. Ozturk M., Dincer I. "Thermodynamic analysis of a solar-based multi-generation system with hydrogen production", Applied Thermal Engineering, 51, (2013), 1235-1244.

[19]. Yuksel Y.E., Ozturk M., Dincer I., Thermodynamic analysis and assessment of a novel interated geothermal energy-based system for hydrogen production ans

storage", International Journal of Hydrogen Energy 43 (2018), 4233-4243.

[20]. Mert M.S., Yüksel F., Burulday M.E., "Biyokütle Kaynaklı Sentez Gazından Hidrojen Üretimine Entegre Bir Güç Sisteminin Modellenmesi", Erzincan Üni. Fen Bilimleri Ens. Dergisi 12(2) (2019), 607-619.

[21]. Ishaq H., Dincer I., "Multi-objective optimization and analysis of a solar energy driven steam and autothermal combined reforming system with natural gas", Journal of Natural Gas Science and Engineering 69 (2019), 102927, 1-19.

[22]. Agbo A. F, Aboje A. A, Obayomi K. S, Exergy analysis of Naphtha Hydrotreating Unit (NHU), 3rd International Conference on Science and Sustainable Development (ICSSD 2019) 1299 012025, 2019.

[23]. Rivero R. Application of the exergy concept in the petroleum refining and petrochemical industry, Energy Conversion and Management 43 1199–1220, 2002.

[24]. Akram A.U., Ahmad I., Chughtai A. Exergy Analysis and Optimization of Naphtha Reforming Process with Uncertainty, Int. J. of Exergy, 26 (3), 2018

[25]. Sadighi S., Mohaddecy S.R.S., Ghabouli O., Bahmani M. Revamp of Naphtha hydrotreating process in an Iranian Refinery, Petroleum & Coal 51(1) 45-50 2009.

[26]. Mustafa, J., Ahmad, I., Ahsan, M. and Kano, M. "Computational fluid dynamics based model development and exergy analysis of naphtha reforming reactors", Int. J. Exergy 24, (2017) Nos. 2/3/4, 344–363.

[27]. Johanna Puolakka, K. and Krause, A.O.I. "CO2 reforming of n-heptane on a Ni/Al2O3 catalyst", Studies in Surface Science and Catalysis 153, (2004), 329–332.

[28]. Ran, R., Xiong, G.X., Sheng, S.S. and Yang, W.S. "The effects of CO2 addition on the partial oxidation of heptane for hydrogen generation", Chinese Chemical Letters 15, No. 5, (2004), 605–608.

[29]. Abashar, M.E.E. "Low temperature catalytic reforming of heptane to hydrogen and syngas", Journal of Saudi Chemical Society, King Saud University 20, (2016) S186–S195.

[30]. Worrell E., Corsten M., Galitsky C., "Energy efficiency improvement and cost saving opportunities for petroleum refineries", in an Energy Star Guide for energy and plant managers, U.S. Environmental Protection Agency, Document Number 430-R-15-002, 2015. [Online] Available: http://www.energystar.gov [Accessed: July. 28, 2020]

[31]. Lou Y., Liao Z., Sun J., Jiang B., Wang J., Yang Y., "A novel two-step method to design inter-plant hydrogen network", International Journal of Hydrogen Energy 44, (2019), 5686-5695.

[32]. Ozcelik Z., Karamandal N., "Hydrogen recovery system design application in a petrochemical refinery", Petroleum and Coal 61(6), (2019) 1414-1424.

[33]. Wu, S., Liu, G., Yu, Z., Feng, X., Liu, Y., Deng, C., "Optimization of hydrogen networks with constraints on hydrogen concentration and pure hydrogen load considered", Chemical Engineering Research and Design 90, (2012), 1208-1220.

[34]. Chen, B., Liao, Z., Wang, J., Yu, H., Yang, Y., "Exergy analysis and CO2 emission evaluation for steam methane reforming" International Journal of Hydrogen Energy 37, (2012) 3191-3200.

[35]. Wang Y., Wu S., Feng X., Deng C., "An exergy-based approach for hydrogen network integration", Energy 86, (2015) 514-524.

[36]. Goodarzvand-Chegini F. and GhasemiKafrudi E., "Application of exergy analysis to improve the heat integration efficiency in a hydrocracking process", Energy & Environment 28 (5–6), (2017) 564–579.

[37]. Mehdizadeh-Fard M., Pourfayaz F., Mehrpooya M., Kasaeian A., "Improving energy efficiency in a complex natural gas refinery using combined pinch and advanced exergy analyses" Applied Thermal Engineering 137, (2018) 341–355.

[38]. Wu S., Yu Z., Feng X., Liu G., Deng C., Chu K.H., "Optimization of refinery hydrogen distribution systems considering the number of compressors", Energy 62, (2013) 185-195.

[39]. Bejan A., Tsatsaronis G., Moran M.J. "Thermal Design and Optimization" John Wiley, 1996, 113–167

[40]. Szargut J., Morris D.R., Steward F.R., "Exergy Analysis of Thermal, Chemical and Metallurgical Processes", Hemisphere Publishing Corporation, New York, 1988.

[41]. Silva J.A.M. and Oliveira Jr. S., “An exergy-based approach to determine production cost and CO_2 allocation in refineries”, Energy 67, (2014), 607-616.

APPENDICES

Table A.1. *The mole fractions of streams for hydrogen production units*

	CCR		SMR		
Compounds	**Inlet**	**Desired Outlet**	**Inlet**	**Inlet**	**Desired Outlet**
H2		0.882			0.766
CH4		0.038	1.000		0.021
C2H6		0.030			
C3H8		0.017			
C5H12-1		0.027			
C6H14-1	0.190	trace			
C6H12-2	0.010	trace			
C6H6		0.003			
CO2					0.191
H2O				1.000	0.021
C7H14-6	0.210	trace			
C8H16-8	0.460	trace			
C7H16-1	0.080	trace			
C8H18-1	0.050	trace			
C7H8		0.002			
C8H10-3		0.001			

Table A.2. *The mole fractions of streams for hydrocracking and hydrodesulphurization units*

	HC			HDS-1			HDS-2			HDS-3		
Compounds	**Inlet**	**Inlet**	**Desired Outlet**	**Inlet**	**Inlet**	**Desired Outlet**	**Inlet**	**Inlet**	**Desired Outlet**	**Inlet**	**Inlet**	**Desired Outlet**
H2		0.90	0.9890		0.700	0.003		0.700	0.003		0.850	0.004
CH4		0.06	0.0080		0.180	0.006		0.180	0.006		0.090	0.003
H2S			0.0002			0.000			trace			trace
C2H6		0.03	0.0020		0.100	0.018		0.100	0.018		0.050	0.009
C3H8		0.01	0.0005		0.020	0.012		0.020	0.012		0.010	0.006
C4H10-1			0.0000									
C4H8-4						trace			trace			trace
C2H6S-1	0.010		trace	0.005		trace	0.005		trace	0.008		trace
C2H6S2	0.010			0.005		trace	0.005		trace	0.008		trace
C4H4S	0.010			0.005		trace	0.005		trace	0.008		trace
C8H6S	0.010		trace	0.005		trace	0.005		trace	0.008		trace
C12H8S	0.010			0.005		trace	0.005		trace	0.008		trace
C8H10-4			trace			0.004			0.004			0.005
C12H22			trace			0.005			0.005			0.008
C9H20-1				0.122		0.113						
C10H22-1				0.122		0.118						
C11H24				0.122		0.120						
C12H26				0.122		0.120						
C13H28				0.122		0.121						
C14H30				0.122		0.121						
C15H32				0.122		0.121						
C16H34				0.121		0.120						
C21H44										0.960		0.963
C18H38							0.475		0.463			
C20H42							0.500		0.487			
C30H62	0.950		trace									

Table A.3. *The mole fractions of streams for naphtha hydrotreating and isomerization units*

	ISO			NHT-1			NHT-2			NHT-3			NHT-4		
Compounds	**Inlet**	**Inlet**	**Desired Outlet**	**Inlet**	**Inlet**	**Desired Outlet**	**Inlet**	**Inlet**	**Desired Outlet**	**Inlet**	**Inlet**	**Desired Outlet**	**Inlet**	**Inlet**	**Desired Outlet**
H2	0.090	0.90	0.9693		0.700	0.863		0.700	0.863		0.700	0.863		0.700	0.930
CH4	0.191	0.06	0.0124		0.180	0.032		0.180	0.032		0.180	0.032		0.180	0.031
H2S	0.013		0.0003			0.005			0.005			0.005			0.002
C2H6	0.199	0.03	0.0065		0.100	0.010		0.100	0.010		0.100	0.010		0.100	0.009
C3H8	0.057	0.01	0.0017		0.020	0.001		0.020	0.001		0.020	0.001		0.020	0.001
C4H10-1	0.113		0.0008	0.300		0.027	0.300		0.027	0.300		0.027	0.300		0.008
C5H12-1	0.140		0.0006	0.300		0.027	0.300		0.027	0.300		0.027	0.300		0.008
C6H14-1	0.175		0.0007	0.300		0.029	0.300		0.029	0.300		0.029	0.300		0.009
C4H8-4	0.005		trace	0.014		0.001	0.014		0.001	0.014		0.001	0.014		trace
C5H10-1	0.006		trace	0.014		0.001	0.014		0.001	0.014		0.001	0.014		trace
C6H12-2	0.011		trace	0.014		0.002	0.014		0.002	0.014		0.002	0.014		0.001
C6H6				0.018		trace	0.018		trace	0.018		trace	0.018		trace
C2H6S-1				0.020		trace	0.020		trace	0.020		trace	0.020		trace
C2H6S2				0.020			0.020			0.020			0.020		
C6H14-2			0.0025												
C6H14-5			0.0008												
C4H10-2			0.0019												
C5H12-2			0.0024												

MANAS Journal of Engineering
ISSN 1694-7398 | e-ISSN 1694-7398

Volume 9, Special Issue 1, (2021) Pages 24-34
https://doi.org/10.51354/mjen.828545

Comparison of artificial neural network models of categorized daily electric load

Vildan Evren[1], Ilker Ali Ozkan[2]

[1] Selcuk University, Selcuk University, The Degree of Master of Science of Information Technologies Engineering, 42000 Konya, Turkey, evrenvildannn@gmail.com, ORCID: 0000-0003-1654-3731

[2] Computer Engineering Department, Faculty of Technology, Selcuk University, 42000 Konya, Turkey, ilkerozkan@selcuk.edu.tr, ORCID: 0000-0002-5715-1040

ABSTRACT

The efficient operation of power systems and future planning, electricity load forecast is very important. Load estimation is based on predicting future electric load by examining past conditions. Short-term load prediction plays a decisive role in the load sharing of power plants. It also allows to overcome shortcomings caused by sudden load increases and power plant losses. Weather conditions are effective in short-term electrical load estimation. Daily or hourly electricity consumption data is generally used for short-term load estimation. In this study, daily electrical energy consumption of Turkey in the four years of data were used. Short-term load prediction modeling has been carried out. In this modeling, past electrical load values and temperature values were used as input, and in order to increase the prediction accuracy, the characteristics of the days were categorized weekly and classified according to the seasons. Different Artificial Neural Network models have been created according to input data, weekly categorization, and season criteria. In the study, mean absolute percentage error values were calculated. Among the models developed with ANN, the best MAPE value was 2.51% and the worst MAPE value was 4.48%. When the season criterion is added, the MAPE value is more successful.

ARTICLE INFO

Research article

Received: 19.11.2020
Accepted: 19.03.2021

Keywords:
artificial neural network,
short term electrical load forecast,
time series modeling,
daily electric load forecast

**Corresponding author*

1. Introduction

Short-term electrical load estimation is important for power systems. To provide economic reliability to consumers, load estimation should be made meticulously [1]. Planning the transmission and distribution of electrical load increases reliability. Planning decisions are based on estimates known as spatial load. Load forecasts can also help managers with financial planning [2]. Planning electrical energy correctly is important for the economy. When planning ahead of the day, it helps to determine the working programs of the production sites [3]. Better forecasting enables more accurate planning, accurate investment in terms of performance, time, and cost. Forecasting studies for the future are not an easy process. There are many electrical load estimation studies. However, it is not healthy to use them in any country's estimation request. It is not possible to use a general model for the environment and environmental conditions for each country [4].

Electricity load estimation has great importance for the efficient operation of power plants. High error value in estimating the load value may cause to activate too many power units or may cause unnecessary use of reserves and this leads to waste [5]. Many operating decisions are determined by load estimates. The production capacity, distribution planning and maintenance plan of the business depend on the load forecast decision [6]. Electric load demands should be estimated as accurately as possible to make planning studies healthier. It is very important for decision makers to estimate electricity demand in the energy sector with minimum error. Making the planning of work, sharing the load, and determining the best group, making the production in the most economical way increases the importance of short-term electrical load estimation. Electric load estimates are made to make a good system planning.

Electricity estimation is examined in three classes. Short term *(hourly, daily and weekly)*, medium term *(monthly, quarterly)* and long term *(year or more than a year)* [7]. Short-term load forecasts usually include estimates to be made from the hourly forecast up to one week. Short-term load estimates are required for planning functions such as power generation

coordination. This coordination can be used to create hourly schedules of production resources, thereby minimizing operating costs for energy power systems [5]. Short term electrical load estimation is essential for control and planning of the power system. Long and medium term electrical load prediction is used to determine the capacity of the generation, transmission and distribution system [8]. Short term load forecast plays a very important role in improving the economy. It becomes more important with the development of power markets [9].

There are different studies in the literature for the purpose of performing electrical load estimation. In the literature research, it was investigated that artificial neural network gave successful results in estimation processes. Es et al. (2014), by using ANN, conducted the study of Turkey's net energy demand forecast. In this study, ANN and prediction models, which are widely used in the energy field, were examined. Regression and time series models were developed, and comparisons were made with the ANN model to evaluate the success of the prediction study and to measure its performance. Time series error rate was calculated as 3.21% and ANN error value as 1.75%. As a result of the analyzes and comparisons, ANN technique has been determined to make more successful predictions [10].

Yavuzdemir et al. (2014) has made Turkey's short-term electricity demand study. Three different methods were used. Fuzzy logic, time series and regression methods are discussed. Performance evaluation was made by comparing the average absolute error rates of the methods. Time series error rate is 2.75%, fuzzy model error rate is 4.81% and linear regression model error rate is 7.64%. The methods used in applications have yielded successful results [11].

Kaysal et al. (2015) conducted a hybrid (ANN and Regression) model study for load estimation. Artificial neural networks and regression methods are used. What makes the study different is that it has been predicted at micro scale and a hybrid system has been used. The MAPE value was calculated as 6.67% in the ANN model, 7.49% in the regression model and 5.26% in the hybrid model. In this study, the hybrid model gave more successful results [12].

Estimation of unbalance cost due to demand prediction errors using artificial neural network study was conducted by Tümer et al. (2018). The imbalance loss caused by electricity has been estimated. ANN model is used. Load estimation study of Niğde province has been handled. Two different methods are used. Methods, nonlinear trend analysis moving average methods and artificial neural network backpropagation algorithm. The correlation coefficient value by using ANN was 0.78 for the test data set. It was determined that the best results were obtained with the ANN model [13].

Estimation of the electricity consumption of Turkey through artificial neural networks study was conducted by Tümer et al. (2016). ANN was used in this study. The high correlation between estimated electricity load consumption and actual load consumption has reached up to 0.95. Therefore, ANN has been successful in electricity load estimation. In this study, it was seen that ANN is very good at predicting [14].

In the study carried out by Haliloğlu et al. (2018), the electricity loads, and daily totals taken from the EPIAS website at the hourly frequency were taken. Model is created by using least squares method for prediction model. According to the model, daily electricity load estimation study has been made for the period January - April 2018. When electricity demand is brought to the monthly frequency, there is a deviation of 1.64% for January, 1.49% for February, 1.34% for March and 1.30% for April. The success of short-term electrical load estimates is directly proportional to the length of the data set used [15].

A short-term electrical load estimation study was carried out in Nigeria by Adepoju et al. In 2007 using ANN. Using the data used in the training, the electric load of the previous hour, the electric load of the previous day, the electric load of the previous week, the day and hour of that week, a 3-layer ANN was created. There are 3 layers, and these layers are called input layer, hidden layer and output layer. The input layer has 5 neurons. Hourly load estimation study has been done with past load value electrical load data. In this study, 2.54% absolute mean error (MAE) value was obtained. As a result of the obtained results, the applicability of ANN for short term electric load estimation has been approved [16].

Short term load prediction study was carried out by Fan and Hyndman in 2011. The proposed model for estimating the relationship between load demand and independent variables such as calendar and temperature is the semi-parametric regression model. Load estimation study from half an hour prediction to seven days prediction has been conducted for Australian National Electricity Market power systems. In the study, 2.81% MAPE value was obtained [17].

Lee and Tong conducted China's electrical load prediction study using the gray model supported by genetic algorithm in 2011. The gray prediction model can lead to large prediction errors. In order to minimize such errors, a gray model was created in this study using a genetic algorithm. 26.21%, 20.23%, 20.23% and 27.76% MAPE values were achieved in 2004-2007, respectively [18].

Himanshu and Lester developed an experimental model based on regression analysis in 2008 and made the electrical load estimation study of Jordan. Its largest unit is around 120 MW. The approximate error value is 6% and represents a very significant difference [19].

Electric load demands should be predicted as accurately as possible to make planning studies better. Reliable and accurate estimates are needed for the future. The most economical way of electricity generation is important for distribution companies and consumers. The aim of this study is to minimize the error in electrical load estimation. It is aimed to minimize the error rate by handling daily electrical load data.

2. Material method

Daily, hourly, or weekly electricity consumption data is used in short-term load estimation. In this study, daily electrical load data and feed forward backpropagation algorithm of artificial neural network are used. Daily electricity consumption in Turkey in the four years of data are used. Daily energy consumption data of 2016, 2017 and 2018 will be used in the training of artificial neural network. Daily energy consumption data for 2019 was handled as test data. In addition, the seasonal criterion is discussed in application to investigate the importance of electrical energy consumption in seasonal conditions. Daily electricity load data for years were examined. It has been found that there are differences in the daily electrical load data and similarities in the load data and accordingly, the feed forward backpropagation algorithm has been applied by categorizing the data.

2.1. Data Set

Data in the short-term electricity load estimation study belongs to 2016, 2017, 2018 and 2019. Load data were obtained from open access EPIAS website [20]. Temperature data were obtained from the open access Turkey weather websites [21]. Daily load data for 2016, 2017 and 2018 were used in the training of ANN. Daily electricity load data for 2019 was used for model testing. First of all, charts of daily electricity load data are examined by years. In the data used in the developed model, the data of the weeks with the public holiday were removed from the dataset. The electricity load data for the remaining 303 days of the year were estimated. In Figure 1, the daily electricity load amount graph for 2016, 2017, 2018 and 2019 were given.

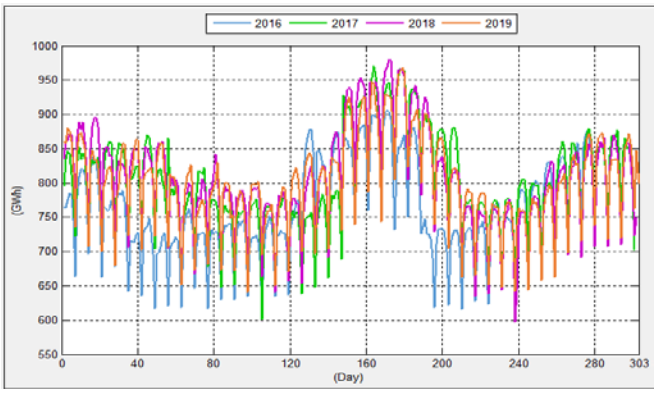

Figure 1. *Daily electricity load amount graphic for 2016, 2017, 2018 and 2019.*

In Figure 2, the average graph of the daily electricity load data by years was given.

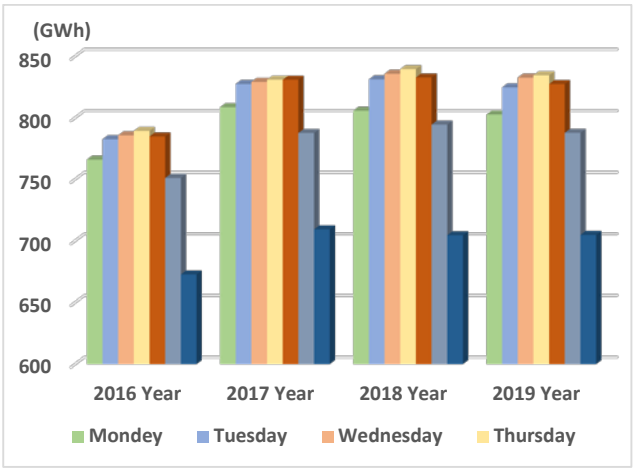

Figure 2. *Average graph of daily electric load data by years.*

When the graphs given in Figures 1 and 2 are analyzed, it is seen that the electricity load data for Tuesday, Wednesday, Thursday and Friday are similar. It is the days when the daily electricity load data falls on the weekend and becomes the lowest on Sunday. Fall and rise of load data on Saturday, Sunday and Monday are different. On weekdays, Monday has a lower load consumption than other days. On Tuesday, Wednesday, Thursday and Friday, the load values have an almost equivalent load.

Daily electricity load data for 2016, 2017, 2018 and 2019 are grouped by seasons. Table 1 contains grouping according to the seasons. When Table 1 is analyzed, the highest load consumption occurred in summer. The least load consumption occurred in the spring season. When the electrical load consumption data for years are analyzed, it is seen that the seasonal factor has an important role in load consumption.

Table 1. *Comparison of daily electricity load data for years according to seasons.*

Season	Load Consumption in 2016 (GWh)	Load Consumption in 2017 (GWh)	Load Consumption in 2018 (GWh)	Load Consumption in 2019 (GWh)
Spring	65363,42008	68393,82538	70126,25309	69991,54880
Summer	73689,86612	77602,41288	77908,35579	76836,94134
Autumn	65766,43777	70830,37170	70215,09600	70101,31634
Winter	70045,24512	73148,56772	73921,64717	73517,11743

In Figure 3, the graph of the comparison of daily electricity load data for 2016, 2017, 2018 and 2019 by seasons is given.

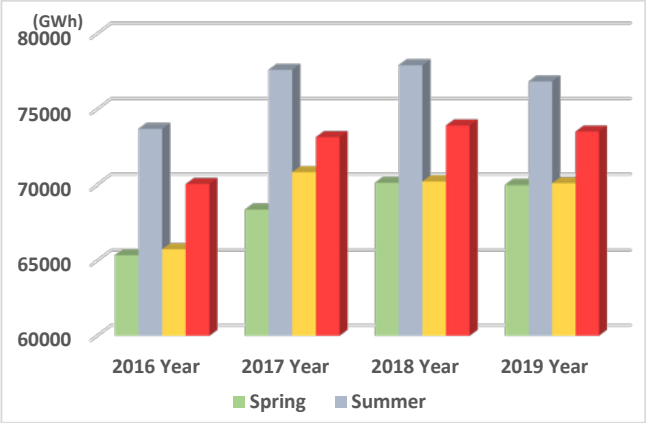

Figure 3. *Comparison chart of daily electricity load data for years by seasons.*

In this study, firstly, all of the load data are modeled without categorizing. Later, due to the similarities and differences of the load data, the data were divided into categories and applied to the model. Similarities of load data were taken into consideration in the categorization process. It was evaluated in a different category because the load data of Tuesday, Wednesday, Thursday and Friday were similar. The remaining days were evaluated in separate categories due to the change difference in load data.

Days of the week divided into categories in load estimates:

- Category 1: Tuesday, Wednesday, Thursday and Friday
- Category 2: Saturday
- Category 3: Sunday
- Category 4: Monday

Electricity market development report for 2016, 2017 and 2018 has been examined. In 2016, the highest electricity consumption was realized in Istanbul with 36.96 TWh. It corresponds to 17.39% of the total consumption [22]. In 2017, the highest electricity consumption was realized in Istanbul with 36.93 TWh. It corresponds to 17.39% of the total consumption [23]. The highest amount of electricity consumption in 2018 was realized in Istanbul with 40.45 TWh. It corresponds to 17.32% of the total consumption [24]. Considering the electricity consumption data by years, the highest consumption belongs to the city of Istanbul. The highest electricity consumption level is in Istanbul. That is why the temperature of Istanbul is discussed in this study.
In this study, the load data of the previous week (t-7) of that day is considered as the past load value. For example, Sunday data was taken one week ago as the past load data of Sunday.

2.2. Artificial Neural Networks

Artificial Neural Network (ANN), which forms a sub-branch of artificial intelligence, was developed by being inspired by the working structure of the human brain [25]. Artificial neural network is a system developed through learning. In addition to learning, it has the feature of establishing a relationship between data [26]. The ANN can be trained with past data and use them to make forward predictions.

The data set obtained for the training of ANN is categorized according to the day and season. The data were used in training and testing ANN. Daily load data of 2016, 2017 and 2018 were used in the training of ANN, and daily electricity load data for 2019 was used for model testing. Neural Network Toolbox was used in MATLAB program to train ANN. Models were created with the feed forward back propagation algorithm. Temperature and past (t-7) electrical load values were used as input data in all models. For some models, the season is considered as input value. In the models where the season is considered as the input variable, the value 1 for the winter day, 2 for the spring day, 3 for the summer day, and 4 for the autumn day. Load data of the previous week (t-7) of that day is considered as the past load value. Using the obtained data, models consisting of single hidden layer and number of hidden neurons in the range [2, 20] were performed. In the studies, the error values are minimized by adjusting the weights in the network.

The data used in models developed for short-term electricity load prediction with ANN are shown in Table 2.

Table 2. *Data and data type used in ANN models.*

ANN Models	Data Type	Day Categorization	Season Input Data	Past Load Input Data(t-7)	Temperature Input Data
Model 1	All Days	No	No	Yes	Yes
Model 2	All Days	No	Yes	Yes	Yes
Model 3	Tuesday, Wednesday, Thursday, Friday	Yes	No	Yes	Yes
Model 4	Tuesday, Wednesday, Thursday, Friday	Yes	Yes	Yes	Yes
Model 5	Saturday	Yes	No	Yes	Yes
Model 6	Saturday	Yes	Yes	Yes	Yes
Model 7	Sunday	Yes	No	Yes	Yes
Model 8	Sunday	Yes	Yes	Yes	Yes
Model 9	Monday	Yes	No	Yes	Yes
Model 10	Monday	Yes	Yes	Yes	Yes

The MAPE values of the models consisting of single layer and hidden neurons in the range [2, 20] were calculated with ANN. The MAPE values of the developed models according to the number of hidden neurons are given in Figure 4. The best MAPE value of the models was obtained when the number of hidden neurons was 8.

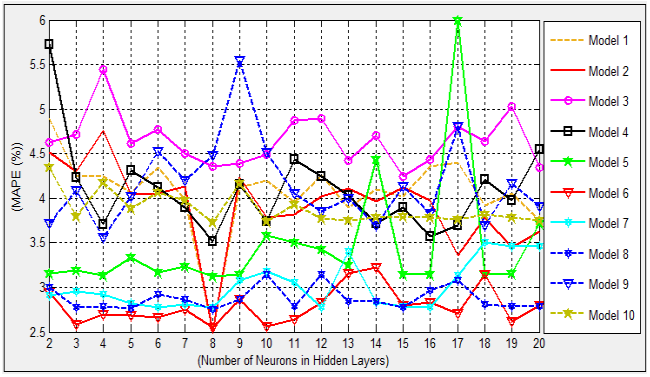

Figure 4. *Comparison graph of MAPE values according to the number of hidden neurons of the developed models.*

The best number of epochs for the model with 8 neurons in the hidden layer was found to be 1000 by trial and error. Table 3 includes the parameters used in ANN training.

Table 3. *Parameters used in ANN training.*

Algorithm	Feed Forward Back Propagation Algorithm
Training function	TRAINGDX
Learning function	LEARNGDM
Activation function	TANSIG
Number of layers	Single layer
Number of hidden layer neurons	8
Number of iterations	1000
Learning coefficient	0.01

The model using temperature, past load input variables and estimated load output variable is shown in Figure 5.

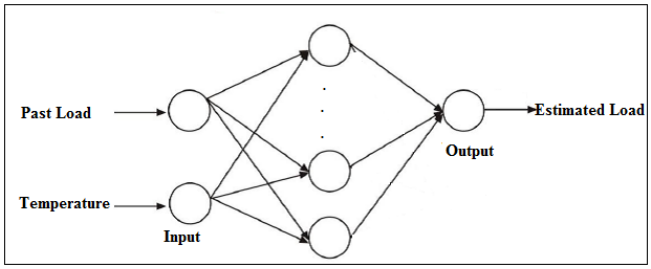

Figure 5. *ANN model developed for the first application.*

The model using temperature, past load and seasonal input variables and estimated load output variable is shown in Figure 6.

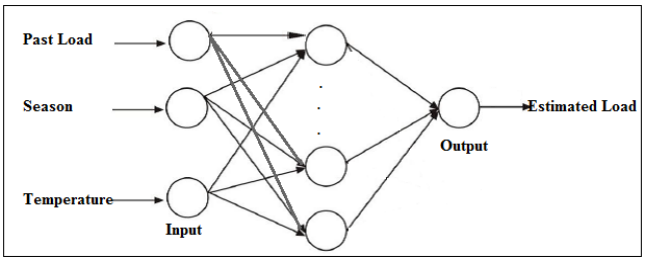

Figure 6. *ANN model developed for the second application.*

"Mean Absolute Percentage Error" was calculated in the developed models. In Equation 1, the MAPE calculation formula is applied.

$$Estimated\ Value = E,$$
$$Actual\ Value = A,$$
$$MAPE = \frac{100}{n}\sum_{k=1}^{n} |(E_k - A_k)/A_k| \,. \quad (1)$$

3. Developed load forecast models

Daily short-term electricity load and temperature values for 2016, 2017 and 2018 were obtained. These data were used in the training of the network. The daily short-term electricity load amount for 2019 has been calculated. Data on the weeks of public holidays are not processed. In MATLAB program, training was carried out using feed forward back propagation algorithm. After the network is trained, the test output data given as predicted by the network was compared with the actual values.

3.1. ANN Models

Temperature of the days and past electrical load data were used as input data in Model 1, 3, 5, 7 and 9. Temperature of days, season and past electrical load data are used as input data in Model 2, 4, 6, 8 and 10. The models were created using the estimated load output variable. Load data of the previous week's (t-7) was considered as the past load value. Output variable is the daily short-term electric load amount. In determining the seasonal input value, the value 1 for the day of the winter season, the value 2 for the day of the spring season, the value 3 for the day of the summer season, the value 4 for the day of the autumn season were used.

Figure 7 shows the graphical comparison of the estimated value of model with the actual values for all days of the week in the Model 1. In Model 1, the MAPE value was obtained as 2.53% between the actual electrical load values and the estimated electrical load values.

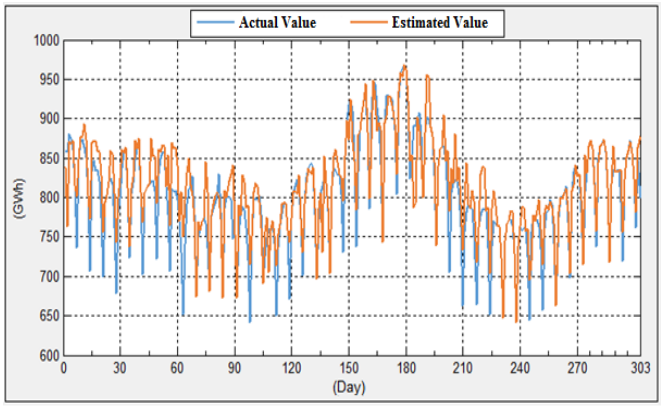

Figure 7. *Graphical comparison of actual values and estimated values in the Model 1.*

Figure 8 shows the graphical comparison of the estimated value of model with the actual values for all days of the week in the Model 2. In Model 2, the MAPE value was obtained as 2.51% between the actual electrical load values and the estimated electrical load values.

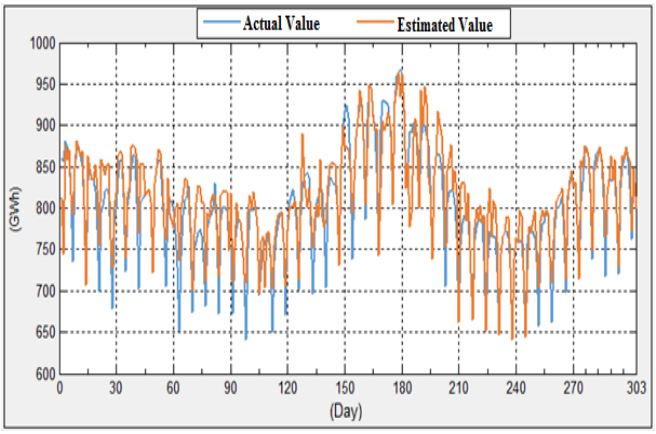

Figure 8. *Graphical comparison of real values and estimated values in the Model 2.*

Figure 9 shows the graphical comparison of the estimated value of model with the actual values in the Model 3 for Tuesday, Wednesday, Thursday and Friday. In Model 3, the MAPE value was obtained as 4.36 % between the actual electrical load values and the estimated electrical load values.

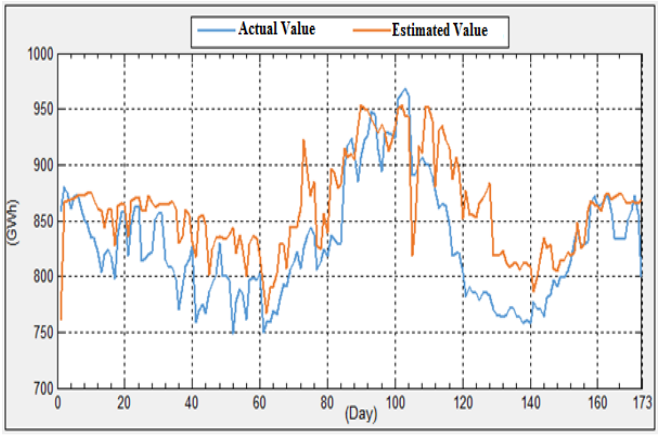

Figure 9. *Graphical comparison of real values and estimated values in the Model 3.*

Figure 10 shows the graphical comparison of the estimated value of model with the actual values in the Model 4 for Tuesday, Wednesday, Thursday and Friday. In Model 4, the MAPE value was obtained as 3.52 % between the actual electrical load values and the estimated electrical load values.

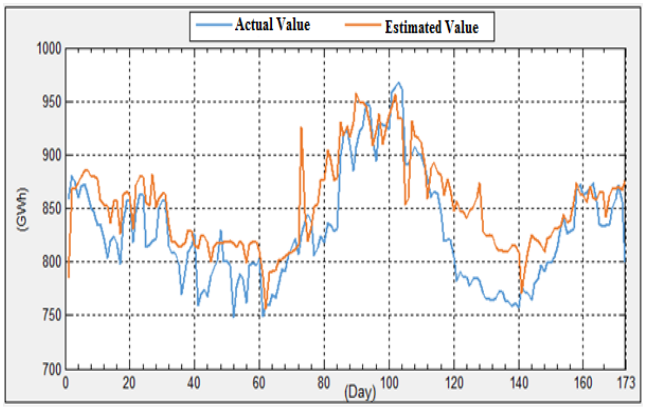

Figure 10. *Graphical comparison of real values and estimated values in the Model 4.*

Figure 11 shows the graphical comparison of the estimated value of model with the actual values in the Model 5 for Saturday. In Model 5, the MAPE value was obtained as 3.12 % between the actual electrical load values and the estimated electrical load values.

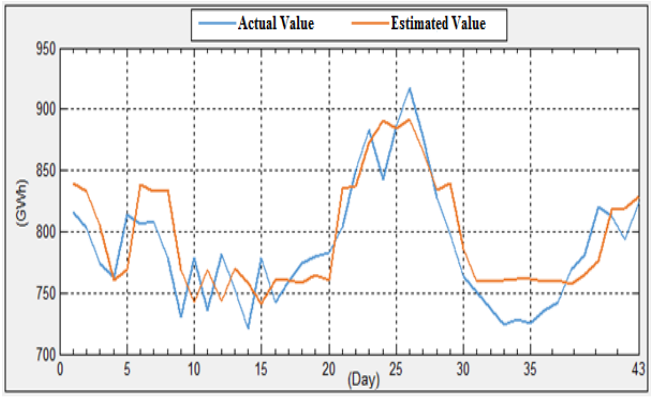

Figure 11. *Graphical comparison of real values and estimated values in the Model 5.*

Figure 12 shows the graphical comparison of the estimated value of model with the actual values in the Model 6 for Saturday. In Model 6, the MAPE value was obtained as 2.55 % between the actual electrical load values and the estimated electrical load values.

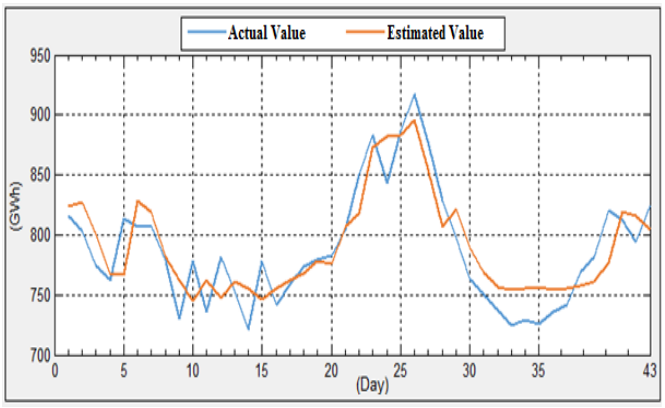

Figure 12. *Graphical comparison of real values and estimated values in the Model 6.*

Figure 13 shows the graphical comparison of the estimated value of model with the actual values in the Model 7 for Sunday. In Model 7, the MAPE value was obtained as 2.77 % between the actual electrical load values and the estimated electrical load values.

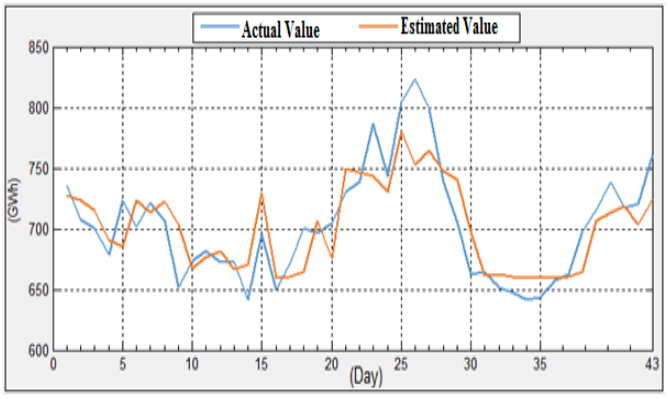

Figure 13. *Graphical comparison of real values and estimated values in the Model 7.*

Figure 14 shows the graphical comparison of the estimated value of model with the actual values in the Model 8 for Sunday. In Model 8, the MAPE value was obtained as 2.75 % between the actual electrical load values and the estimated electrical load values.

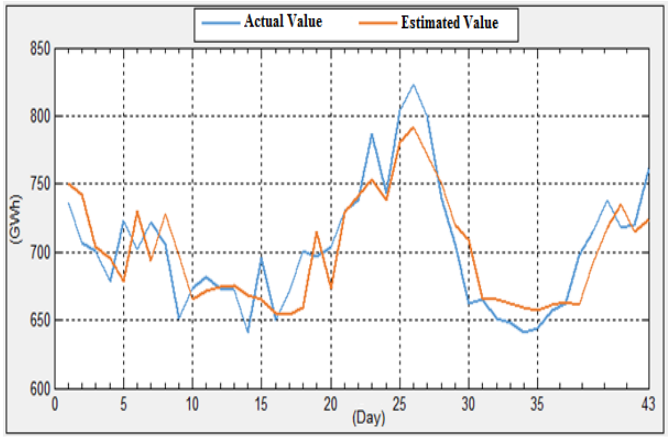

Figure 14. *Graphical comparison of real values and estimated values in the Model 8.*

Figure 15 shows the graphical comparison of the estimated value of model with the actual values in the Model 9 for Monday. In Model 9, the MAPE value was obtained as 4.48 % between the actual electrical load values and the estimated electrical load values.

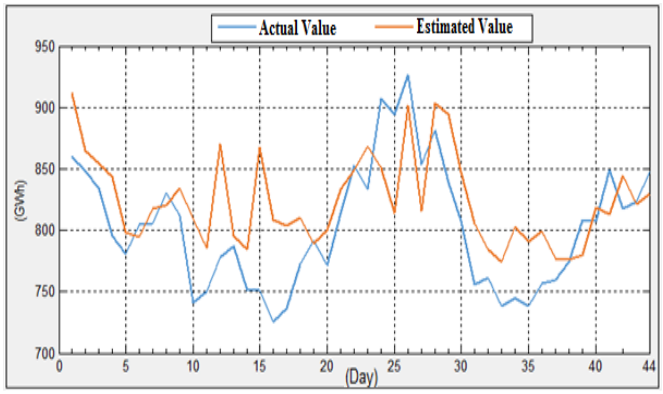

Figure 15. *Graphical comparison of real values and estimated values in the Model 9.*

Figure 16 shows the graphical comparison of the estimated value of model with the actual values in the Model 10 for Monday. In Model 10, the MAPE value was obtained as 3.73 % between the actual electrical load values and the estimated electrical load values.

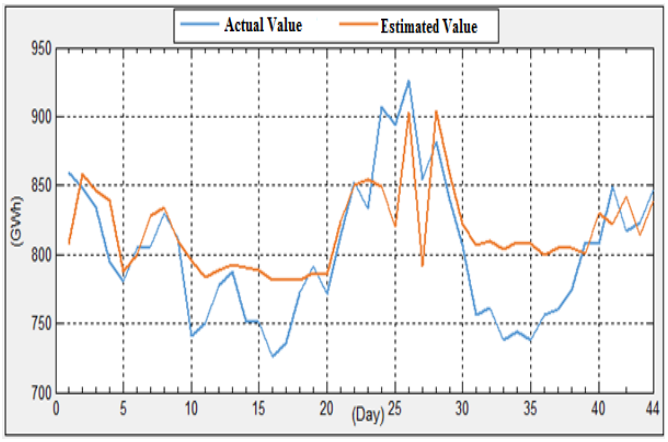

Figure 16. *Graphical comparison of real values and estimated values in the Model 10.*

3. Results

ANN has been used in this study for short term electrical load estimation. Feed forward back propagation algorithm is used as algorithm. Studies based on electric load estimation have been examined. The actual electrical load data and estimated electrical load data are compared.

Data must be obtained before making a forecast. Analysis of these data should be done well. Turkey's daily electricity consumption data are used as electrical load data. Load data for the years 2016, 2017 and 2018 were taken for training of ANN. Load data of 2019 was considered as test data. The effect of temperature on load consumption varies according to the seasons. Temperature is the most important factor in short-term electrical load estimation. The temperature of İstanbul which is Turkey's most electricity consumption province was considered.

Models were created according to data entry and the number of hidden neurons with the feed forward back propagation algorithm. seasonal data was used in some models. Due to the similarities and differences of the load data, the data were categorized and models were created. Also an evaluation was made between models. MAPE value of the models is calculated.

The graph of the MAPE values of the models created by using the feed forward back propagation algorithm is given in Figure 17. Among the models developed with ANN, the best MAPE value was obtained as 2.51% (Model 2). The addition of the season criteria has yielded a successful result.

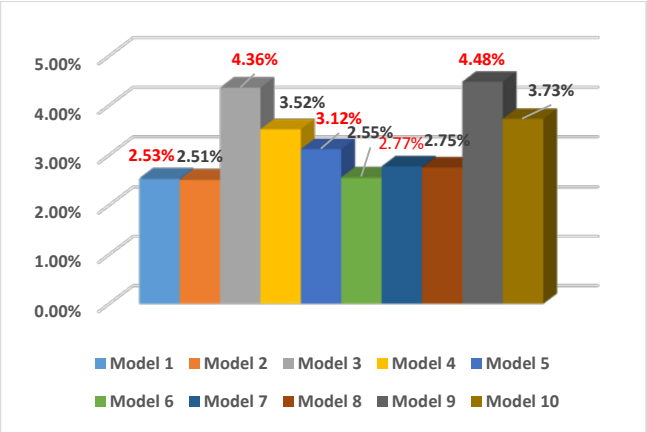

Figure 17. *MAPE values of models developed with feed forward back propagation algorithm.*

Table 4 shows the comparison of seasonal MAPE values of models developed with ANN. The red colored areas in the table show the worst MAPE values and the green colored areas show the best MAPE values. The best MAPE values were obtained in the winter season, and the worst MAPE values were obtained in the autumn and spring seasons.

Table 4. *Comparison of seasonal MAPE values of models developed with ANN.*

ANN Model	Spring MAPE Value (%)	Summer MAPE Value (%)	Autumn MAPE Value (%)	Winter MAPE Value (%)
Model 1	3,14%	2,00%	2,52%	2,35%
Model 2	3,10%	2,33%	2,51%	2,11%
Model 3	5,40%	2,85%	5,97%	2,81%
Model 4	3,13%	3,23%	4,97%	2,64%
Model 5	3,94%	2,35%	3,08%	3,20%
Model 6	2,75%	1,79%	2,87%	2,63%
Model 7	2,89%	3,59%	2,93%	2,62%
Model 8	2,84%	2,55%	2,34%	3,49%
Model 9	6,86%	4,12%	4,59%	2,82%
Model 10	3,65%	3,79%	5,27%	2,52%

5. Conflicts of interest

The results of prediction of the electrical load studies in the literature are given in Table 5. In this study, the best MAPE value was calculated as 2.51% with the ANN model. The past load has been obtained in accordance with the categorization. The categorization of the past load data and the handling of the seasonal input data enabled the MAPE value to give a successful result. It has been determined that the seasonal criterion has an important role in the estimation of the electrical load. In future studies, by using different algorithms, error values can be reduced to minimum levels, or successful results can be achieved by determining the factors affecting electrical load consumption in the input data and reducing the error rate.

Table 5. *Comparison of the MAPE values of the studies.*

Country	Year	The Data used	The Models Used	MAPE Value (%)	Load Estimated Time	Reference
Turkey	2014	Past electrical load, time zones during the day, temperature and humidity, meteorological data	Levenberg – Marquardt Model Developed by Backpropagation Algorithm	% 7.52	Short Term	(Var & Türkay, 2014)
Turkey	2015	One week prior load data and seasonal data	ANN Model Regression Model Hybrid Model	% 6,67 % 7,49 % 5,26	Short Term	(Hocaoğlu,Kaysal & Kaysal, 2015)
Turkey	2014	Gross national product and energy demand	Fuzzy Logic Model Time Series Model Regression Model	% 4,81 % 2,75 % 7,64	Short Term Yearly	(Yavuzdemir & Gökgöz, 2014)
Australia	2011	Calendar, Temperature	Semi Parametric Regression Model	% 2,81	Short Term Hourly	(Fan & Hyndman, 2011)

References

[1]. Var H., Türkay B. E., "Short term electric load forecasting using artificial neural networks", Elektronics – Computer and Biomedical Engineering Symposium, November 27-29, 2014, Bursa.

[2]. Hong T., "Short Term Electric Load Forecasting", Doctor of Philosophy, North Carolina State University, 2010.

[3]. Çevik H.H., "Short term electrical load forecasting of Turkey", Master Thesis, Electrical and Electronics Engineering, Selcuk University Institute of Science and Technology, Konya, 2013.

[4]. Başoğlu B., Bulut M., "Development of a hybrid system based on neural networks and expert systems for shortterm electricity demand forecasting", Journal of the Faculty of Engineering and Architecture of Gazi University, 32.2, (2017), 575-583.

[5]. Akman T., Yılmaz C., Sönmez Y., "Analysis of electrical load forecasting methods", Gazi Journal of Engineering Sciences, 4.3, (2018), 168-175.

[6]. Fan S., Chen L., "Short-term load forecasting based on an adaptive hybrid method", IEEE Transactions on Power Systems, 21.1, (2006), 392-401.

[7]. Hamzaçebi C., Kutay F., "Electric consumption forecasting of Turkey using articial neural netwoorks up to year 2010", Gazi University Journal of Engineering and Architecture Faculty, 19.3, (2004), 227-233.

[8]. Lee K. Y., Cha Y. T., Park J. H., " hort-term load forecasting using an artificial neural network", IEEE transactions on power systems, 7.1 (1992) 124-132.

[9]. Nie H., Liu G., Liu X., Wang Y., "Hybrid of ARIMA and SVMs for short-term load forecasting", Energy Procedia, 16, (2012), 1455-1460.

[10]. Es H., Kalender F.Y., Hamzaçelebi C., "Forecesting the energy demand of Turkey by artificial neural network", Gazi University Journal of Engineering and Architecture Faculty, 29.3, (2014), 495-504.

[11]. Yavuzdemir M. Y., Gökgöz F.T.D, "Short-term gross annual electriciy demand forecast in Turkey", Master Thesis, Ankara University Institute of Social Sciences, Department of Business Administration, Ankara, 2014.

[12]. Kaysal K., Kaysal A., Hocaoğlu F.O., "Hybrid Model for Load Forecasting (ANN and Regression)", Afyon Kocatepe University, Faculty of Engineering, Department of Electric Engineering, Turkey, (2015), 33-39.

[13]. Tümer Abdullah Erdal, Yavuz Cankat, Koçer Sabri (2018). Estimation of Unbalance Cost Due To Demand Prediction Errors Using Artificial Neural Network. Selçuk University Technology Faculty Selçuk-Technical Journal, Special Issue 2018 (ICENTE'17), 27-37.

[14]. Tümer A.E., Koçer S., Koca A. (2016, November). Estimation of the electricity consumption of Turkey trough artificial neural networks. In 2016 IEEE 17th International Symposium on Computational Intelligence and Informatics (CINTI) (pp. 000315-000318). IEEE.

[15]. Haliloğlu E.Y., Tutu B.E., "Short-term electricity power demand forecasting for Turkey", Journal of Yasar University, 13.51, (2018), 243-255.

[16]. Adepoju G.Y., Ogunjuyigbe S.O.A., Alawode K.O., Application of neural network to load forecasting in Nigerian electrical power system, Ladoke Akintola University of Technology Nigeria, The Pacific Journal of Science and Technology, vol. 8, pp., (2007), 68-72.

[17]. Fan S., Hyndman R.J., Short-term load forecasting based on a semi-parametric additive model, Monash Univ., (2011), Clayton, Australia, Augus.

[18]. Lee Y.S., Tong L.I., Forecasting energy consumption using a grey model improved by incorporating genetic programming, Energy Conversion and Management, (2011), 52 : 147–152.

[19]. Himanshu A.A., Lester C.H., Electricity demand for Sri Lanka: a time series analysis. Energy, (2008), 33, 724-739.

[20]. "EPIAS Transparency Platform", [Online]. Available: [https://seffaflik.epias.com.tr], [Accessed: September 15, 2019].

[21]. "Weather Turkey", [Online]. Available: https://www.havaturkiye.com. [Accessed: September 15, 2019].

[22]. "Electricity market 2016 market development report", T. C. Energy Market Regulatory Authority, Ankara, (2017).

[23]. "Electricity market 2017 market development report", T. C. Energy Market Regulatory Authority, Ankara, (2018).

[24]. "Electricity market 2018 market development report", T. C. Energy Market Regulatory Authority, Ankara, (2019).

[25]. Zontul M., Yangın A., "Data Mining on education publishing sector by artificial neural network tecniques", Aurum Journal of Engineering Systems and Architecture, 1.2, (2017), 1-15.

[26]. Kılıç G., "Refectory Daily demand forecast using artificial neural networks", Master Thesis, Pamukkale University Institute of Science, Denizli, 2015.

MANAS Journal of Engineering
ISSN 1694-7398 | e-ISSN 1694-7398

Volume 9, Special Issue 1, (2021) Pages 35-42
https://doi.org/10.51354/mjen.839516

Plant tissue culture of *Nicotiana tabacum* cv. TAPM 26 and its minimum inhibition against herbicide-Dalapon

Karwan Talaat Mohammed[1], Muhamad Arshad Javed[1], Fahru Huyop[1], Yilmaz Kaya[*,1,2,3]

[1] Department of Biocience, Faculty of Sciences, Universiti Teknologi Malaysia, 81310 Skudai, Johor, Malaysia

[2] Department of Biology, Faculty of Science, Kyrgyz-Turkish Manas University, 720038 Bishkek, Kyrgyzstan, yilmaz.kaya@manas.edu.kg, ORCID: 0000-0003-1506-7913

[3] Agricultural Biotechnology Department, Faculty of Agriculture, Ondokuz Mayis University, Samsun, Turkey. yilmaz.kaya@omu.edu.tr

ABSTRACT

Current study is to establish a basic plant tissue culture of *Nicotiana tabacum* TAPM 26 and test the plant tissue on resistancies against 2,2 DCP an active ingredient in herbicide-Dalapon. During micropropagation, the surface sterilization method was ascertained on seeds of tobacco. HgCl2 was used to disinfect tobacco seeds at different concentrations (0.05 gL^{-1}, 0.2 gL^{-1}, 0.5 gL^{-1} and 1.0 gL^{-1}) within three minutes. About 70% seeds were survived when exposed to 0.05 gL^{-1} of HgCl2, whereas, no seeds were germinated when sterilized at concentrations above 0.05 gL^{-1} of HgCl2. To optimize an efficient protocol of shoots and callus formation during *in vitro* regeneration, explant types and plant growth were studied. Growth regulators NAA (0.1 mgL^{-1}, 0.2 mgL^{-1}, 0.5 mgL^{-1}, 1.0 mgL^{-1} and 2.0 mgL^{-1}) and BAP (1.0 mgL^{-1}, 2.0 mgL^{-1}, 3.0 mgL^{-1} and 4.0 mgL^{-1}) were used. The explants types were one month old leaves and two weeks old cotyledons. The maximum numbers of shoots per explants were obtained from cotyledon with combination 0.1 mgL^{-1} NAA and 1.0 mgL^{-1} BAP. The highest callus fresh weight was achieved when NAA 0.5 mgL^{-1} with BAP 1.0 mgL^{-1} after four weeks. Thus, the highest number of shoots produced per explants from leaves culture on the MS media containing 0.2 mgL^{-1} NAA and 4.0 mgL^{-1} BAP. The best callus fresh weight was obtained with combination of 1.0 mgL^{-1} NAA and 1.0 mgL^{-1} BAP by using leaves explant. Finally, Dalapon (5 gL^{-1}, 10 gL^{-1}, 15 gL^{-1} and 20 gL^{-1}) were applied onto leaves and cotyledon cultures of *N. tabacum* to check on the minimum concentration of inhibition. The minimum concentration of inhibition of leaves and cotyledon cultures of *N. tabacum* was at 5 gL^{-1} of 2,2DCP but not at 10 gL^{-1}, 15 gL^{-1} and 20 gL^{-1}. This investigation will shed alight for future studies on transgenic tobacco resistant against Dalapon

ARTICLE INFO

Research article

Received: 12.12.2020
Accepted: 19.03.2021

Keywords:
seeds sterilization,
NAA,
BAP,
callus formation,
shoot regeneration,
Dalapon,
2,2 DCP

**Corresponding author*

1. Introduction

Plant tissue culture refers to the set of methods designed for growth and microprogation of an explant that grown on a specialized nutrient solutions called standard media in the aseptic condition [1, 2]. Tobacco (*Nicotiana tabacum* L.) is one of the most valuable cash crops, which belongs to the Solanaceae family [3]. Tobacco plant is an indigenous plant species found in tropical South America, South West Africa and the South Pacific [4, 5]. It has been cultivated since pre-Colombian times and separated to the world [6, 7]. Tobacco was always used as a model plant performed a main provision in advancement of plant tissue culture, transgenic research and genetic engineering over the past few decades because of its scientific uniqueness [8, 9, 10]. Tobacco is a valuable commercial plant and has become an important tool for the advancing production methods of a recombinant vaccines, pharmaceutical compounds, commercial enzymes, proteins and antibodies [11, 12, 13]. The first research on the creation of plant based vaccine was successfully achieved in tobacco with the hope of developing a less expensive product [14, 15, 16].

In plant tissue culture method, development of an efficient micropropagation technique involved in removal of plant pathogens from an infected explant source. In addition, this technique can also enhance in plant breeding systems to create new cultivars with higher profit, resistance to pathogens, pest resistance as well as weed resistance [17, 2, 18]. Tobacco has also been a favorable medium for studies of inheritance and evolution [11, 19].

The genus *Nicotiana* comprises of an approximately 70 species, in *which Nicotiana tabacum* is the most well-known in businesses as tobacco product and in academic for science development studies [20, 21]. The physiology and genetics of the Nicotiana genus has been widely explored for example its ability to regenerate into a specilised tissues to form a fully grown living organism from its de-differentiated cells. *Nicotiana tabacum* was always selected for developing of genetically modified plant model having functional of foreign genetic materials [22, 23, 24, 25, 26, 49].

The in-vitro propagation consists of numerous steps such as selection of explants, aseptic culture establishment, and multiplication of propagules, rooting and acclimatization of plantlets. However, the most critical and important step is surface sterilization for seeds or explants for culturing at sterile environment. Surface sterilization is a technique to make seeds or explants free from contamination before culturing on nutrient media [27,28,29,30,31]. Direct shoot propagation using leaves segment and cotyledons have been successfully established using tobacco [32]. On the other hand, production of regeneration plant through indirect organogenesis is also another possibility to contribute tobacco genomic enhancement [33,34]. Callus stage is widely studied in tissue culture protocols to present new desirable cultivars and generating genetically modified plants to achieve some new traits such as pesticide or herbicide resistance product [35,17,36].

Growth regulators can be defined as a small organic molecule that elicits a physiological response at very low concentration and its important components in the tissue culture media to enhance and developed pathways in plant cells product [37,38]. The concentrations of growth regulators are very critical for the control of enlargement and morphogenesis [39]. However, different type of tissue or organs considerably required various amount of substance depends on their uptake and endogenous levels [40]. The most significant classes of growth regulators are auxins and cytokinins. Auxin plays role in many development processes and required by many plant cells for adventitious root formation, swelling of tissue and somatic embryogenesis [41]. Usually, when the concentration of auxin is low, root initiation is favored but when at the high concentration, callus formation occurs [42]. Cytokinins also have important regulative roles involve in an extensive series of physiological and metabolic developments of plants, stimulate cell division, promote flowering and inhibit root cell prolongation [43].

Herbicides are commonly used to control and manage weeds but not to harm pests and organisms living in soil. Usually herbicides have to be selective in action which means capable to kill only certain plants without harming major crops [23,44,45]. Dalapon is classified by the U.S. Environmental Protection Agency (USEPA) as a general use of herbicide. According to Dikshith and Diwan [46] Dalapon is a non-color liquid with an acrid odor and it is a kind of acid usually formulates with sodium and magnesium salts. Dalapon contain an active ingredient, 2,2-dichloropropionic acid that had been used widely in Austria, central asia and some parts of the country in the world [47, 48].

The purpose of current research is to establish plant tissue culture technique on micropropagation of *Nicotiana tabacum* L. in order to form shoots and callus. This study includes the effect of Mercuric Chloride (HgCl2) on seed surface sterilization. Consequently, cultured leaves and cotyledons explant on MS [42] media at different concentrations of NAA (α-naphthaleneacidic acid) (Auxin) and BAP (6-benzylaminopurine) (Cytokinin) under aseptic conditions. Finally, the determination of Dalapon minimum inhibition of tobacco explants will be conducted through spraying method.

2. Materials and methods

2.1. Sterilization of plant materials and seed germination

Tobacco seeds were provided by Lembaga Tembakau Negera Malaysia. Selected seeds were disinfected with (0.05 gL^{-1}, 0.2 gL^{-1}, 0.5 gL^{-1} and 1.0 gL^{-1}) of Mercuric Chloride (HgCl2). Each exposure was three minutes and then the seeds were washed with sterilized water for at least three times with two minutes each. Then the seed were allowed to grow on standard growth media under pathogen-free conditions by supplying 16/8 h (light/dark) at room temperature (25±2°C).

2.2. Preparation of growth regulator for callus induction and shoot regeneration

The sterilized explants i.e leaves and cotyledons were grown on an MS media supplemented with plant growth regulators at different concentrations of α-naphthaleneacidic acid (NAA) (0.1 mgL^{-1}, 0.2 mgL^{-1}, 0.5 mgL^{-1}, 1.0 mgL^{-1} and 2.0 mgL^{-1}) and 6-benzylaminopurine (BAP) (0.0 mgL^{-1}, 1.0 mgL^{-1}, 2.0 mgL^{-1}, 3.0 mgL^{-1} and 4.0 mgL^{-1}). Cotyledon section and leaves with an approximately 0.5-1cm were grown on a primary standard solid MS media under a photosynthetic photon flux density (PPFD) of 26 µmol m^{-2} delivered by cool white fluorescent tubes with a photoperiod of 16/8 h (day/night) at 25±2°C. In the medium, these cotyledons were allowed to develop for at least two weeks and leaves for one month for shoot and callus regeneration.

The basic tissue culture experiment had three replicates, with more than 75 explants plated for each batch. For each plate containing MS medium for callus and shoot induction different concentrations of NAA (0.1, 0.2, 0.5, 1.0 and 2.0 mgL^{-1}) and BAP (0.0, 1.0, 2.0, 3.0 and 4.0 mgL^{-1}) were prepared. The pH of the media was adjusted to pH 5.7 ± 1 prior to autoclaving for 20 min at 121 °C. After autoclaving, the MS media was allowed to cool at room temperature. Then, 20 mL medium was dispensed into culture tube. All culture media were maintained at room temperature for growth. The

culture media was monitored for shoot production and callus fresh weight per explant at weekly intervals throughout 4 weeks period of time.

2.3. Application of herbicide Dalapon on Nicotiana tabacum

Herbicide Dalapon was prepared at different concentrations from 5 gL^{-1}, 10 gL^{-1}, 15 gL^{-1} and 20 gL^{-1}. Then, the two months old tobacco plant was sprayed with different concentrations of Dalapon and its minimum inhibition/resistancy was monitored.

3. Results and discussion

3.1. Effects of Mercuric Chloride ($HgCl_2$) on Survival of Tobacco Seeds

Table 1 shows the % of seeds survived when washed with various concentrations of $HgCl_2$. The maximum number of seeds germinated was obtained at 0.05 gL^{-1} of $HgCl_2$. However, seeds washed with $HgCl_2$ at 0.2, 0.5, and 1.0 gL^{-1} were not survived suggesting at higher concentrations of $HgCl_2$ was too toxic to the seeds. Fig. 1. supported Table 1 showing the total number of seeds placed on MS media. It was 25 seeds per petri dishes with three replicates for each treatment. This observation was in agreement with the findings of Azeem et al. [6], that seed washed with 0.05gL^{-1} of $HgCl_2$ showed a good growth. At 0.05 gL^{-1} of $HgCl_2$the seed coat is free from contaminants, without killing the seeds. There are many scientific finding of surface sterilization in tobacco tissue culture using $HgCl_2$. [50].

Table 1. *The effects of different concentrations of HgCl2 on seeds germination. Concentrations above 0.05 HgCl2(gL^{-1}) inhibit seeds germination*

Concentrations of $HgCl_2$ (gL^{-1})	Time (min)	Seed germination (%)
0.05	3	70
0.2	3	0
0.5	3	0
1.0	3	0

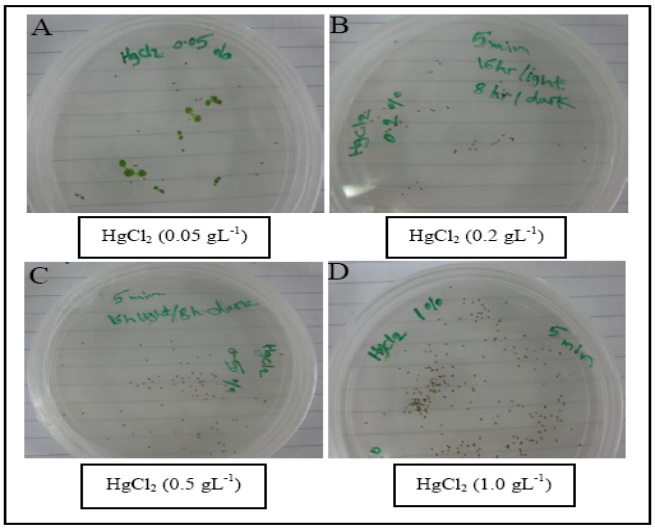

Figure 1: *The growth of tobacco seeds after treated with various concentrations of $HgCl_2$; (A) the seeds still showing some growth at 0.05 gL^{-1} of ($HgCl_2$). The concentrations of Mercuric Chloride at 0.2, 0.5, 1.0 gL^{-1}, on plates B, C and D, respectively showing no seeds germination after two weeks in culture.*

3.2. Effect of Auxins and Cytokinins on Shoot Formation from Cotyledon Explants

The purpose of the following experiments were to evaluate the explants (cotyledon and leaves) for their callus and shoot formation at different concentrations of NAA and BAP supplied in MS medium. Cotyledon is important primary explants used, due to their reliability and simplicity for micropropagation [51]. Moreover, *in vitro* tobacco seed germination needed little period of time to produce cotyledons from seeds in about two weeks. In addition, the combination concentration of plant growth regulators had been applied to find suitable effect of cotyledon explants on shoot/callus formation.

Figure 2 shows the maximum number of shoots (average of 7.66± 0.23 shoots/explant) per explant (cotyledon) was obtained at combination of both concentrations NAA: BAP, 0.1 mgL^{-1} NAA and 1.0 mgL-1 BAP, respectively. The minimum shoot per explants was obtained at 0.5 mgL^{-1} NAA and 0.0 BAP. This observation was taken after four weeks of culture. The results seen based on different concentrations of plant growth regulators that had been added into MS media as well as explants type. BAP was essential factor for shoot proliferation, whereas poor shoot development occurred on the media without cytokinins. In fact, certain explants will be more responsive than the others for instance the cotyledon of some species regenerate shoot better than true leaves or stems [39, 52].

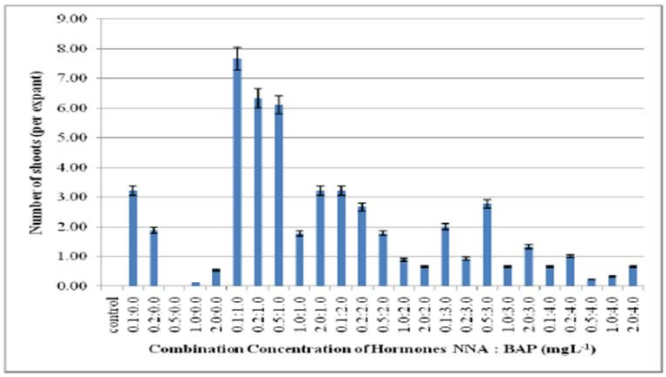

Figure 2. *The effects of both NAA and BAP on number of shoots produced per explant in cotyledon culture*

3.3. Effect of Combination Concentration of Auxins and Cytokinins on the Mean Callus Weight from Cotyledon Explants

The efficacy of BAP and NAA on callus induction was observed from cotyledon explants. The callus were induced in three weeks by taking cotyledon explants from in vitro grown plants on MS media supplemented with selected concentrations of BAP and NAA. Figure 3 illustrates the highest mean weight of callus formation was 4.02 g when NAA 0.5 mgL^{-1}: BAP 1.0 mgL^{-1} on MS media. In this experiment, the lowest mean weight of callus was 0.15 g when supplied by 0.2 mgL^{-1} NAA: 3.0 mgL^{-1} BAP. Abaxial surface of leaves disc in touch with media is better than adaxial surface due to a large number of somates on the abaxial surface [53]. Callus formation can be affected by explants type, concentration combination, growth media and type of the plant growth regulators [54].

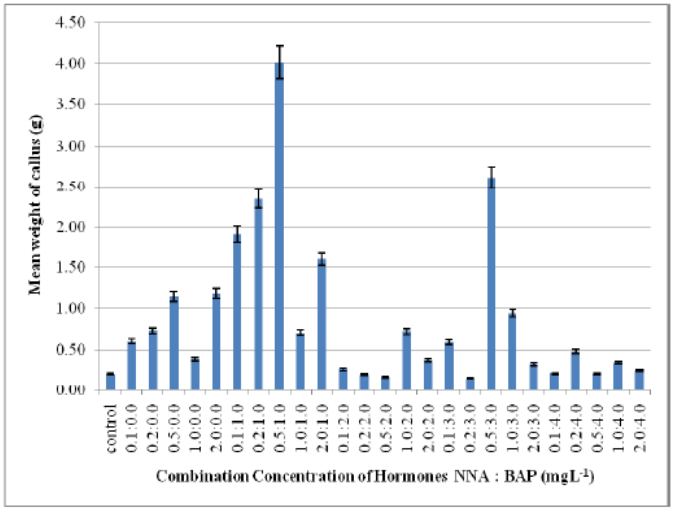

Figure 3 *The effects of both NAA and BAP on fresh callus weight gained from cotyledon culture*

3.4. Effect of Combination Concentration of Auxins and Cytokinins on the Shoot Formation from Leaf Explant

BAP and NAA were used to investigate the number of shoots induction from leaves culture. The effects of plant growth regulators on shoots proliferation were examined using leaves explant. After four weeks of culture, the numbers of shoots per explants were recorded. Previous study has shown that BAP was one of the most effective among the other cytokinins for inducing shoot development [55,56]

Figure 4 shows that the highest numbers of shoots per explants were obtained on the media containing 0.2 mgL^{-1} NAA and 4.0 mgL^{-1} BAP which produced shoots per explants. This number significantly decreased on media supplemented with NAA 0.1 mgL^{-1}: BAP 3.0 mgL-1 that was slightly different from NAA 0.1 mgL^{-1} : BAP 2.0 mgL-1 which formed 8.88 and 8.55 number of shoots per explants respectively. On the other hand, the lowest number of shoots per explants were obtained when 0.1 mgL-1 NAA: 0.0 mgL-1 BAP, 2.0 mgL-1 NAA : 0.0 mgL-1 BAP, while 2.0 mgL-1 NAA : 2.0 mgL-1 BAP resulted in no shoot formation at all.

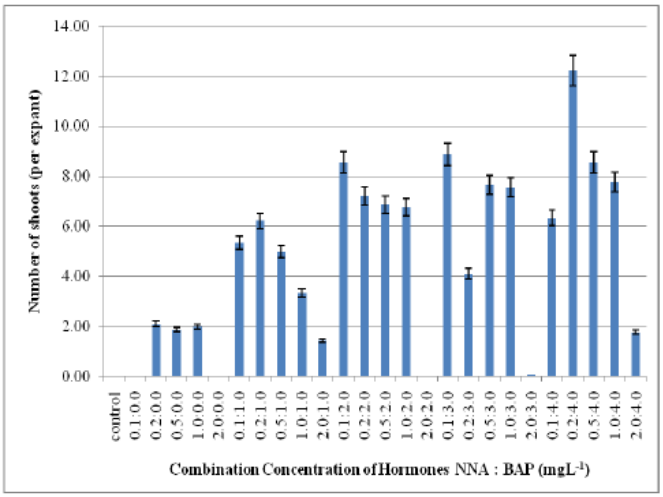

Figure 4 *The effects of both NAA and BAP on shoot proliferation from leaves culture*

3.5. Effect of Combination Concentration of Auxins and Cytokinins on the Mean Callus Weight from Leaf Explant

Callus induction is significantly depending on explants type. Calli was induced by using leaf explants from *in vitro* grown plants during four weeks on MS media supplemented with various concentrations of plant growth regulators. Induction in monocots callus requires long time for its initiation [51,57]. Figure 5 shows the highest callus weight was achieved on medium supplemented with hormone combination of 1.0 mgL^{-1} NAA: 1.0 mgL^{-1} BAP that was 14.8 g of fresh callus weight. The second best was slightly lower than the previous one that was gained at 2.0 mgL^{-1} NAA: 4.0 mgL^{-1} BAP which recorded only 14.72 g of fresh callus. However, the lowest fresh callus formation was obtained at 0.1 mgL^{-1} NAA: 0.0 mgL^{-1} BAP.

Figure 6 illustrates the effect of Dalapan on tobacco plant after two weeks. Therefore, it was concluded that successful callus formation had been achieved base on plant growth regulators and their combination. The results showed that leaves culture was more efficient to gain better callus fresh weight than using cotyledon culture.

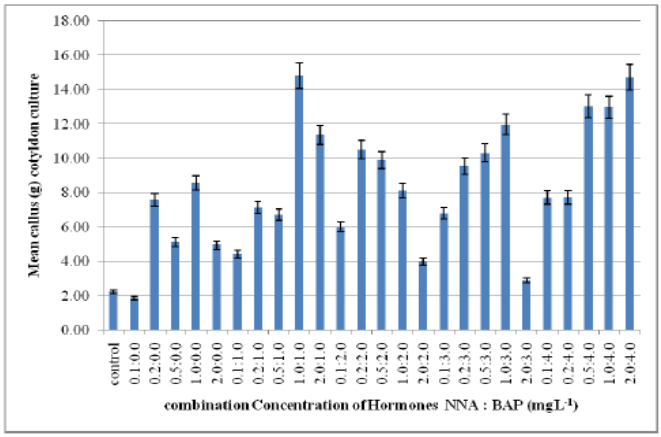

Figure 5. *The effects of both NAA and BAP on fresh callus weight gained from leaves culture*

3.6. Effect of Dalapon via spraying method

Dalapon is a selective herbicide which can only kill the weeds but not directly kill desired plant. The growth of tobacco plant was inhibited using Dalapon at high concentrations. The leaves became bigger but wilt due to the mode of action of Dalapon that affect the plant growth. The uptake of Dalapon was done through the leaves, translocate to other plant tissues.

Table 2. *The Effects of various concentrations of herbicide Dalapon on tobacco growth after two weeks in culture*

Concentrations of Dalapon	**5 gL^{-1}**	**10 gL^{-1}**	**15 gL^{-1}**	**20 gL^{-1}**
Observations	Plant Still remains in healthy condition	Leaves and stems begin to change the color to yellow	Plants unable to survive	Plants were dead

Table 2 shows several concentrations of Dalapon that had been used and its effect after two weeks in culture. Figure 6 shows that Dalapon at 5 gL^{-1} has no effect on plant after two weeks in culture. Above 5 gL^{-1} of Dalapon showed death to the plant tissue.

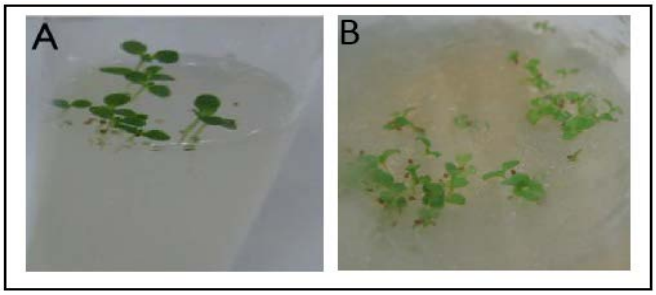

Figure 6 *The effect of Dalapon on tobacco plant after two weeks. (A) all plant parts were in a good condition when exposed to 5 gL^{-1} Dalapon. (B) at 10 gL^{-1} Dalapon caused changes in the color of leaves and started to wilt and die*

4. Conclusions

This study underlined the important technique for tobacco seeds surface sterilization by using Mercuric Chloride ($HgCl_2$) at different concentrations. The effects of plant growth regulators on micropropagation of *Nicotiana tabacum* from cotyledons and leaf explants were established. The micropropagation of two different types of explants showed different number of shoots produced per explants as well as callus fresh weight. Combination of BAP and NAA had been applied to find out the effects on callus fresh weight and number of shoots per explants. Dalapon was also used as herbicide to determine the resistancy of tobacco against Dalapon at minimum inhibition concentration. The establishment of the current study may shed alight in future experiment to transform dehalogenase gene into plant tissue culture for developing plant resistant to herbicide.

Acknowledgment

We thank Farough Motasemi for checking the analysis. Lastly, the authors offer regards and blessings to all of those who supported this work until completion of the project.

References

[1]. Bidabadi S.S., Jain S.M., “Cellular, Molecular, and Physiological Aspects of In Vitro Plant Regeneration”, Plants, 9, (2020), 702.

[2]. Mohammed S., “Effects and quantity ranges of some auxins on embryogenic callus induction from upland rice cultivars: An overview”, International Journal of Life Sciences and Biotechnology, 3(2), (2020), 197-204.

[3]. Popova V., Ivanova T., Stoyanova A., Nikolova V., Hristeva T., Zheljazkov V.D., “GC-MS Composition and Olfactory Profile of Concretes from the Flowers of

Four Nicotiana Species", Molecules, 25(11), (2020), 2617. https://doi.org/10.3390/molecules25112617.

[4]. Nielsen M.T., "Tobacco. Outlook on Agriculture" 16(2), (1987), 77–81.

[5]. Charlton A.,"Medicinal uses of tobacco in history", Journal of the Royal Society of Medicine, 97(6), (2004), 292–296.

[6]. Azeem S.A, Ullah I., Ali M., Khan A., Bakht J.S.A., "Effects of different sterility on seeds and Callusing frequency as effected by hormones in Nicotiana tabacum L.", Biofrontiers, 1, (2010), 62-67.

[7]. Gebhardt C., "The historical role of species from the Solanaceae plant family in genetic research", Theoretical and Applied Genetics, 129(12), (2016), 2281-2294.

[8]. Kumar V., Maherchandani N., "Differentiation in callus cultures of a tobacco (Nicotiana tabacum cv. White Burley) variant: some biochemical aspects", Plant Cell, Tissue and Organ Culture, 14, (1988), 177-185.

[9]. Kaya Y., Yilmaz S., Marakli S., Gozukirmizi N., Huyop F., "Transformation of Nicotiana tabacum with DehE Gene", Journal of Food Agriculture and Environment, 11(3-4), (2013) ,777-780.

[10]. Kaya Y., Yilmaz S., Gozukirmizi N., Huyop F.,"Evaluation of transgenic Nicotiana tabacum with dehE gene using transposon based IRAP", American Journal of Plant Sciences, 4, (2013), 41-44.

[11]. Ganapathi T., Suprasanna P., Rao P.S., Bapat V., "Tobacco (Nicotiana tabacum L.)-A model system for tissue culture interventions and genetic engineering", Indian Journal of Biotechnology, 3, (2004), 171-184.

[12]. Ma J.K., Drossard J., Lewis D., Altmann F., Boyle J., Christou P., Cole T., "Regulatory approval and a first-in-human phase I clinical trial of a monoclonal antibody produced in transgenic tobacco plants", Plant Biotechnology Journal, 13(8), (2015), 1106–1120.

[13]. Habibi P., Daniell H., Soccol C.R., Grossi-de-Sa M.F., "The potential of plant systems to break the HIV-TB link" Plant Biotechnology Journal, 17(10), (2019), 1868-1891.

[14]. Phan H.T., Pohl J., Floss D.M., Rabenstein F., Veits J., Le B.T., Chu H.H., Hause G., Mettenleiter T., Conrad U., "ELPylated haemagglutinins produced in tobacco induce potentially neutralizing antibodies against H5N1 virus in mice", Plant Biotechnology Journal, 11, (2013), 582–593.

[15]. Zhong X., Qi G., Yang J., Xing G., Liu J., Yang X., "High-efficiency expression of a receptor-binding domain of SARS-CoV spike protein in tobacco chloroplasts" Sheng Wu Gong Cheng Xue Bao 30(6), (2014), 920-930.

[16]. Demurtas O.C, Massa S., Illiano E., De Martinis D., Chan P.K, Di Bonito P., Franconi R., "Antigen production in plant to tackle infectious diseases flare up: The case of SARS", Frontiers in Plant Science, 7, (2016), 54-57.

[17]. Yan M.M., Xu C., Kim C.H., Um Y.C., Bah A.A., Guo D.P., "Effects of explant type, culture media and growth regulators on callus induction and plant regeneration of Chinese jiaotou (Allium chinense)", Scientia Horticulturae", 123(1), (2009),124–128.

[18]. Gourguillon L., Rustenholz C., Lobstein A., Gondet L., "Callus induction and establishment of cell suspension cultures of the halophyte Armeria maritima (Mill.) Willd", Scientia Horticulturae, 233, (2018), 407–411.

[19]. Mehmood F., Abdullah U.Z., Shahzadi I., Ahmed I., Waheed M.T., Poczai P., Mirza B., "Plastid genomics of Nicotiana (Solanaceae): insights into molecular evolution, positive selection and the origin of the maternal genome of Aztec tobacco (Nicotiana rustica)", Peer Journal, 8, (2020), e9552.

[20]. Olmstead R.G., Bohs L., Migid H.A., Santiago-valentin E., "Molecular phylogeny of the Solanaceae", Molecular Phylogenetics and Evolution, 57, (2008), 1159–1181.

[21]. Dupin J., Matzke N.J., Särkinen T., Knapp S., Olmstead R.G., Bohs L., Smith S.D., "Bayesian estimation of the global biogeographical history of the Solanaceae", Journal of Biogeography, 44(4), (2016), 887–899.

[22]. Suzuki K., Ichiro Y., Nobukazu T., "Tobacco plants were transformed by Agrobacterium rhizogenes infection during their evolution", The Plant journal, 32, (2002), 775-787.

[23]. Kaya Y., Marakli S., Gozukirmizi N., Mohamed E., Javed M.A., Huyop F., "Herbicide Tolerance Genes Derived from Bacteria", The Journal of Animal and Plant Sciences, 23(1), (2013), 85-91.

[24]. Kanwal M., Joyia F.A., Mustafa G., Zia M.A., Rana I. A., Khan M.S., "Direct in vitro regeneration of Nicotiana plumbaginifolia L. and the potential for genetic transformation", International Journal of Horticulture, 7(6), (2017), 40-46.

[25]. Liu H., Kotova T.I., Timko M.P., "Increased leaf nicotine content by targeting transcription factor gene expression in commercial flue-cured tobacco (Nicotiana tabacum L.)", Genes(Basel), 10(11), (2019), 930-935.

[26]. Sun H, Sun X, Wang H, & Ma X., "Advances in salt tolerance molecular mechanism in tobacco plants", Hereditas,157(5), (2020),1-6.

[27]. Makenzi N.G., Mbinda W.M., Okoth R.O., Ngugi M.P., "In vitro plant regeneration of sweet potato through direct shoot organogenesis", Journal of Plant Biochemistry and Physiology, 6(1), (2018), 207-210.

[28]. Latifian E., Arvas Y.E., Kaya Y., "Tagetes minuta bitkisinin mikro üretimi üzerinefarklı BAP ve IAA konsantrasyonlarının etkileri", International Journal of Life Sciences and Biotechnology,1(2), (2018), 96-104.

[29]. Kaya Y., Karakutuk S., "Effects of different growth regulators on regeneration of Turkish upland rice", Anadolu Tarım Bilimleri Dergisi 33(3), (2018), 226-231.

[30]. Aboshama H.M., Atwa M.M., "In vitro Evaluation of Somaclonal Variation of Two Potato Cultivars Santana and Spunta for Resistance against Bacterial Blackleg Pectobacterium atrosepticum", Journal of Plant Biochemistry & Physiology, 7(3), (2019), 243-253.

[31]. Mangena P., "Benzyl adenine in plant tissue culture-succinct analysis of the overall influence in soybean [Glycine max (L.) Merrill.] seed and shoot culture establishment", Journal of Biotech Research, 11, (2020), 23-34.

[32]. Hussein N.B.M., Huyop F., Kaya Y., "An easy and reliable method for establishment and maintenance of tissue cultures of Nicotiana tabacum cv. TAPM 26", International Journal of Science Letters, 2(2), (2020), 62-71.

[33]. Kutty P.C., Parveez G.K.A., Huyop F., "An easy method for Agrobacterium tumefaciens-mediated gene transfer to Nicotiana tabacum cv. TAPM26", Journal of Biological Sciences, 10(6), (2010), 480-489.

[34]. Kutty P.C., Parveez G.K.A., Huyop F., "Agrobacterium tumefaciens-infection strategies for greater transgenic recovery in Nicotiana tabacum cv. TAPM26", International Journal of Agricultural Research", 6(2), (2011), 119-113.

[35]. Geethalakshmi S., Balakrishnan H., Natarajan S., "Optimization of media formulations for callus induction, shoot regeneration and root induction in Nicotiana benthamiana", Journal of Plant Science & Research, 3(1), (2016), 150-154.

[36]. Eibl R., "Plant cell culture technology in the cosmetics and food industries : current state and future trends", Applied Microbiology and Biotechnology, 102(20), (2018), 8661– 8675.

[37]. Al-remi F., Arvas Y.E., Durmuş M., Kaya Y.,"Tomato Plant and Its In Vitro Micropropagation", Journal of Engineering Technology and Applied Sciences, 3(1),(2018), 57-73.

[38]. Arvas Y.E., Aksoy H.M., Kaya Y., "Patates bitkisinde biyoteknolojik çalışmalar", International Journal of Life Sciences and Biotechnology, 1(1), (2018), 37-47.

[39]. Ali G., Fazal H., Zahir A., Muhammad T., Muhammad A.K., "Callus Induction and in vitro Complete Plant Regeneration of Different Cultivars of Tobacco (Nicotiana tabacum L.) on Media of Different Hormonal Concentrations", Biotechnology, 6, (2007), 561-566.

[40]. Vissenberg K., Feijo J.A., Weisenseel M.H., Verbelen J. P., "Ion fluxes, auxin and the induction of elongation growth in Nicotiana tabacum cells", Journal of Experimental Botany, 52, (2001), 2161-2167.

[41]. Eklof S., Astot C., Sitbon F., Moritz T., Olsson O., Sandberg G., "Transgenic tobacco plants co-expressing Agrobacterium iaa and ipt genes have wild-type hormone levels but display both auxin- and cytokinin-overproducing phenotypes", The Plant Journal, 23(2), (2000), 279–284.

[42]. Skoog F., Miller C.O., "Chemical regulation of growth and organ formation in plant tissues cultured in vitro", Symposia of the Society for Experimental Biology, 54, (1957), 118–130.

[43]. Allawzi M., Kandah M.I., "Parametric study of biodiesel production from used soybean oil", European Journal of Lipid Science and Technology, 110, (2008), 760-767.

[44]. Duke S.O., Scheffler B.E., Boyette C.D., Dayan F.E., "Biotechnology in weed control. In: Kirk-Othmer encyclopedia of chemical technology" Wiley, New York, pp 1–25, (2015).

[45]. Beckie H.J., Ashworth M.B., Flower K.C., "Herbicide resistance management: recent developments and trends", Plan Theory, 8(6), (2019),161-167.

[46]. Dikshith T.S., Diwan P.V., Industrial Guide to Chemi and Drug Safety, (2003), John Wiley&Sons,Inc.

[47]. Hawker D.W., Cumming J.L., Watkinson A., Bartkow M.E., "The occurrence of the herbicide dalapon (2,2-dichloropropionate) in potable water as a disinfection by-product", Journal of Environmental Monitoring, 13(2), (2011), 252–256.

[48]. Akcay K., Yilmaz K., "Isolation, characterization and molecular identification of a halotolerant Bacillus megaterium CTBmeg1 able to grow on halogenated compounds", Biotechnology & Biotechnological Equipment, 33:1, (2019), 945-953, DOI: 10.1080/13102818.2019.1631717 .

[49]. Arvas Y. E., & Kaya Y., "Genetiği değiştirilmiş bitkilerin biyolojik çeşitliliğe potansiyel etkileri" Yüzüncü Yıl Üniversitesi Tarım Bilimleri Dergisi, 29(1), (2019), 168-177.

[50]. Neelu J., "In vitro growth and shoot multiplication in Nicotiana tabacum L.-Influence of gelling agent and carbon source", International Journal of Plant Developmental Biology, 3(1), (2009), 23-29.

[51]. Mehmood F., "Effect of different parameters on transformation and regeneration of nodal and leaf explants of Nicotiana tabacum cv. Petiat Havana. " Master thesis, (2016)., Quaid-i-Azam University, Islamabad, Pakistan.

[52]. Monthony A.S., Page S.R., Hesami M., Jones A.M.P., "The Past, Present and Future of Cannabis sativa Tissue Culture", Plants (Basel, Switzerland), 10(1), (2021), 1-10, DOI: 10.3390/plants10010185.

[53]. Dhaliwal H.S., "Competence and determination during Shoot and Root Organogenesis in vitro" Master of Science Thesis, (1998), University of Calgary, Canada.

[54]. Attfield E.M., Evans P.K., "Developmental pattern of root and shoot organogenesis in cultured leaf explants of Nicotiana tabacum", Journal of Experimental Botany, 42, (1991), 51-57.

[55]. Stolarz A., Macewicz J., Lörz H., "Direct somatic embryogenesis and plant regeneration from leaf explants of Nicotiana tabacum L.", Journal of Plant Physiology, 137(3), (1991), 347–357.

[56]. Vajjiram C., Vanitha A., Kalimuthu K., "Ftir and gc-ms analysis of bioactive compounds in ethanol extract of tobacco callus (Nicotiana tabacum)", World Journal of Pharmaceutical Research, 6(14), (2017), 530-545.

[57]. Gelvin S.B., "Agrobacterium-Mediated Plant Transformation: the Biology behind the "Gene-Jockeying" Tool", Microbiology and molecular biology reviews, 67(1), (2003), 16-37.

MANAS Journal of Engineering
ISSN 1694-7398 | e-ISSN 1694-7398

Volume 9, Special Issue 1, (2021) Pages 43-48
https://doi.org/10.51354/mjen.859016

Molecularly-imprinted silica nanoparticles for rapid and selective detection of atenolol in artificial urine samples

Adem Zengin

Van Yuzuncu Yil University, Faculty of Science, Department of Chemistry, 65080 Van-Turkey,
ademzengin@yyu.edu.tr, ORCID: 0000-0002-6889-5387

ABSTRACT

Herein, a novel molecularly imprinted polymer was synthesized on silica nanoparticles via surface imprinting approach for rapid, sensitive and selective detection of atenolol in artificial urine samples. For this purpose, silica nanoparticles were firstly modified with methacryloxy group for surface initiated polymerization and then, polymerization was carried out in the presence of 2-hydroxyethyl methacrylate (functional monomer), ethylene glycol dimethacrylate (cross-linker), azobisisobutyronitrile (initiator), atenolol (template) and acetonitrile (porogen). The surface characterization of imprinted nanoparticles indicated that a thin polymer layer was grafted on the silica nanoparticles. The rebinding properties of the imprinted nanoparticles were investigated in detail and the results revealed that the imprinted nanoparticles had high adsorption capacity (32.06 mg/g), fast adsorption kinetics (15 min for equilibration), high imprinting factor (4.14) towards atenolol and good regeneration ability. The imprinted nanoparticles were also used as selective sorbent for selective extraction and determination of atenolol in artificial urine samples. The results showed that the proposed method good recovery percentages (98.6 %-100.1%) with low standard deviations (less than 4.4%). It is believed that the atenolol-imprinted silica nanoparticles can be used as an alternative sorbent for selective quantification of atenolol in artificial urine samples.

ARTICLE INFO

Research article

Received: 12.01.2021
Accepted: 11.03.2021

Keywords:
molecularly-imprinted polymers,
surface imprinting,
silica nanoparticles,
atenolol,
artificial urine

1. Introduction

Molecular imprinting is a powerful method for the creation of selective binding sites for target molecules in polymer networks [1]. The formed binding sites are complementary to target molecules in shape, size, and functional group orientations [2]. Molecularly-imprinted polymers (MIPs) can be easily synthesized in the presence of functional monomer, template (target) molecule, cross-linker, initiator and porogen (solvent). Due to the superior features of MIPs such as high thermal, mechanical and chemical stability, long durability without loss their selective recognition ability and robustness, MIPs are generally used in separation/purification technologies [3], catalysis [4], sensors [5], environmental and food testing [6] and many other practical applications [7].

Atenolol is a type of *β*-blocker and generally used for treatment of cardiovascular disorders such as angina pectoris, myocardial infarction, cardiac arrhythmias, and hypertension [8]. Atenolol reduces tremors and heart attacks and often used by athletes for improving their performance. Therefore, atenolol is classified as anti-doping agent and the usage of atenolol is banned by the World Anti-Doping Agency (WADA) [9]. As a result, determination of atenolol in biological samples is an important issue.

There have been several analytical methods such as high performance liquid chromatography (HPLC) [10], liquid chromatography-mass spectrometry (LC-MS) [11], gas chromatography-mass spectrometry (GC-MS) [12], potentiometry [13], spectrofluorimetry [14], and enzyme-linked immunoassay (ELISA) [15] reported for determination of atenolol in different biological samples. The aforementioned chromatographic methods are generally suffer from pure selectivity due to the presence of potential interferences which limits sensitivity of the methods. Moreover, chromatographic methods requires high cost equipment, large solvent consumption, complicated sample pre-treatment steps, requiring highly skilled operators. ELISA is the most preferred method for determination of drugs in clinical applications but the method has some drawbacks such as cross-reactivity of endogenous molecules, single use, the need for a highly skilled operators. Especially, spectrofluorimetric methods also suffer from potential fluorescent interferences in biological samples. Therefore, an

effective, sensitive and selective analytical method is necessary for the determination of atenolol in biological samples.

Herein, a novel analytical method was presented for selective extraction and sensitive determination of atenolol in artificial urine sample based on surface imprinting approach. For this purpose, 3- methacryloxypropyl trimethoxysilane (MPS) modified silica nanoparticles (MPS@SiO_2 NPs), 2-hydroxyethly methacrylate (HEMA), atenolol, ethylene glycol dimethacrylate (EGDMA), azobisisobutyronitrile (AIBN), and acetonitrile (ACN) were used as supporting material, template molecule, cross-linker, initiator and porogen, respectively. Surface characterization was conducted to verify grafting of the imprinted polymer. Rebinding properties of atenolol on the imprinted/non-imprinted polymer were investigated in detail. Moreover, the prepared atenolol-imprinted nanoparticles (MIP@SiO_2 NPs) were used as selective sorbent for extraction of atenolol and its quantification by spectrofluorimetry in artificial urine samples.

2. Materials and methods

3- methacryloxypropyl trimethoxysilane (MPS), 2-hydroxyethly methacrylate (HEMA), tetraethyl orthosilicate (TEOS) and ethylene glycol dimethacrylate (EGDMA) were purchased from Sigma-Aldrich and used as received unless otherwise noted. Azobisisobutyronitrile (AIBN) was provided by Across Organics and recrystallized twice from methanol. Atenolol, propranolol and pindolol were supplied by Alfa Aesar Chemicals and used as received.

2.1. Preparation of SiO_2 NPs

SiO_2 NPs were synthesized via well-known Stöber method [16]. Briefly, 2.5 mL TEOS was added to 50 mL absolute ethanol and then, 600 µL NH_4OH was added to the mixture. The solution was stirred at 60 °C for overnight. The resultant milky solution was centrifuged at 6500 rpm for 10 min to recovery the silica nanoparticles. The nanoparticles were repeatedly washed with ethanol. Lastly, the nanoparticles were dried in a vacuum oven.

2.2. Preparation of MPS@SiO_2 NPs

100 mg SiO_2 NPs were dispersed in 25 mL toluene via ultrasonication for 10 min at room temperature. 500 µL of MPS was added to the mixture and the mixture was stirred 18 h at room temperature. MPS modified silica nanoparticles were collected by centrifugation at 6500 rpm for 10 min and washed with plenty of toluene, toluene:methanol and methanol, respectively. Lastly, the nanoparticles were dried in a vacuum oven.

2.3. Preparation of MIP/NIP@SiO_2 NPs

MIP@SiO_2 NPs were prepared via surface initiated free radical polymerization. Atenolol (0.4 mmol) and HEMA (1.6 mmol) were added to 10 mL acetonitrile. The mixture was stirred at room temperature for 4 h to form pre-polymerization mixture. 8.0 mmol EGDMA and 0.015 mmol AIBN were added to the solution. Subsequently, 100 mg MPS@SiO_2 was dispersed in the mixture and polymerization was carried out at 60 °C for 8 h after degassing the mixture with nitrogen for 15 min on an ice-bath. After polymerization, the mixture was diluted by 10 mL ACN and the mixture was centrifuged. The imprinted atenolol was removed from the nanoparticles by washing with methoanol:acetic acid (7/3, v/v) in a Soxhlet extractor. Same protocol was applied to prepare NIP@SiO_2 particles except in the absence of atenolol.

2.4. Rebinding experiments

1.5 mg of MIP/NIP@ SiO_2 NPs dispersed in acetonitrile solution of atenolol at concentration range between 0.1 mg/mL-1.0 mg/mL. The mixture was stirred on an orbital shaker for different time intervals (1-45 min). After rebinding, the nanoparticles were collected by centrifugation. The supernatant was filtered through cellulose acetate membrane and the remaining concentration of atenolol was determined by spectrofluorimetry ($\lambda_{excitation}$: 274 nm, $\lambda_{emission}$: 300 nm). The adsorption capacities of nanoparticles were calculated according to the formula $Q = (C_0 - C_s).\ V / m$ where C_0 *and* C_s are atenolol concentration before and after rebinding, respectively, V is the volume of the solution, and m is the mass of the nanoparticles.

2.5. Selectivity test

In order to test the selectivity of MIP@SiO_2 NPs, propranolol and pindolol were selected as structural analogues. 1.5 mg MIP@SiO_2 was separately dispersed in 0.6 mg/mL concentrations of atenolol, propranolol and pindolol solutions in acetonitrile. The mixtures were stirred on an orbital shaker for 15 min at room temperature and the concentration was determined by spectrofluorimetry.

2.6. Determination of atenolol in spiked artificial urine samples

Artificial urine sample was prepared according to published procedure [17] and pH of the artificial urine sample was adjusted to pH 5. 10 mL of artificial urine sample was spiked with different concentration (0.2 µg/mL-2.5 µg/mL) of standard stock solution of atenolol in acetonitrile. Then, 15 mg MIP@SiO_2 NPs were added to the artificial urine sample and the mixture was stirred for 15 min at room temperature. The nanoparticles were removed from solution by centrifugation and washed with plenty of water. Then, the nanoparticles was washed with methanol:acetic acid (7/3, v/v) to remove the rebound atenolol and concentration of atenolol in the supernatant was determined by spectrofluorimetry.

2. Instruments

The attenuated total reflectance- Fourier transform infrared (ATR-FTIR) analysis was carried out by a Thermo Nicolet 6700 spectrometer and the spectra were collected at a resolution 4 cm-1 after 256 scans. The surface morphology and nanoparticle diameter were determined by transmission electron microscopy (TEM, JEOL JEM 1400). A spectrofluorometer (Shimadzu RF-6000) was used for rebinding experiments.

3. Results and discussion

3.1. Fabrication of MIP@SiO_2 NPs

The synthesis procedure of MIP@SiO_2 NPs is schematically shown in Figure 1. Firstly, SiO_2 NPs were prepared by Stöber method and then, modified with MPS to initiate polymerization on the silica particles. The atenolol-imprinted particles were fabricated through surface-initiated free radical polymerization in the presence of HEMA, atenolol, EGDMA, AIBN and ACN. After polymerization, the imprinted atenolol was removed from the polymer network by methanol:acetic acid mixture and the resultant polymer network on the SiO_2 NPs consists specific cavities that complementary to the atenolol in terms of size, shape and functionality.

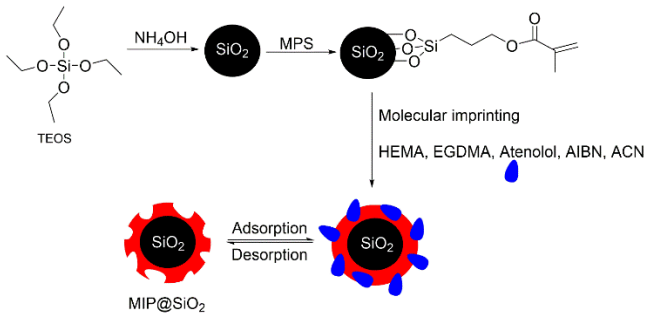

TEOS: tetraethyl orthosilicate

MPS: 3- methacryloxypropyl trimethoxysilane

HEMA: 2-hydroxyethly methacrylate

EGDMA: Ethylene glycol dimethacrylate

AIBN: Azobisisobutyronitrile

ACN: Acetonitrile

Figure 1. *Schematic illustration for preparation of MIP@SiO_2 NPs.*

3.2. Characterization of MIP@SiO_2 NPs

The chemical characterization of silica particles before and after modification were carried out by ATR-FTIR spectroscopy. For bare silica particles (Figure 2a), the band at 1071 cm^{-1} could be assigned as Si-O-Si stretching vibrations of tetrahedral silica structures. After covalent attachment of MPS onto silica particles, a new peak recorded at 1709 cm^{-1} which could be attributed to the carbonyl group of MPS indicating the covalent binding of MPS. The ATR-FTIR spectrum of *MIP@SiO_2 NPs* (Figure 2c), the band at 1716cm^{-1} associated with carbonyl groups of HEMA and the absorption bands at around 3426 cm^{-1} and 2956-2882 cm^{-1} could be assigned as hydroxyl groups and methyl/methylene groups of HEMA indicating the successful grafting of polymer on the silica particles [18, 19].

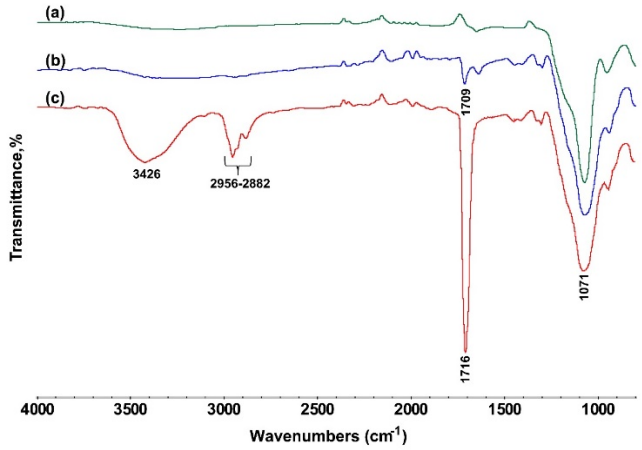

Figure 2. *ATR-FTIR spectra of (a) bare SiO_2, (b) MPS@ SiO_2 and (c) MIP@SiO_2 NPs.*

The size and morphology of MIP@SiO_2 NPs were determined by TEM. As shown in low magnification TEM image of MIP@SiO_2 NPs (Figure 3a), the particles have spherical morphology and no agglomeration occurred after polymerization. Moreover, the particles consist SiO_2 core with a diameter of 93 nm and a homogenous polymer layer with a relatively bright layer and thickness of 21 nm (Figure 3b).

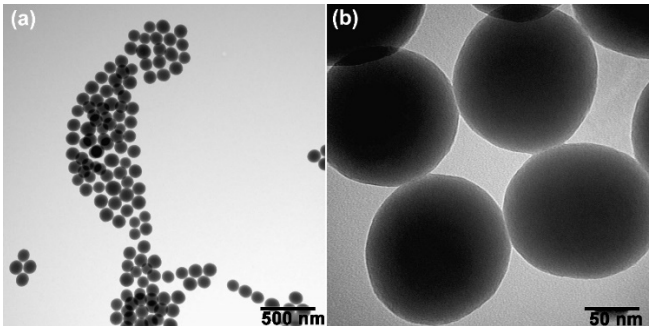

Figure 3. *TEM images of MIP@SiO_2 NPs with low (a) and high (b) magnifications.*

3.3. Rebinding properties of atenolol on MIP/NIP@SiO_2 NPs

The adsorption kinetics for atenolol MIP/NIP@SiO_2 NPs are shown in Figure 4a. The adsorption capacities of both particles increased with increasing adsorption time and reached an equilibration at 15 min adsorption time. Moreover, the adsorption capacity of MIP@SiO_2 NPs was higher than NIP@SiO_2 NPs for all adsorption times implying the

presence of specific recognition cavities on the imprinted particles. Meanwhile, the lower adsorption capacities of NIP@SiO_2 NPs could be mainly occurred non-specific interactions between atenolol and polymer network [19].

The binding isotherms of MIP/NIP@SiO_2 NPs are given in Figure 4b. It is obviously seen that the adsorption capacity of MIP/NIP@SiO_2 NPs towards atenolol increased with increasing initial concentration of atenolol and reached saturation when the initial concentration was 0.6 mg/mL. The adsorption capacity of MIP@SiO_2 NPs was 32.06 mg/g, 4.14 times higher than that of NIP@SiO_2 NPs which is a natural result of the presence of specific binding sites on MIP@SiO_2 NPs.

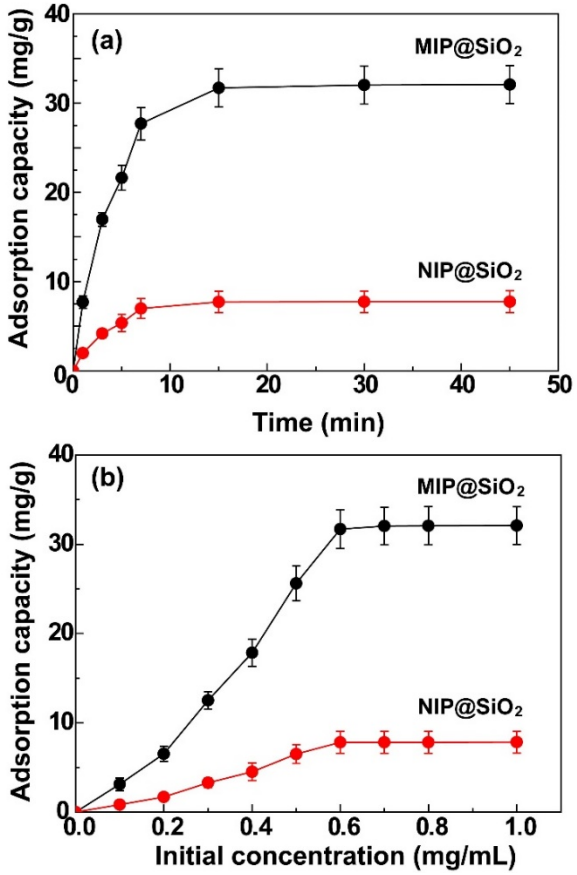

Figure 4. *(a) Adsorption kinetics for MIP/NIP@SiO_2 NPs and (b) Adsorption isotherms for MIP/NIP@SiO_2 NPs.*

Selectivity is a key parameter for any molecularly-imprinted polymers and directly affect the usability of the imprinted polymers for practical applications. The selectivity of the MIP@SiO_2 NPs was tested with propranolol and pindolol as structural analogues of atenolol (Figure 5a). As seen in Figure 5b, the adsorption capacity of MIP@SiO_2 NPs for atenolol is much higher than the other molecules which strongly indicates the presence of selective cavities for atenolol on MIP@SiO_2. Meanwhile, the adsorption capacities of NIP@SiO_2 NPs are nearly same for all analogues implying the non-selective binding is predominant on the NIP@SiO_2 NPs.

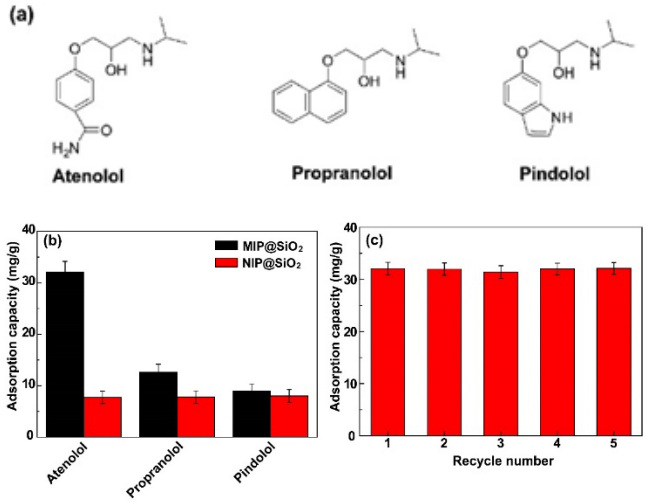

Figure 5. *(a) Molecular structures of atenolol, propranolol and pindolol, (b) Selectivity of MIP/NIP@SiO_2 NPs and (c) Reusability of MIP@SiO_2 NPs*

The imprinting factor ($\alpha = Q_{MIP}/ Q_{NIP}$ where Q_{MIP} and Q_{NIP} are the adsorption capacity of the imprinted and non-imprinted particles, respectively [20]) and relative selectivity coefficient ($\beta = \alpha_{atenolol}/ \alpha_{analogue}$ where $\alpha_{atenolol}$ and $\alpha_{analogue}$ are the imprinting factor of atenolol and its analogues, respectively [21]) were also calculated to obtain more detail information of selectivity (Table 1). The results indicated that the imprinting factor for atenolol is larger than that of the others and the relative selectivity coefficient values are greater than 1 for MIP@SiO_2 NPs which is again the strongest indication that atenolol selectively binds due to the imprinting effect.

Table 1. *The selectivity parameters of MIP/NIP@SiO_2.*

Molecule	***α***	***β***
Atenolol	4.14	-
Propranolol	1.63	2.54
Pindolol	1.12	3.70

Regeneration ability is another important parameter for any imprinted polymer. The reusability of the atenolol-imprinted particles was investigated via adsorption-desorption cycles and the results are given in Figure 5c. The adsorption capacity of MIP@SiO_2 NPs is almost unchanged even after 5 adsorption-desorption cycles. As a result, the high selectivity and stability of the MIP@SiO_2 NPs indicate that it can be used in practical application such as separation and purification technologies.

3.4. Determination of atenolol in spiked artificial urine samples

The artificial urine samples were spiked by atenolol with different atenolol concentration. Then atenolol was extracted with MIP@SiO_2 and coupled with spectrofluorimetry. A good linearity was observed between 0.25-2.5 µg/mL atenolol concentrations. Limit of detection (LOD) and limit of quantification (LOQ) were calculated to be 0.068 µg/mL and 0.228 µg/mL, respectively. Moreover, the recoveries of atenolol varied between 98.6% and 100.1% for different spiked concentrations of atenolol with low standard deviations (less than 4.4%) (Table 2) which indicated that the proposed method is accurate and practical.

Table 2. *Recovery of atenolol from spiked artificial urine samples extract by MIP@SiO_2 NPs. (n=3).*

Added atenolol concentration (µg/mL)	Found atenolol concentration (µg/mL)	Recovery, %	Relative standard deviation,%
0	-	-	-
0.07	0.069 ± 0.003	98.6	4.34
0.28	0.277 ± 0.01	98.9	3.61
0.56	0.559 ± 0.02	99.8	3.57
1.12	1.121 ± 0.04	100.1	3.56

4. Conclusion

In summary, a novel atenolol-imprinted silica nanoparticles were synthesized via surface imprinting approach based on surface initiated free radical polymerization. The prepared imprinted nanoparticles showed high adsorption capacity, fast adsorption kinetic, high selectivity and stability. Moreover, the application of the imprinted nanoparticles was successfully carried out in selective extraction and determination of atenolol from artificial urine samples with high recovery and low standard deviation. The proposed method can be alternative candidate for determination of atenolol in biological samples.

Acknowledgements
The author would like to thank Prof. Dr. Zekiye SULUDERE for TEM analysis.

References

[1]. Odabaşı M., Uzun L., Baydemir G., Aksoy N.H., Acet Ö., Erdönmez D., "Cholesterol imprinted composite membranes for selective cholesterol recognition from intestinal mimicking solution", Colloids and Surfaces B: Biointerfaces, 163, (2018), 266-274.

[2]. Turan E., Şahin F., "Molecularly imprinted biocompatible magnetic nanoparticles for specific recognition of Ochratoxin A", Sensors and Actuators B: Chemical, 227, (2016), 668-676.

[3]. Ansell R.J., Kriz D., Mosbach K., "Molecularly imprinted polymers for bioanalysis: chromatography, binding assays and biomimetic sensors", Current Opinion in Biotechnology, 7, (1996), 89-94.

[4]. Dechtrirat D., Yarman A., Peng L., Lettau K., Wollenberger U., Mosbach K., Scheller F.W., 2 - Catalytically Active MIP Architectures, in: S. Li, S. Cao, S.A. Piletsky, A.P.F. Turner (Eds.) Molecularly Imprinted Catalysts, Elsevier, Amsterdam, 2016, pp. 19-34.

[5]. Mo G., Qin D., Jiang X., Zheng X., Mo W., Deng B., "A sensitive electrochemiluminescence biosensor based on metal-organic framework and imprinted polymer for squamous cell carcinoma antigen detection", Sensors and Actuators B: Chemical, 310, (2020), 127852.

[6]. Regal P., Díaz-Bao M., Barreiro R., Cepeda A., Fente C., "Application of molecularly imprinted polymers in food analysis: clean-up and chromatographic improvements", Open Chemistry, 10, (2012), 766-784.

[7]. Cormack P.A.G., Elorza A.Z., "Molecularly imprinted polymers: synthesis and characterisation", Journal of Chromatography B, 804, (2004), 173-182.

[8]. Gupta P., Goyal R.N., "Amino Functionalized Graphene Oxide and Polymer Nanocomposite Based Electrochemical Platform for Sensitive Assay of Anti-Doping Drug Atenolol in Biological Fluids", Journal of The Electrochemical Society, 163, (2016), B601-B608.

[9]. Hasanah A.N., Dwi Utari T.N., Pratiwi R., "Synthesis of Atenolol-Imprinted Polymers with Methyl Methacrylate as Functional Monomer in Propanol Using Bulk and Precipitation Polymerization Method", Journal of Analytical Methods in Chemistry, 2019, (2019), 9853620.

[10]. Kannappan V., Mannemala S.S., "Simultaneous enantioseparation and purity determination of chiral

switches of amlodipine and atenolol by liquid chromatography", Journal of Pharmaceutical and Biomedical Analysis, 120, (2016), 221-227.

[11]. Shah J.V., Patel D.P., Shah P.A., Sanyal M., Shrivastav P.S., "Simultaneous quantification of atenolol and chlorthalidone in human plasma by ultra-performance liquid chromatography–tandem mass spectrometry", Biomedical Chromatography, 30, (2016), 208-216.

[12]. Yilmaz B., Arslan S., "Determination of Atenolol in Human Urine by Gas Chromatography-Mass Spectrometry Method", Journal of Chromatographic Science, 49, (2011), 365-369.

[13]. Arvand M., Vejdani M., Moghimi M., "Construction and performance characterization of an ion selective electrode for potentiometric determination of atenolol in pharmaceutical preparations", Desalination, 225, (2008), 176-184.

[14]. Damiani P.C., "Determination of atenolol in human urine by emission–excitation fluorescence matrices and unfolded partial least-squares with residual bilinearization", Talanta, 85, (2011), 1526-1534.

[15]. Sapir A., Shalev A.H., Skalka N., Bronshtein A., Altstein M., "Development of an enzyme-linked immunosorbent assay and a beta-1 adrenergic receptor–based assay for monitoring the drug atenolol", Environmental Toxicology and Chemistry, 32, (2013), 585-593.

[16]. Mellon V., Rinaldi D., Bourgeat-Lami E., D'Agosto F., "Block Copolymers of γ-Methacryloxypropyltrimethoxysilane and Methyl Methacrylate by RAFT Polymerization. A New Class of Polymeric Precursors for the Sol−Gel Process", Macromolecules, 38, (2005), 1591-1598.

[17]. Lopez C., Claude B., Morin P., Pelissou M., Pena R., Max J.-P., Ribet J.-P., "Synthesis and study of a molecularly imprinted polymer for specific solid-phase extraction of vinflunine and its metabolite from biological fluids", Journal of Separation Science, 34, (2011), 1902-1909.

[18]. Zengin A., Tamer U., Caykara T., "A SERS-Based Sandwich Assay for Ultrasensitive and Selective Detection of Alzheimer's Tau Protein", Biomacromolecules, 14, (2013), 3001-3009.

[19]. Bilici M., "Synthesis of a Novel Molecularly Imprinted Polymer for the Sensitive and Selective Determination of Artemisinin in Urine Samples Based on Solid-Phase Extraction (SPE) and Determination with High-Performance Liquid Chromatography (HPLC)", Analytical Letters, (2020), 1-17.

[20]. Gorbani Y., Yılmaz H., Basan H., "Spectrofluorimetric determination of atenolol from human urine using high-affinity molecularly imprinted solid-phase extraction sorbent", Luminescence, 32, (2017), 1391-1397.

[21]. Zengin A., Badak M.U., Aktas N., "Selective separation and determination of quercetin from red wine by molecularly imprinted nanoparticles coupled with HPLC and ultraviolet detection", Journal of Separation Science, 41, (2018), 3459-3466..

MANAS Journal of Engineering
ISSN 1694-7398 | e-ISSN 1694-7398

Volume 9, Special Issue 1, (2021) Pages 49-57
https://doi.org/10.51354/mjen.878066

Asymptotic behaviours of the solutions of neutral type Volterra integro-differential equations and some numerical solutions via differential transform method

Yener Altun

Yuzuncu Yil University, Ercis Management Faculty, Department of Business Administration, Van, Turkey, yeneraltun@yyu.edu.tr, ORCID: 0000-0003-1073-5513

ABSTRACT

In this manuscript, we consider the first order neutral Volterra integro-differential equation (NVIDE) with delay argument. Firstly, we obtain novel sufficient conditions to establish the asymptotic behaviours of solutions of considered NVIDE using the Lyapunov method and present an example to demonstrate the applicability of proposed method. Secondly, we get some numerical solutions for a particular case of considered NVIDE via the differential transformation method (DTM). The results of this manuscript are novel and they improve some existing ones in the literature.

ARTICLE INFO

Research article

Received: 10.02.2021
Accepted: 25.03.2021

Keywords:
Asymptotic behavior,
Lyapunov functional,
NVIDE,
DTM

1. Introduction

Volterra integral and integro-differential equations were first introduced by Vito Volterra in 1926. Subsequently, these equations have been frequently used in technical fields of scientific and engineering. Volterra integro-differential equations (VIDEs), which are known as a famous mathematical model in the related literature, and delay differential equations/systems have been seen in many practical fields such as electrical circuit, glass forming process, biology, physics, chemistry, control theory, economics (see, [1-13]). Besides, many researchers have done studies on the qualitative behaviors of solutions and some numerical solutions of these equations in recent years. Lyapunov's direct method is an important tool to discuss the some qualitative behaviors of solutions of ordinary and functional differential equations and integro-differential equations. This technique is theoretically very attractive, and there are many applications where it is natural to use it. However, it is rather difficult to construct a meaningful Lyapunov functional for a non-linear ordinary or functional differential equation and a non-linear functional VIDE.

DTM, which is a semi-analytical-numerical method, is based on the expansion of the Taylor series. The method principle was first used by Pukhov [14] who applied to solve linear and non-linear physical process problems, and by Zhou[15] who applied to linear and non-linear initial value problems in electrical circuit analysis. In obtaining numerical, analytical and precise solutions of ordinary and partial differential equations, this approach is beneficial and has been widely studied and applied in recent years (see, [16-20]). DTM is a reliable approach that needs less effort and does not need linearization, according to existing methods in the literature. By using this method, it is possible to solve integral and integro-differential equations [21], differential difference equations [22], partial differential equations [23], fractional-order differential equations [24].

In this manuscript, we consider the first order NVIDE with delay argument:

$$\frac{d}{dt}[u(t)+c(t)u(t-\xi(t))] = -a(t)\mu(u) - b(t)u(t-\xi(t)) + \int_{t-\xi(t)}^{t} k(t,s)\, f(u(s))ds + h(t,u(t),u(t-\xi(t))), \quad t \geq 0, \tag{1}$$

where $a(t),\ b(t), c(t):[t_0,\infty)\to[0,\infty),\ t_0\geq 0,$ are continuous and $c(t)$ is differentiable with $|c(t)|\leq c_0<1\ \ (c_0-\text{constant});\ h,\ k$ and f with $f(0)=0,$ are real-valued and continuous functions on their respective domains. The varying delay argument $\xi(t):[0,\infty)\to[0,\xi_0]$ is continuous and differentiable and satisfying

$$0\leq\xi(t)\leq\xi_0,\quad 0\leq\xi'(t)\leq\delta<1, \tag{2}$$

where ξ_0 and δ are positive constants.

For each solution $u(t)$ of equation (1), we assume the following existence initial condition:

$$u(\theta)=\varphi(\theta),\qquad \theta\in[t_0-\xi_0,t_0],$$

where $\varphi\in C([t_0-\xi_0,\ t_0],\ \Re).$

Define

$$\mu_0(u)=\begin{cases}\mu(u)u^{-1}, & u\neq 0\\ \dfrac{d\mu(0)}{dt}, & u=0.\end{cases} \tag{3}$$

Hence, from (1) and (3), we have

$$\frac{d}{dt}[u(t)+c(t)u(t-\xi(t))]=-a(t)\mu_0(u)u(t)-b(t)u(t-\xi(t))+\int_{t-\xi(t)}^{t}k(t,s)f(u(s))ds$$
$$+h(t,u(t),u(t-\xi(t))),\qquad t\geq 0. \tag{4}$$

2. Main problem

In this section**,** before proceeding further, we will state some assumptions for main result.

2.1. Assumptions

(A1) There exists a positive constant $\beta,$ such that

$$|k(t,s)|\leq\beta,\ \text{for all}\ t\geq 0\ .$$

(A2) There is an $M>0,$ such that $|u|,|z|\leq M$ imply that,

$$|f(u)-f(z)|\leq|u-z|\quad\text{and}\quad f(0)=0.$$

(A3) Let $h(t,u,u(t-\xi(t)))\in\Re$ be a non-linear uncertainty such that

$$\left|h(t,u,u(t-\xi(t))\right| \le q_1\left|u(t)\right| + q_2\left|u(t-\xi(t))\right|, \quad q_1, q_2 \ge 0 .$$

(A4) $\tilde{\mu}$ be a positive constant such that $1 \le \mu_0(u) \le \tilde{\mu}$ for all $u \in \Re$.

Theorem 1: Assumptions (A1)–(A4) are satisfied. Then, the zero solution of NVIDE (4) is asymptotically stable, if there exists a constant c_0 such that $\left|c(t)\right| \le c_0 < 1$ and

$$\Lambda = \left(\Lambda_{jk}\right) < 0, \tag{5}$$

where Λ is a 3×3 symmetric matrix with the elements $\Lambda_{11} = -2a(t) + q_1\left(c_0 + 2\right) + (\beta + 1)\xi_0 + q_2 + 1,$
$\Lambda_{12} = -\left(c_0 a(t) + b(t)\right), \Lambda_{13} = 0, \Lambda_{22} = q_2 - (1-\delta) + c_0\left(-2b(t) + \beta\xi_0 + q_1 + 2q_2\right), \Lambda_{23} = 0, \Lambda_{33} = \beta + \beta c_0 - (1-\delta).$

Proof. Consider the legitimate Lyapunov functional as

$$W(t) = [u(t) + c(t)u(t-\xi(t))]^2 + \int_{t-\xi(t)}^{t} u^2(s)ds + \int_{t-\xi(t)}^{t}\int_{s}^{t} f^2(u(v))dvds.$$

From the calculation of the time derivative of the Lyapunov functional W, we have

$$\begin{aligned}
\frac{dW}{dt} &= 2[u(t) + c(t)u(t-\xi(t))][-a(t)\mu_0(u)u(t) - b(t)u(t-\xi(t)) \\
&\quad + \int_{t-\xi(t)}^{t} k(t,s) f(u(s))ds + h(t,u(t),u(t-\xi(t))] + u^2(t) \\
&\quad -(1-\xi'(t))u^2(t-\xi(t)) + \int_{t-\xi(t)}^{t} f^2(u(t))ds - (1-\xi'(t))\int_{t-\xi(t)}^{t} f^2(u(v))dv \\
&= -2a(t)\mu_0(u)u^2(t) - 2b(t)u(t)u(t-\xi(t)) + 2u(t)\int_{t-\xi(t)}^{t} k(t,s) f(u(s))ds \\
&\quad +2u(t)h(t,u(t),u(t-\xi(t)) - 2a(t)c(t)\mu_0(u)u(t)u(t-\xi(t)) \\
&\quad -2b(t)c(t)u^2(t-\xi(t)) + 2c(t)u(t-\xi(t))\int_{t-\xi(t)}^{t} k(t,s) f(u(s))ds \\
&\quad +2c(t)u(t-\xi(t))h(t,u(t),u(t-\xi(t)) + u^2(t) - (1-\xi'(t))u^2(t-\xi(t)) \\
&\quad +\xi(t) f^2(u(t)) - (1-\xi'(t))\int_{t-\xi(t)}^{t} f^2(u(v))dv \\
&\le -2a(t)u^2(t) - 2b(t)u(t)u(t-\xi(t)) + 2\beta\left|u(t)\right|\int_{t-\xi(t)}^{t}\left|f(u(s))\right|ds \\
&\quad +2q_1u^2(t) + 2q_2\left|u(t)\right|\left|u(t-\xi(t))\right| - 2a(t)c(t)u(t)u(t-\xi(t))
\end{aligned}$$

$$
\begin{aligned}
&-2b(t)c(t)u^2(t-\xi(t))+2\beta c(t)\left|u(t-\xi(t))\right|\int_{t-\xi(t)}^{t}\left|f(u(s))\right|ds\\
&+2q_1c(t)\left|u(t)\right|\left|u(t-\xi(t))\right|+2q_2c(t)u^2(t-\xi(t))+u^2(t)\\
&-(1-\xi'(t))u^2(t-\xi(t))+\xi(t)f^2(u(t))-(1-\xi'(t))\int_{t-\xi(t)}^{t}f^2(u(v))dv\\
&\le\left(-2a(t)+2q_1+1\right)u^2(t)-2\left(c_0a(t)+b(t)\right)u(t)u(t-\xi(t))\\
&+\beta\int_{t-\xi(t)}^{t}\left(u^2(t)+f^2(u(s))\right)ds+q_2\left(u^2(t)+u^2(t-\xi(t))\right)\\
&+\left(2q_2c_0-2c_0b(t)-(1-\xi'(t))\right)u^2(t-\xi(t))\\
&+\beta c_0\int_{t-\xi(t)}^{t}\left(u^2(t-\xi(t))+f^2(u(s))\right)ds+q_1c_0\left(u^2(t)+u^2(t-\xi(t))\right)\\
&+\xi(t)f^2(u(t))-(1-\xi'(t))\int_{t-\xi(t)}^{t}f^2(u(v))dv.
\end{aligned}
$$

From (2), we obtain

$$
\begin{aligned}
\frac{dW}{dt}&\le\left(-2a(t)+q_1\left(c_0+2\right)+(\beta+1)\xi_0+q_2+1\right)u^2(t)\\
&-2\left(c_0a(t)+b(t)\right)u(t)u(t-\xi(t))\\
&+\left(q_2+c_0\left(-2b(t)+\beta\xi_0+q_1+2q_2\right)-(1-\delta)\right)u^2(t-\xi(t))\\
&+[\beta+\beta c_0-(1-\delta)]\int_{t-\xi(t)}^{t}f^2(u(s))ds.
\end{aligned}
$$

The last estimate implies that

$$\frac{dW}{dt}\le\psi^T(t)\Lambda\Psi(t),$$

where $\psi^T(t)=[u(t)\quad u(t-\xi(t)\quad(\int_{t-\xi(t)}^{t}f^2(u(s))ds)^{1/2}]$ and Λ is defined in (5). Therefore if the matrix Λ is negative definite, $\frac{dW}{dt}$ is negative. (5) implied that there exists a constant sufficiently small $\eta>0$ such that $\frac{dW}{dt}\le-\eta\left\|u_t\right\|$. Thus, equation (4) is asymptotically stable according to [6, Theorem 8.1, pp. 292–293]. This completes the proof of Theorem 1.

Example 1: As a special case of the equation (4), we consider the following the first order NVIDE

$$\frac{d}{dt}[u(t)+0.24u(t-0.3)]=-1.8u(t)-0.5u(t-0.3)-0.6\int_{t-0.3}^{t}u(s)ds,\quad t\geq 0. \tag{6}$$

Here

$$a(t)=1.8, b(t)=0.5, c(t)=0.24, |k(t,s)|\leq \beta=0.6, q_1=q_2=0, \xi(t)=0.3\ . \tag{7}$$

Under the above assumptions, by solving (5) using Matlab, it can be easily determined that all eigenvalues of this matrix are negative. As a result, it is clear that all the conditions of Theorem 1 hold. This discussion implies that the zero solution of equation (6) with (7) is asymptotically stable.

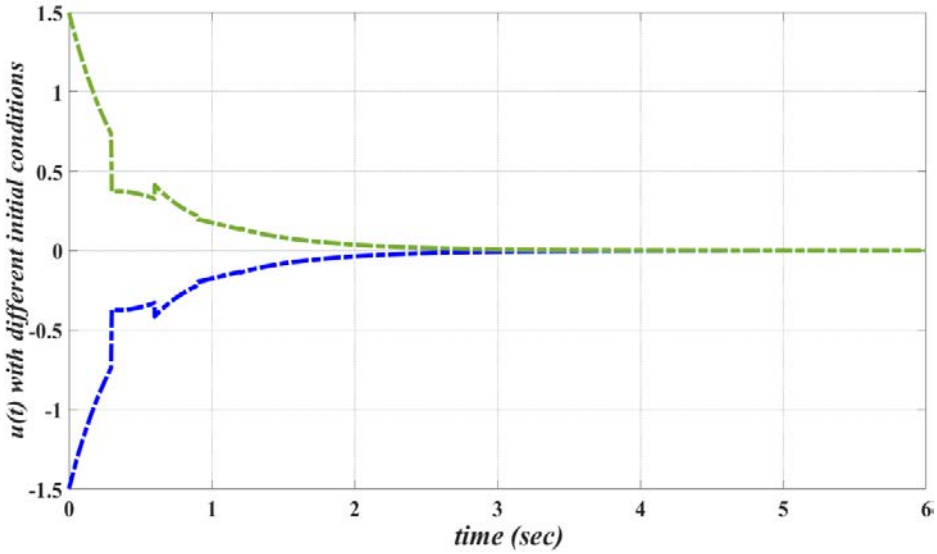

Figure 1 *The simulation of the Example 1.*

3. DTM and numerical experiment

The theory of differential transformation can be found in [14]-[15]. In this manuscript we will explain briefly. The differential transformation of function $u(t)$ is defined as

$$U(k)=\frac{1}{k!}\left[\frac{d^k u(t)}{dt^k}\right]_{t=0}, \tag{8}$$

where $u(t)$ is the original function and $U(k)$ is the transformed function.

Differential inverse transformation of $U(k)$ is defined as

$$u(t)=\sum_{k=0}^{\infty}\frac{t^k}{k!}\left[\frac{d^k u(t)}{dt^k}\right]_{t=0}. \tag{9}$$

From (8) and (9), if the function $u(t)$ can be expressed in a finite series as follows

$$u(t)=\sum_{k=0}^{\infty}U(k)t^k=U(0)+U(1)t+U(2)t^2+\ldots, \tag{10}$$

then it is called series solution of the DTM.
The following fundamental theorems can be easily deduced from equations (8) and (9) (also, see [20], [21]).

Theorem 2: If $u(t)=\dfrac{du(t)}{dt}$, then $U(k)=\dfrac{(k+1)!}{k!}U(k+1)=(k+1)U(k+1)$.

Theorem 3: If $u(t)=\delta u(t)$, then $U(k)=\delta U(k)$, where δ is a constant.

Theorem 4: If $u(t)=u(t-a)$, $a>0$ and reel constant, then

$$U(k)=\sum_{i=k}^{N}(-1)^{i-k}\binom{i}{k}a^{i-k}U(i),\ N\to\infty.$$

Theorem 5: If $u(t)=\dfrac{d}{dt}u(t-a)$, then

$$U(k)=(k+1)\sum_{i=k+1}^{N}(-1)^{i-k-1}\binom{i}{k+1}a^{i-k-1}U(i),\ N\to\infty.$$

Theorem 6: If $u(t)=\int_{t_0}^{t}u(s)ds$, then $U(k)=\dfrac{U(k-1)}{k}$, $k\geq 1$.

Now, we demonstrate potentiality, advantages and effectiveness of our method on an example.

Example 2:

$$\frac{d}{dt}[u(t)+0.25u(t-0.2)]=-2u(t)-0.2u(t-0.4)-0.3\int_{t-0.3}^{t}u(s)ds,\quad t\geq 0, \tag{11}$$

$$u(0)=2.5\ . \tag{12}$$

As a special case of the equation (4), under initial condition $u(0)=2.5$, we consider the first order NVIDE (11) with delay argument. Taking into account Theorems 2-6, applying DTM on both sides of equation (11) and condition (12), we obtain the following recurrence relation

$$U(0)=2.5,$$

$$(k+1)U(k+1)=[-0.25(k+1)\sum_{i=k+1}^{N}(-1)^{i-k-1}\binom{i}{k+1}0.2^{i-k-1}U(i)-2U(k)$$

$$-0.2\sum_{i=k}^{N}(-1)^{i-k}\binom{i}{k}(0.4)^{i-k}U(i)-0.3\frac{U(k-1)}{k}],\qquad k=0,\ 1,\ 2.$$

Using this recurrence relation, the following series coefficients $U(k)$ can be obtained.

For $N = 4$,

$$U(1) = -4.393919443,\quad U(2) = 4.302113487,\quad U(3) = -3.45438152,\quad k = 0,\ 1,\ 2.$$

For $N = 6$,

$$U(1) = -4.391032965,\quad U(2) = 4.310228598,\quad U(3) = -3.580749520,\quad k = 0,\ 1,\ 2.$$

For $N = 8$,

$$U(1) = -4.395762327,\quad U(2) = 4.300262145,\quad U(3) = -3.364722005,\quad k = 0,\ 1,\ 2.$$

Finally, using above mentioned relations, taking $N = 4,\ 6,\ 8$ and using formula (10), we reach approximate solutions of the NVIDE (11) with three iterations as follows:

$N = 4$,

$$u_{DTM}(t) = 2.5 - 4.393919443t + 4.302113487t^2 - 3.45438152t^3,$$

$N = 6$,

$$u_{DTM}(t) = 2.5 - 4.391032965t + 4.310228598t^2 - 3.580749520t^3,$$

$N = 8$,

$$u_{DTM}(t) = 2.5 - 4.395762327t + 4.300262145t^2 - 3.364722005t^3.$$

As a result, it is seen that in the cases of $N = 4$, $N = 6$ and $N = 8$, our numerical results are almost the same.

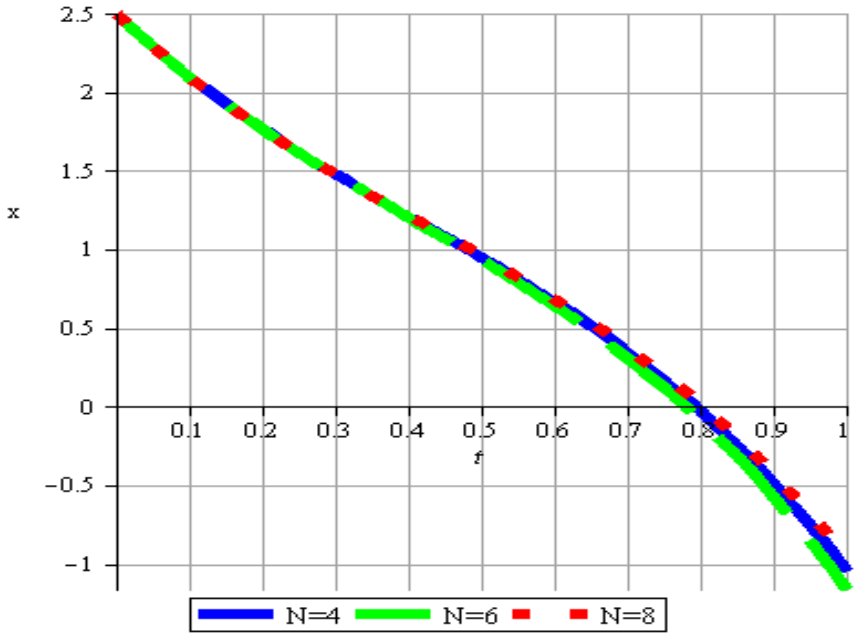

Figure 2 *Comparison between approximate solutions with DTM for* N *and* $0 \le t \le 1$.

Table 1 *Comparison of numerical results with DTM obtained.*

t	*N*=4	*N*=6	*N*=8
0.0	2.5	2.5	2.5
0.1	2.100174808	2.100418240	2.100061666
0.2	1.765665585	1.765556555	1.765940245
0.3	1.475746036	1.473930447	1.477447401
0.4	1.209689859	1.204055421	1.214394804
0.5	0.9467707560	0.9344469780	0.9565941214
0.6	0.6662624282	0.6436206197	0.6838570229
0.7	0.347438578	0.310091852	0.375995174
0.8	-0.030427096	-0.087623823	0.012820244
0.9	-0.488060893	-0.571010904	-0.425856099
1.0	-1.046189108	-1.161553887	-0.960222187

5. Conclusion

In this manuscript, we first derived some novel sufficient conditions to prove the asymptotic behaviours of solutions of the first order NVIDE with delay argument. We provided an example to show the effectiveness of proposed method by Matlab. Thereafter, for a special case of considered NVIDE using DTM, we obtained some numerical approximations as for different N ve t by a suitable computer program. We constructed the Table 1 to make a comparison between the numerical results for $N=4$, $N=6$ and $N=8$. Finally, the simulations (Figure 1 and Figure 2) in Example 1 and Example 2 show that the proposed methods are useful and feasible in terms of the obtained results.

References

[1]. Agarwal, R. P., Grace, S. R., “Asymptotic stability of certain neutral differential equations”, Math. Comput. Modelling, 31(8-9), (2000), 9–15.

[2]. Altun, Y., “A new result on the global exponential stability of nonlinear neutral volterra integro-differential equation with variable lags”, Math. Nat. Sci., 5, (2019), 29–43.

[3]. Altun, Y., “Further results on the asymptotic stability of Riemann–Liouville fractional neutral systems with variable delays”, Adv. Difference Equ., 437,(2019), 1-13.

[4]. Altun, Y., “Improved results on the stability analysis of linear neutral systems with delay decay approach”, Math Meth Appl Sci., 43, (2020), 1467–1483.

[5]. Altun, Y., Tunç C., “On the global stability of a neutral differential equation with variable time-lags”, Bull. Math. Anal. Appl., 9(4), (2017), 31-41.

[6]. Hale, J., Verduyn Lunel, S.M., “Introduction to functional-differential equations”, Springer Verlag, (1993), New York.

[7]. Kolmanovskii, V., Myshkis, A., “Applied Theory of Functional Differential Equations”, Kluwer Academic Publisher Group, (1992), Dordrecht.

[8]. Kulenovic, M., Ladas, Meimaridou, A., "Necessary and sufficient conditions for oscillations of neutral differential equations", J. Aust. Math. Soc. Ser. B, 28, (1987), 362-375.

[9]. Park, J. H., Kwon, O. M., "Stability analysis of certain nonlinear differential equation", Chaos Solitons Fractals, 37, (2008), 450-453.

[10]. Raffoul, Y., "Boundedness in nonlinear functional differential equations with applications to Volterra integro differential equations", J. Integral Equ. Appl., 16(4), (2004), 375–388.

[11]. Rama Mohana Rao, M., Raghavendra, V., "Asymptotic stability properties of Volterra integro-differential equations", Nonlinear Anal., 11(4), (1987), 475–480.

[12]. Tunç, C., Altun, Y., "Asymptotic stability in neutral differential equations with multiple delays", J. Math. Anal., 7(5), (2016), 40–53.

[13]. Vanualailai, J, Nakagiri, S., "Stability of a system of Volterra integro-differential equations", J. Math. Anal. Appl., 281(2), (2003), 602–619.

[14]. Pukhov, G. E., "Differential Transformations and Mathematical Modelling of Physical Processes", Naukova Dumka, (1986), Kiev.

[15]. Zhou, J. K., "Differential Transformation and Its Application for Electrical Circuits", Huazhong University Press, (1986), Wuhan.

[16]. Arslan, D., "Approximate Solutions of Singularly Perturbed Nonlinear Ill-posed and Sixth-order Boussinesq Equations with Hybrid Method", BEU Journal of Science, 8(2), (2019), 451-458.

[17]. Arslan, D., "A Novel Hybrid Method for Singularly Perturbed Delay Differential Equations", Gazi University Journal of Sciences, 32(1), (2019), 217-223.

[18]. Arslan, D., "Numerical Solution of Nonlinear the Foam Drainage Equation via Hybrid Method", New Trends in Mathematical Sciences, 8(1), (2020), 50-57.

[19]. Ayaz, F., "Applications of Differential Transform Method to Differential-Algebraic Equations", Applied Mathematics and Computation, 152, (2004), 649-657.

[20]. Rebenda, J., Smarda, Z., Khan, Y., "A New Semi-analytical Approach for Numerical Solving of Cauchy Problem for Differential Equations with Delay", Filomat, 31(15), (2017), 4725–4733.

[21]. Arikoglu, A., Ozkol, I., "Solutions of integral and integro-differential equation systems by using differential transform method" Comput. Math. Appl., 56, (2008), 2411–2417.

[22]. Zou, L., Wang, Z., Zong, Z., "Generalized differential transform method to differential-difference equation", Phys. Lett. A, 373, (2009), 4142–4151.

[23]. Chen, C. K., Ho, S. H., "Solving partial differential equations by two dimensional differentialtransform", Appl. Math. Comput., 106, (1999), 171–179.

[24]. Arikoglu, A., Ozkol, I., "Solution of fractional differential equations by using differential transform method", Chaos Soliton. Fract., 34, (2007), 1473–1481.

MANAS Journal of Engineering
ISSN 1694-7398 | e-ISSN 1694-7398

Volume 9, Special Issue 1, (2021) Pages 58-64
https://doi.org/10.51354/mjen.884756

Synthesis, spectroscopy, and photophysical properties of newly magnesium (II) phthalocyanine

Mehmet Pişkin*[,1], Ömer Faruk Öztürk[2], Zafer Odabaş[3]

[1] Department of Food Processing, Çanakkale Technical Sciences Vocational School, Çanakkale Onsekiz Mart University, 17020, Çanakkale, Turkey, mehmetpiskin@comu.edu.tr, ORCID: 0000-0002-4572-4905

[2] Çanakkale Onsekiz Mart University, Department of Chemistry, Çanakkale, Turkey, ORCID: 0000-0002-4545-7149

[3] Marmara University, Department of Chemistry, İstanbul, Turkey, ORCID: 0000-0002-0647-0404

ABSTRACT

2(3),9(10),16(17),23(24)-tetrakis-2,6-dimethoxyphenoxy substituted magnesium (II) phthalocyanine, which has very good solubility in polar and non-polar solvents and does not aggregate, was synthesized. Its structure was characterized by spectroscopic methods such as elemental analysis, UV-*vis*, FT-IR, MALDI-TOF mass and ^{1}H NMR. It has very good solubility in polar aprotic solvents such as dimethyl sulfoxide, *N*, *N*- Dimethylformamide, tetrahydrofuran, dichloromethane, and non-polar solvents such as toluene, chloroform. Its aggregation properties have been studied both in the solvents mentioned above and in *N*, *N*- Dimethylformamide at different concentrations. Its photophysical properties were determined in *N*, *N*-dimethyl formamide. The effects of the nature and presence of 2,6-dimethoxyphenoxy group, which is an antioxidant derivative, on the phthalocyanine skeleton on the spectroscopic and photophysical properties were investigated by comparing it with unsubstituted magnesium (II) phthalocyanine. It can be a good nominee for various technological applications in that it does not aggregate and has good solubility in polar and non-polar solvents, as well as better and favorable fluorescence properties than its analog in the previous study.

ARTICLE INFO

Research article

Received: 22.02.2021
Accepted: 25.03.2021

Keywords:
phthalocyanine, magnesium (II), 2,3-dimethoxyphenol, highly solubility, spectroscopic, photophysical

**Corresponding author*

1. Introduction

Phthalocyanines (Pcs) are synthetic substances related to naturally occurring porphyrins [1]. Pcs have been used in numerous technological applications. Pcs are an interesting class of compounds with increasingly diverse industrial and biomedical applications, photosensitization [1], non-linear optics [2], catalysis [3], photodynamic therapy [4], photocatalysis [5], liquid crystals [6], and gas sensing [7], etc. The wide range of Pc applications are primarily because of their high molar absorption coefficient ($\varepsilon > 10^5$) in the far end of the visible spectrum, high triplet state quantum yields, long lifetimes, exceptionally high thermal, chemical and electromagnetic stability [8]. Optical properties of Pcs depend on their solubility and aggregation behavior [9]. Pcs can coordinate with most metals and can be substituted at the periphery with a variety of substituents [10]. In the center of planar π-electron conjugated Pc ring, various metal ions can be coordinated, *e.g.*, Mg^{2+}, Zn^{2+}, Fe^{3+} [11]. In this way, specific physicochemical and biological properties of Pcs can be modified. [12]. The photophysical properties of Pc are strongly influenced by the presence and nature of the coordinated central metal ion [12]. Magnesium phthalocyanine (MgPc) and its derivatives, being synthetic analogs of chlorophyll [1]. These are of great interest because of their chemical, catalytic and spectroscopic properties [13, 14], which appear to be significantly different from other divalent metallophthalocyanines [15]. The electrochemical properties of MgPc derivatives make them good candidates for solar energy conversion in laser printers and optical discs [16-18], as well as pigment materials [19-22]. Pcs are mostly hydrophobic compounds and are insoluble in solvent media [22]. To increase the solubility of Pcs, some functional groups such as crown ether, alkyl, alkoxy, alkylthio and donor atoms such as N and O need to be substituted on the peripheral positions of phthalocyanines [23-25]. MgPcs exhibit an intense absorption band in the near-IR spectral region due to the non-planar nature that arises from the magnesium atom being displaced from the Pc plane. This is because the magnesium ion of a molecule interacts with the N-azomethine atom of the neighboring MgPc molecule [26]. This effect will be observed further for MgPcs due to differences in flatness as noted above [26]. The spectra and photophysical behavior

of MgPcs will therefore depend on their flatness. [26]. In this study, combining 2,3-dimethoxyphenoxy group and phthalocyanine, which are bioactive compounds, in one molecule, and in this complex, the non-aggregated and bifunctional new MgPc, which has high solubility in various solvents, was designed, synthesized and its structure was characterized by widely known spectroscopic techniques (Scheme 1). In addition, the photophysical properties of this complex were studied in *N*, *N*-dimethyl formamide (DMF) and its spectroscopic and photophysical properties were compared with unsubstituted magnesium (II) phthalocyanine [27].

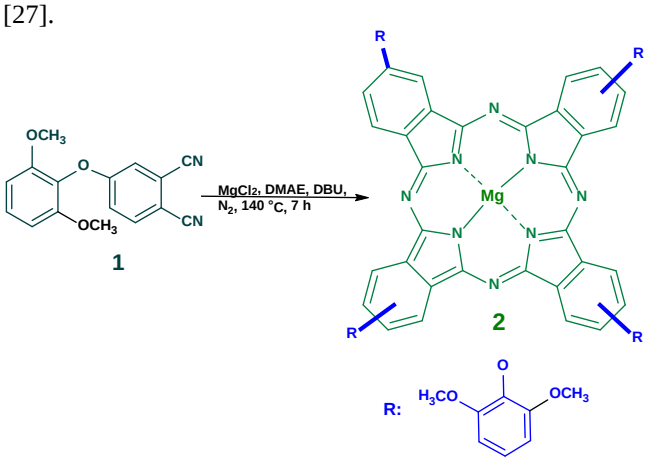

Scheme 1. *Synthesis of peripheral-tetrakis-2,6-dimethoxyphenoxy substituted magnesium (II) phthalocyanine* ***2***

2. Experimental section

The used materials, equipment, photophysical formulas and parameters were supplied as supplementary information.

2.1. Synthesis of 2(3),9(10),16(17),23(24)-tetrakis-(2,6-dimethoxyphenoxy) phthalocyaninato magnesium (II) (MgPc) (2)

4-(2,6-dimethoxyphenoxy) phthalonitrile **1** [28] (0.12 g, 0.43 mmol), anhydrous magnesium(II) chloride (0.04 g, 0.43 mmol) and and catalytic amount of 1,8-diazabicyclo[5.4.0]undec-7-ene (DBU) in 1.50 cm^3 of 2-Dimethylaminoethanol (DMAE) was heated with stirring at 140 °C in a sealed glass tube for 7 hours under nitrogen atmosphere. The resulting suspensions were cooled to room temperature and then poured into 25 ml of ethanol. The precipitates were filtered off and washed with water, hot ethanol, methanol and acetone. The products were purified using column chromatography on silica gel using dichloromethane (DCM): ethanol (MeOH) (85:15) solvent system as eluent. The phthalocyanine complexes were then dried in vacuo over P_2O_5. The MgPc **2** is soluble in dimethylsulfoxide (DMSO), *N,N*-dimethylformamide (DMF), tetrahydrofuran (THF), toluene, chloroform ($CHCl_3$), and dichloromethane (DCM). Mp>300° C. Yield: 37.17 mg (28.54%). Calculated for $C_{64}H_{48}MgN_8O_{12}$ Elemental Analysis: C, 67.11; H, 4.22; N, 9.78; found C, 65.87%; H, 3.79%; N, 9.33%. IR (ATR) λ_{max}/cm^{-1}: 750-1010(C–H str.), 1090-1188(C–N str.), 1230-1330(C–O str.), 1450-1480 (C–H bend.), 1582-1596(C=C str.), 2850-2970 (>CH_2 str.), 3065(=C–H str.). UV–*vis* (DMF, $1x10^{-5}$ M): λ_{max}(nm), (log ε): 362 (4.675 (5.02). MS *(*MALDI-TOF*)* m/z: calc.: 1145.42; found: 1146.75 $[M+H]^+$. ^{1}H NMR [500 MHz, $CDCl_3$, δ (ppm)]: 7.70-7.55(m, Ar-H, 8H), 7.32-7.24(m, Ar-H, 4H), 7.02-6.92(m, Ar-H, 4H), 6.78-6.70(m, Ar-H, 8H), 3.81 (m, O-CH_3, 24H).

3. Results and discussion

3.1. Synthesis and characterization

Precursor molecule 1 for this reaction were synthesized as given in literature [28-32]. The MgPc 2 was synthesized by cyclotetramerization reaction of the 4-(2,6-dimethoxy phenoxy)phthalonitrile 1 presence of DMAE as the solvent, DBU as the catalyzer and anhydrous magnesium(II) chloride under the nitrogen atmosphere (Scheme 1). The MgPc 2 was obtained as bluish green solids, 28.54% in yield. The MgPc 2 was washed several times with hot ethanol, methanol and acetone and then were purified by column chromatography with silica gel using DCM: EtOH (85:15) as an eluent. The MgPc 2 was characterized by FT-IR, ^{1}H NMR, UV–*vis*, MALDI-TOF mass spectroscopic techniques, and elemental analysis as well. The analyses are consistent with the predicted structure as shown in the experimental section. Main findings are found suitable for proposed structure of this phthalocyanine. The proposed target structure of the MgPc 2 was affirmed in the FT-IR spectra by the disappearance of the -C≡N vibration at 2231 cm^{-1} for the phthalonitrile 1 [28-32]. In the FT-IR spectrum of the MgPc 2, stretching vibrations of aromatic CH groups around 3065 cm^{-1}, aliphatic-CH, CH_2 groups around 2970-2850 cm^{-1}, aromatic -C=C groups around 1596 -1582 cm^{-1} and –C-H bands around 1480-1450 cm^{-1} appeared at expected frequencies (Fig.1).

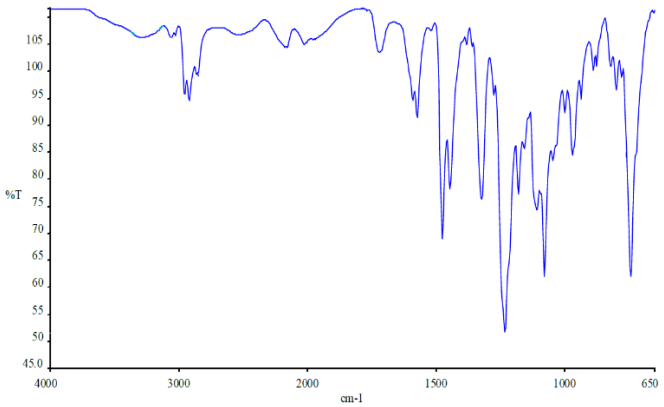

Figure 1. *FT-IR spectrum of the MgPc 2.*

The ^{1}H NMR spectrum of the MgPc 2 was recorded in chloroform-d ($CDCl_3$). ^{1}H-NMR spectrum of the MgPc 2 showed aromatic protons broad peak at 7.70-6.70 ppm. It is probable that the broadening is due to the chemical exchange caused by aggregation–disaggregation equilibrium [33]. In the ^{1}H-NMR spectrum of the MgPc **2**, the multiple peaks for aromatic protons were observed in the range of 7.70-7.55, 7.32-7.24, 7.03-6.92, and 6.78-6.70 ppm integrating as 8, 4, 4 and 8 protons. The singlet peak for aliphatic protons was observed at 3.91 ppm integrating as 24 protons.

The positive ion MALDI-TOF mass spectrometry is an analysis method used in the characterization of Pcs. In this analysis, mostly the molecule ion type is the porphyrin radical cation (M^+). The MgPc **2** identified easily with 2,5-dihydroxybenzoic acid (DHB) as a MALDI matrix in the reflectron mode using a MALDI-TOF mass spectrometry. The molecular ion peak $[M+H]^+$ of the MgPc **2** was observed at m/z: 1146.75 Da (Fig. 2). In addition, elemental analysis result and mass spectrum of the MgPc **2** were good agreement with proposed structure. The elemental compositions (C, H and N) of the MgPc **2** are consistent with the proposed structures.

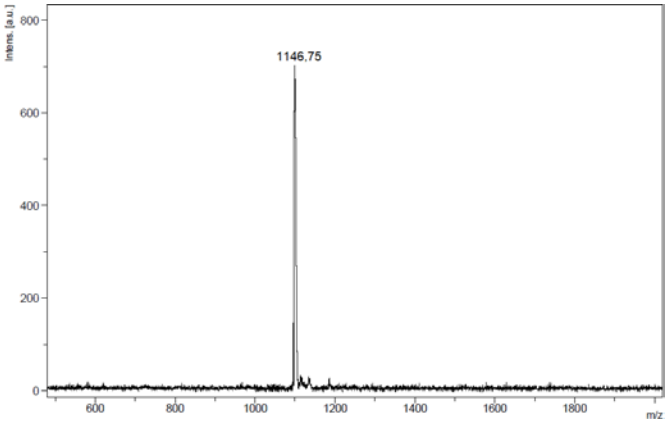

Figure 2. *Positive ion MALDI-TOF mass spectrum (reflectron mode) of the MgPc **2**, obtained in 2,5-dihydroxybenzoic acid.*

The electronic spectrum of the MPcs showed a monomeric behavior evidenced by a single (narrow) Q band for the MgPc **2** up to ~ 1.00 x 10^{-5} mol×dm^{-3} in DMF [34]. The electronic absorption spectra of the MgPc **2** showed characteristic a single Q band due to the π-π* transitions at 682 nm, with shoulders λ_{max}: 634 and 611 nm (Fig. 3). The Soret band (B band) of the MgPc **2** was observed at 362 nm (Fig. 2). In DMF, the substituted MgPc **2** showed 7 nm more red-shifted Q band compared to unsubstituted MgPc [27]. This is due to the presence of 2,6-dimethoxy phenoxy units on the phthalocyanine skeleton.

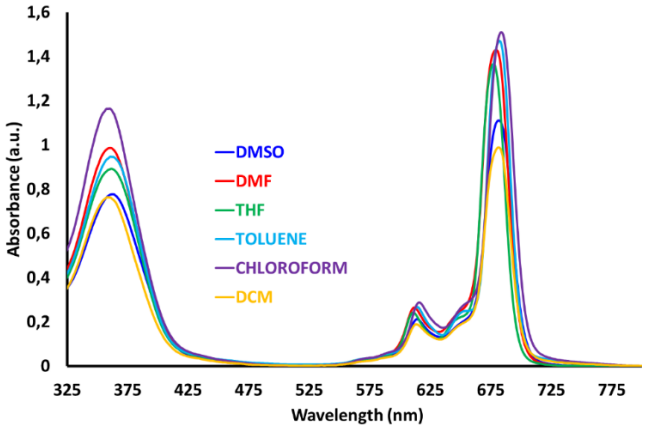

Figure 3. *Electronic absorption spectra of the MgPc **2** in different solvents. Concentration= ~1×10^{-5} mol×dm^{-3}.*

3.2. Aggregation studies

Aggregation can be defined as overlapping of monomers, dimers, and rings in solvent medium [35]. On phthalocyanines aggregation is determined by the concentration of the solution, the nature of the solvent, the temperature, the nature, and position of the substituents on the phthalocyanine skeleton, as well as the metal ion in the phthalocyanine center [35]. In the aggregated state the electronic structure of the complexed phthalocyanine rings is perturbed resulting in alternation of the ground and excited state electronic structures [36]. Dilution studies at different concentrations were researched at ambient temperature in DMF to better determine the aggregation properties of the MgPc **2**. To demonstrate compliance with the Lambert-Beer law, a linear regression analysis was performed between the density of the Q-bands and the concentrations of the MgPc **2**. The MgPc **2** did not aggregate in DMF at studied concentrations. Increasing the concentration for UV-*vis* studies of the MgPc **2** with concentrations ranging from 1.20 × 10^{-5} to 2.00 × 10^{-6} M in DMF, did not yield new bands on the higher energy side, which would mean the absence of aggregated species, and the absorption intensity obeys Lambert-Beer's law (Fig. 4).

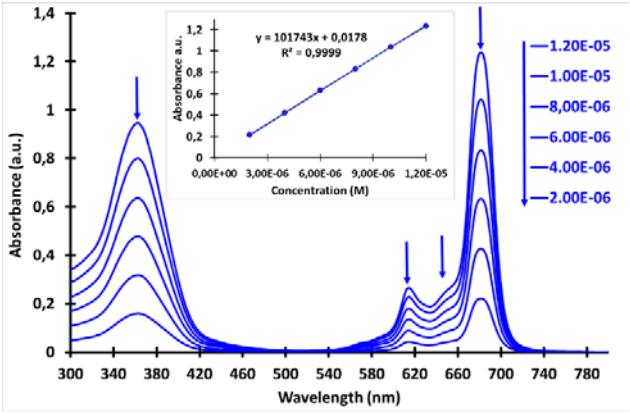

Figure 4. *Aggregation behavior of the MgPc **2** in DMF at different concentrations. (Inset: plot of absorbance vs. concentration).*

4. Photophysıcal propertıes

4.1. Fluorescence spectra

Fig. 5 shows fluorescence emission, absorption and excitation spectra of the MgPc 2 in DMF. Fluorescence spectra of the MgPc 2 were observed at 690 nm for emission and at 674 nm for excitation in DMF. The Stokes shift value of the MgPc 2 was found as 16 nm. The observed Stokes shift of the substituted MgPc 2 was higher than unsubstituted magnesium phthalocyanine in DMF [27]. The MgPc 2 showed similar fluorescence behavior in DMF (Fig. 5). The proximity of the wavelength of the MgPc 2 of the Q-band absorption to the Q band maxima of the excitation spectrum for the MgPc 2 suggests that the nuclear configurations of the ground and excited states are similar and not affected by excitation [34, 37].

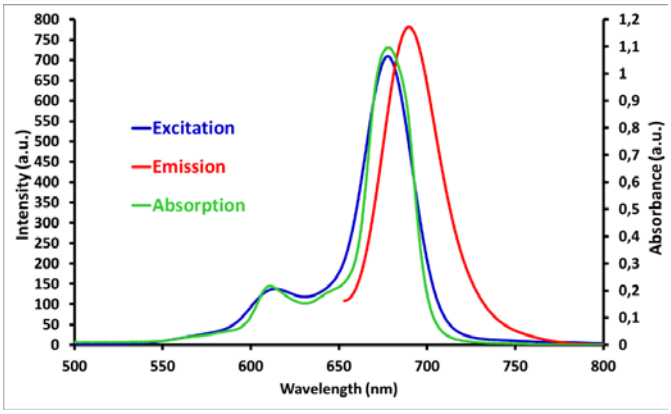

Figure 5. *Absorption, excitation, and emission spectra of the MgPc 2 in DMF. Excitation wavelength= 640 nm*

4.2. Fluorescence quantum yield and lifetime

The fluorescence quantum yield (Φ_F) is the ratio of the number of molecules that luminesce to the total number of the excited molecule. The Φ_F value of the MgPc 2 in DMF was found to be 0.27. The Φ_F value of the MgPc 2 was lower than unsubstituted magnesium (II) phthalocyanine in DMF [27], which implies that the presence of the 2,6-dimethoxyphenoxy units reduced the fluorescence quenching of the Pc molecule. The Φ_F value of the MgPc 2 is similar and typical of the other studied magnesium (II) Pc in DMF [37-47]. Fluorescence lifetime (τ_F) refers to the average time a molecule stays in its excited state before fluorescing, and its value is directly related to that of Φ_F, i.e. the longer the lifetime, the higher the quantum yield of fluorescence. Any factor that shortens the fluorescence lifetime of a fluorophore indirectly reduces the value of Φ_F. Such factors include internal conversion and intersystem crossing. As a result, the nature and the environment of a fluorophore determine its fluorescence lifetime. τ_F value of the MgPc 2 was calculated using the Strickler–Berg equation. In DMF, the τ_F value of the substituted MgPc 2 is 4.65 ns and longer compared to unsubstituted magnesium (II) phthalocyanine [27], suggesting less quenching by substitution. The τ_F value of the MgPc 2 is typical for the metallo-phthalocyanines [37-47]. The natural radiative lifetime (τ_0) and the rate constants for fluorescence (k_F) value of the MgPc 2 are 5.81×10^{-7} s^{-1} and 17.22 ns, respectively. The k_F value of the MgPc 2 is higher than unsubstituted magnesium (II) phthalocyanine in DMF [27]. The τ_0 of substituted the MgPc 2 is shorter when compared to magnesium (II) phthalocyanine in DMF [27]. It was determined to have richer fluorescent properties than its counterpart in the previous studies [27-30].

5. Conclusions

The synthesis and characterization of peripheral-tetrakis-2,6-dimethoxyphenoxy substituted magnesium (II) phthalocyanine 2 were presented in this study. The elemental analyses, FT-IR, ^{1}H NMR, UV–*vis*, fluorescence spectroscopy and MALDI-TOF-MS spectra confirmed the proposed structures of this phthalocyanine. It showed good solubility and non-aggregated species in dimethylsulfoxide, *N*, *N*-dimethylformamide, tetrahydrofuran, toluene, chloroform, and dichloromethane, which make it a candidate to use for many applications in different fields of science and technology. It is reported to have predominantly monomeric species in the solvents studied and show similar fluorescent behavior. It was reported that the presence of magnesium (II) metal ion as an alkaline earth metal in the phthalocyanine cavity, as well as enhancing its photophysical properties by substituting 2,6-dimethoxyphenoxy groups from peripheral positions to the phthalocyanine ring. It can also be a promising candidate for various technological applications, as it has rich photophysical properties.

Acknowledgements

This work was supported by Çanakkale Onsekiz Mart University, The Scientific Research Coordination Unit, Project number: FBA-2021-3355

References

[1]. Ingram D.J.E., Bennett J.E., “Paramagnetic resonance in phthalocyanine, chlorophyll, and hemoglobin derivatives”, The Journal of Chemical Physics, 22(6), (1954), 1136-1137.

[2]. Tian M., Wada T., Kimura-Sudab H., Sasabea H., “Novel non-aggregated unsymmetrical metallophthalocyanines for second-order non-linear optics”, Materials Chemistry Communication, 7(6), (1997), 861-863.

[3]. Sorokin A.B., "Phthalocyanine metal complexes in catalysis", Chemical Reviews, 113(10), (2013), 8152-8191.

[4]. Ben-Hur E., Rosenthal I., "Photosensitized inactivation of Chinese hamster cells by phthalocyanines", Photochemistry and Photobiology, 42(2), (1985), 129—133.

[5]. Bayrak R., Albay C., Koç M., Altın İ., Değirmencioğlu İ., Sökmen M., "Preparation of phthalocyanine/TiO2 nanocomposites for photocatalytic removal of toxic Cr(VI) ions Process", Process Safety and Environmental Protection, 102, (2016), 294-302.

[6]. Petritsch K., Friend R.H., Lux A., Rozenberg G., Moratti S.C., Holmes A.B., "Liquid Crystalline Phthalocyanines in Organic Solar Cells", Synthetic Metals, 102, (1999), 1776-1777.

[7]. Lü K., Zhou J., Zhou L., Chen X.S., Chan S.H., Sun Q., "Pre-combustion CO2 capture by transition metal ions embedded in phthalocyanine sheets", The Journal of Chemical Physics, 136(23), (2012), 234703.

[8]. Singh S., Aggarwal A., Bhupathiraju N. V. S. Dinesh K., Arianna G., Tiwari K., Drain C.M., "Glycosylated Porphyrins, Phthalocyanines, and Other Porphyrinoids for Diagnostics and Therapeutics", Chemical Reviews, 115(118), (2015), 10261−10306.

[9]. Snow A.W., The Porphyrin Handbook Phthalocyanines: Properties and Materials in Phthalocyanine Aggregation, Vol.17, K.M. Kadish, K.M. Smith, R. Guilard Eds. New York, Academic Press, 2003, 129-176.

[10]. Lukyanets E.A., Nemykin V.N., "The key role of peripheral substituents in the chemistry of phthalocyanines and their analogs", Journal of Porphyrins and Phthalocyanines, 14(01), (2010), 1-40.

[11]. Qi Z-L., Cheng Y-H., Xu Z., Chen M-L, "Recent Advances in Porphyrin-Based Materials for Metal Ions Detection", International Journal of Molecular Science 21, (2020), 5839- 5866.

[12]. Ishii K., Kobayashi N., in The Porphyrin Handbook, ed. K. M. Kadish, K. M. Smith, R. Guiard, Academic Press, New York, 2003, vol. 16, pp.1–42.

[13]. Janczak J., Kubiak R., "From 1,3-dicyanobenzene to 3-cyanobenzamide—its molecular structure in the gas-phase and in the crystal", Journal of Molecular Structure, 644 (2003), 13-21.

[14]. Janczak J., Śledź M., Kubiak R., "Catalytic trimerization of 2- and 4-cyanopyridine isomers to the triazine derivatives in presence of magnesium phthalocyanine", Journal of Molecular Structure, 659, (2003), 71-79.

[15]. McKewon N.B., "Phthalocyanine Materials: Synthesis, Structure and Function", Cambridge University Press, Cambridge, 1998.

[16]. Loutfy, R.O., Hor, A.M., DiPaola-Baranyi, G., Hsiao, C.K. "Electrophotographic Photoreceptors Incorporating Aggregated Phthalocyanines", Journal of Imaging Science, 29(3), (1985), 116-121.

[17]. Khe N.C., Aizawa M., Kaishi N.K., "The Use of Magnesium Phthalocyanine Compound as Electrophotographic Receptor Available for Laser Diode Recording", 1986(3), (1986), 393- 401.

[18]. Herbst W., Hunger K., Industrial Organic Pigments: Production, Properties, Applications, Wiley-VCH, New York, 1993.

[19]. Loutfy R.O., McIntre L.F., "Photoelectrochemical solar energy conversion by polycrystalline films of phthalocyanine" Solar Energy Materials, 6(4), (1982), 467-479.

[20]. Loutfy R.O.,"High-conversion polymerization of fluorescence probes. 1. Polymerization of methyl methacrylate", Macromolecules, 14, (1981), 270-275.

[21]. Ghosh A.K., Morel D.L., Feng T., Shaw R.F., Rowe C.A., "Photovoltaic and rectification properties of Al/Mg phthalocyanine/Ag Schottky-barrier cells", Journal of Applied Physics, 45, (1974), 230-236.

[22]. Bayona A.M.D.P., Mroz P., Thunshelle C., Hamblin M.R., Design features for optimization of tetrapyrrole macrocycles as antimicrobial and anticancer photosensitizers, Chemical Biology & Drug Design, 89(2), (2017), 192-206.

[23]. Soares A.R.M. , Tomé J.P.C. , Neves M.G.P.M.S., Tomé A.C., Cavaleiro J.A.S. , Torres T., "Synthesis of water-soluble phthalocyanines bearing four or eight d-galactose units", Carbohydrate Research, 344(4), (2009), 507-510.

[24]. Kandaz M. , Özkaya A.R., Koca A., Salih B., "Water and alcohol-soluble octakis-metalloporphyrazines

bearing sulfanyl polyetherol substituents: synthesis, spectroscopy, and electrochemistry", Dyes and Pigments, 74(2), (2007), 483-489.

[25]. Nishida M., Horiuchi H., Momotake A., Nishimura Y., Hiratsuka H., Arai T., "Singlet molecular oxygen generation by water-soluble phthalocyanine dendrimers with different aggregation behavior", Journal of Porphyrins and Phthalocyanines, 15, (2011), 47-53.

[26]. Janczak J., Idemori Y.M., "Synthesis, crystal structure and characterisation of aquamagnesium phthalocyanine—MgPc(H2O). The origin of an intense near-IR absorption of magnesium phthalocyanine known as 'X-phase' ", Polyhedron, 22(9), (2003), 1167-1181.

[27]. Taştemel A., Karaca B.Y., Durmuş M., Bulut M., "Photophysical and photochemical properties of novel metallophthalocyanines bearing 7-oxy-3-(m-methoxyphenyl) coumarin groups", Journal of Luminescence, 168, (2015), 163–171.

[28]. Pişkin Mehmet, "The novel 2,6-dimethoxyphenoxy substituted phthalocyanine dyes having high singlet oxygen quantum yields", Polyhedron, 104, (2016), 17-24.

[29]. Pişkin M., Öztürk Ö.F., Odabaş Z. "Determination of photophysical, photochemical and spectroscopic properties of novel lead(II) phthalocyanines", Polyhedron, 182, (2020), 114480.

[30]. Pişkin M., Öztürk Ö.F., Odabaş Z., "Newly Soluble and Non-Aggregated Copper(II) and Tin(II) Phthalocyanines: Synthesis, Characterization and Investigation of Photophysical and Photochemical-Responsive", Karaelmas Science and Engineering Journal, 7 (2), (2017), 627-637.

[31]. Pişkin M., Odabaş Z., "Synthesis, Characterization and Spectroscopic Properties of Novel Mono-Lutetium(III) Phthalocyanines", Karaelmas Science and Engineering Journal, 6 (2), (2016), 307-314.

[32]. Pişkin M., Can N., Odabaş Z., Altındal A., "Toluene vapor sensing characteristics of novel copper(II), indium(III),mono-lutetium(III) and tin(IV) phthalocyanines substituted with 2,6-dimethoxyphenoxy bioactive moieties", Journal of Porphyrins and Phthalocyanines, 22, (2018), 1–9.

[33]. [33] Kharisov B.I., Blanco L.M., Torres-Martinez L.M., García-Luna A., "Electrosynthesis of Phthalocyanines: Influence of Solvent", Industrial & Engineering Chemistry Research, 38(8) (1999) 2880-2887.

[34]. Stillman M.J., Nyokong T., Phthalocyanines Properties and Applications, vol. 1, C. C. Leznoff and A. B. P Lever, Eds., New York, Wiley-VCH Publishers,1989, ch. 3, pp. 133–289.

[35]. Enkelkamp H., Nolte R.J.M.," Molecular materials based on crown ether functionalized phthalocyanines", Journal of Porphyrins and Phthalocyanines, 4(5), (2000), 454-459.

[36]. Dominquez D.D., Snow A.W., Shirk J.S., Pong R.G.S., "Polyethyleneoxide-capped phthalocyanines: limiting phthalocyanine aggregation to dimer formation", Journal of Porphyrins and Phthalocyanines, 5(7), (2001), 582-592.

[37]. Nyokong T.,"Effects of substituents on the photochemical and photophysical properties of main group metal phthalocyanines", Coordination Chemistry Reviews, 251(13-14), (2007), 1707-1722.

[38]. Tuhl A., Chidawanayika W., Ibrahim H. M., Al-Awadi N., Litwinski C., Nyokong T., Behbehani H., Manaa H., Makhseed S., "Tetra and octa(2,6-di-iso-propylphenoxy)-substituted phthalocyanines: a comparative study among their photophysicochemical properties", Journal of Porphyrins and Phthalocyanines, 16(01), (2012), 163-174.

[39]. Kobayashi N., Ogata H., Nonaka N., Luk'yanets E.A., "Effect of Peripheral Substitution on the Electronic Absorption and Fluorescence Spectra of Metal-Free and Zinc Phthalocyanines", Chemistry—A European Journal, 9(20), (2003), 5123-5134.

[40]. Çapkın A., Pişkin M., Durmuş M., Bulut M., "Spectroscopic, photophysical and photochemical properties of newly metallo-phthalocyanines containing coumarin derivative", Journal of Molecular Structure,1213, (2020), 128145.

[41]. Akçay H.T., Pişkin M., Demirbaş Ü., Bayrak R., Durmuş M., Menteşe E., Kantekin H., "Novel triazole bearing zinc(II) and magnesium(II) metallo-phthalocyanines: Synthesis, characterization, photophysical and photochemical properties", Journal of Organometallic Chemistry, 745 (746), (2013), 379-386.

[42]. Kantekin H., Yalazan H., Kahriman N., Ertem B., Serdaroğlu V., Pişkin M., Durmuş M.,"New

peripherally and non-peripherally tetra-substituted metal-free, magnesium(II) and zinc(II) phthalocyanine derivatives fused chalcone units: Design, synthesis, spectroscopic characterization, photochemistry and photophysics", Journal of Photochemistry and Photobiology A: Chemistry, 361, (2018), 1-11.

[43]. Mutlu F., Pişkin M., Canpolat E., Öztürk Ö.F., "The new zinc(II) phthalocyanine directly conjugated with 4-butylmorpholine units: Synthesis, characterization, thermal, spectroscopic and photophysical properties", Journal of Molecular Structure, 1201, (2020), 127169.

[44]. Şahal H., Pişkin, M., Organ G.A., Öztürk Ö.F., Kaya M., Canpolat E., "Zinc(II) phthalocyanine containing Schiff base containing sulfonamide: synthesis, characterization, photophysical, and photochemical properties" J. Coord. Chem. 71 (22), (2018), 3763–3775

[45]. Demirbaş Ü., Pişkin M., Bayrak R., Durmuş M., Kantekin H. "Zinc(II) and lead(II) phthalocyanines bearing thiadiazole substituents: Synthesis, characterization, photophysical and photochemical properties", Journal of Molecular Structure, 1197, (2019) 594-602

[46]. Pişkin M., Canpolat E., Öztürk Ö.F. "The new zinc phthalocyanine having high singlet oxygen quantum yield substituted with new benzenesulfonamide derivative groups containing schiff base", Journal of Molecular Structure, 1202, (2020), 127181 .

[47]. Pişkin M., Öztürk Ö.F., Odabaş Z., "The photophysicochemical properties of peripherally and non-peripherally tetrakis-substituted lutetium(III) acetate phthalocyanines" Journal of Anatolian Chemistry and Chemical Education Research, 1(1), (2017), 1-12.

MANAS Journal of Engineering
ISSN 1694-7398 | e-ISSN 1694-7398

Volume 9, Special Issue 1, (2021) Pages 65-71
https://doi.org/10.51354/mjen.883804

Investigation of BSA adsorption performances of metal ion attached mineral particles embedded cryogel discs

Ömür Acet

Vocational School of Health Science, Pharmacy Services Program, Tarsus University, Tarsus, Turkey,
omuracet@tarsus.edu.tr, ORCID: 0000-0003-1864-5694

ABSTRACT

Blood plasma is rich in albumin protein. Albumin has some physiological duties. Investigations over separation of albumin has been paid considerable interest for its excellent potential in blood protein production. Natural pumice particles are non-toxic, reasonably priced and alternative adsorbents with excellent adsorption performance. In order to study the adsorption performance of BSA on composite cryogel discs with immobilized metal affinity chromatography (IMAC), Cu^{+2}-attached natural pumice particles were designed and they were embedded into cryogel generated medium. Cu^{2+}-attached natural pumice particle embedded composite cryogel discs (Cu^{2+}-NP-ECDs) were synthesized through polymerization of gel-former factors at minus temperatures. The characterization experiments of the Cu^{2+}-NP-ECDs were accomplished via SEM, FTIR experiments. The experiments were studied in a batch system. The highest amount of adsorbed BSA (356,8 mg/g particles) onto discs was obtained at pH 7.0 (phosphate buffer), 4 mg/mL concentration of BSA. As a result of conducted 30 adsorption-desorption experiments periods, there was no important change in adsorption performance of composite discs.

ARTICLE INFO

Research article

Received: 20.02.2021
Accepted: 02.04.2021

Keywords:
IMAC,
cryogel disc,
pumice particle,
bovine serum albumin,
adsorption

**Corresponding author*

1. Introduction

Lately, protein adsorption studies have become so widespread since it has been having very many practices in science of biological [1, 2, 3]. Blood plasma is rich in albumin protein [4]. It can deliver most drugs to target organs or cells where therapeutic missions are exerted [5, 6, 7]. Bovine serum albumin (BSA) is a globular blood plasma protein that fulfills as the stabilizator of enzymes [8]. The studies on the BSA separation has been paid much attention for its excellent potential by researchers.

Immobilized metal affinity chromatography (IMAC) presented by Porath et al. (1975) has turned into a common analytic and preparative separation technique on purification of some biomolecules [9, 10, 11, 12, 13]. Proteins with standard of high purity, which are extensively utilized in various fields, such as molecular biology and biotechnology, can be gained through His-tagged recombinant proteins which require IMAC [14, 10].

Cryogels are sub-category of hydrogels, which are bio-materials with excellent physical properties [15]. They have spongy morphologies with inter-connected macroporous, elastic structures and high mechanical robustness [16]. They are multi-purpose tools that could be turn to good purpose intended practices [17], such as purification and adsorption of some biomolecules [18, 19, 9], removal of heavy metals, dyes, [20, 21] and water treatment process [22]. The boosting of cryogel properties will carry forward its potential usage in various areas [17]. The weak side of cryogels that adsorption capacities of them for proteins is not at intended levels since the low surface area of inter-connected supermacropores within the matrix [23, 24, 25]. Enhancing the binding performance of cryogels has a great significance in bio-separation operations [26].

Some composite materials have been conducted to fulfill some important duties [27, 28].Natural particles (i.e., pumice particles) can be embedded in the cryogel structure to solve the problem of low surface area and achieve high efficiency in a short time. These composite polymers can be successfully applied in protein adsorption studies. Particle embedded cryogels are a special kind of cryogels column to widen the surface area owing to the unification of the unique features of both cryogels and particles. Pumice particles are natural adsorbents and have some advantages such as low cost, non-toxicity and high surface area for superior adsorption potential. [13, 29].

Here, Cu^{2+}-NP-ECDs were developed a new type of functional, low cost, composite cryogel disc for adsorption of BSA. Effects of pH, initial BSA concentration, ionic strength and temperature on BSA adsorption onto the Cu^{2+}-NP-ECDs were studied. Prepared composite cryogel disc and pristine cryogel disc were analysed with some characterizations concerning Fourier Transform Infrared Spectrophotometer (FTIR), Scanning Electron Microscopy (SEM), and attached amount of Cu^{2+} ions.

2. Materials and methods

2.1 Materials

The pumice particles were obtained from Pumice Research Centre (through Dr. Fatma Gurbuz), Süleyman Demirel University. 2-Hydroxyethyl methacrylate (HEMA) was provided from Fluka A.G (Buchs, Switzerland). *N,N'*-methylene-bis-acrylamide (MBAAm), *N,N,N',N'*-Tetramethylethylene-diamine (TEMED) and ammonium persulfate (APS) were purchased by Sigma (St. Louis, MO, USA). Other chemicals were purcahed at reagent grade from Merck AG (Darmstadt, Germany).

2.2 Preparation of natural pumice particles (NP)

Natural pumice particles have been occurred by pre-treatment to remove substances that may be extracted and affected the surface area of natural particles. For this purpose, the pumice particles were put into acid (3.0 M HCl) and alkali (3.0 M NaOH) solutions for 24 hours. And also, a heating method was conducted at 130 °C for 5 h for the removal of organic contaminants from the pore structures. Therefore, the surface area of natural particles has been enlarged. The treated particles were washed by using distilled water and dehydrated at 180 °C for 24 hours.

2.3 Attachment of Cu^{2+} ions to natural pumice particles (Cu^{2+}-NP)

Attachment process of Cu^{2+} ions to NP was operated (at room temperature, 2 h) with a Cu^{2+} ions containing solution (100 ppm, pH 5.0 tuned up with 0.01 M HCl). The quantity of binded Cu^{2+} ions onto NPs were calculated through beginning and last solutions of Cu^{2+} ion by a graphite furnace atomic absorption spectrometer (GFAAS, Analyst 800/PerkinElmer, Waltham, MA).

2.4 Formation of Cu^{2+}-attached natural pumice particle embedded composite cryogel disc (Cu^{2+}-NP-ECD)

HEMA (6 mmol) as monomer and MMBAm (1 mmol) as cross-linker were dissolved in deionized water (14 mL) by cryo-polymerization method. Then, 150 mg Cu^{2+}-NP was added into polymerization solution, APS (10%, w/v) as the free radical producer and TEMED (20 µL) as the initiator were added immediately. The prepared solution was poured into two glass layers (separated by 1.5 mm thick spacers) and was completed the polymerization in the refrigerator frozen at −12 °C for 24 h. After polymerization, it was thawed at room temperature. The synthesized composite cryogel discs were washed with deionized water until the impurities were removed. They were cut into circular discs (0.6 cm in diameter) with the help of a perforator. Lastly, they were put into buffer containing sodium azide (0.02 %) at 4 °C until usage.

2.5 Characterization of Cu^{2+}-NP-ECD sample and pristine cryogel

The functional groups of *Cu^{2+}-NP-ECD* and natural pumice were brightened by Fourier Transform Infrared Spectrometer (FTIR 8000 Series, Shimadzu, Japan). These samples (about 0.1 g) were combined separately with KBr. They were pelleted and analyzed by FTIR spectrophotometer.

The surface structure of pristine cryogel and Cu^{2+}-NP-ECD membrane discs were examined by using scanning electron microscopy (SEM, EVO LS 10 ZEISS 5600 SEM, Tokyo, Japan) at desired magnifications. For this purpose, the composite discs and pristine discs were swollen in deionized water. Then, they were put into absolute (98%) ethanol to replace water with alcohol molecules in the pores. Immediately after the alcohol is diffused, both samples were put into an oven (60 °C) to remove the alcohol molecules from the samples without harm their structures. The dewatered samples were coated with gold-palladium (40:60) and they were then taken to SEM for taking images.

2.6 Adsorption-elution stages of BSA from aqueous solutions

BSA adsorption experiments on composite cryogel discs were applied in a shaker bath system to investigate some parameters such as pH effect, initial BSA concentration, ionic strength effect and temperature factor. The control of temperature on the shaker system was followed with temperature control unit of shaker. The phosphate buffer (pH 7.0, 0.05 M) was implemented to equilibrate the system. All BSA readings were accomplished at 280 nm via a UV spectrophotometer (Shimadzu, Tokyo, Japan, Model 1601). Elution of adsorbed BSA from Cu^{2+}-NP-ECDs were accomplished with 0.5 M NaCl solution .

3. Results and discussion

3.1 Characterization of Cu^{2+}-NP-ECD sample and pristine cryogel

The quantity of Cu^{2+} ions binded to natural pumice particles was determined to be 40 mg/g. Additionally, It was checked for any ion leakage. No ion leakage was found. This outcome approved that washing process was satisfying.

The FTIR spectra of both natural pumice particles and pumice particle embedded cryogel discs were shown in Figure 1. SiO_2

is found in natural pumice particles about 70 % percentage [29]. The typical SiO_2 stretching vibration band of about was observed around 1006 cm^{-1}. On the other hand, the wavelength belonged to the SiO_2 groups in pumice particle embedded cryogel disc shifted to around 1022 cm^{-1}. The shift value in FTIR spectrum of natural pumice particle embedded cryogel discs can be attributed to the interaction of the Cu^{2+}-NP with the cryogel structure and the presence of the Cu^{2+}-NP in the cryogel disc structure.

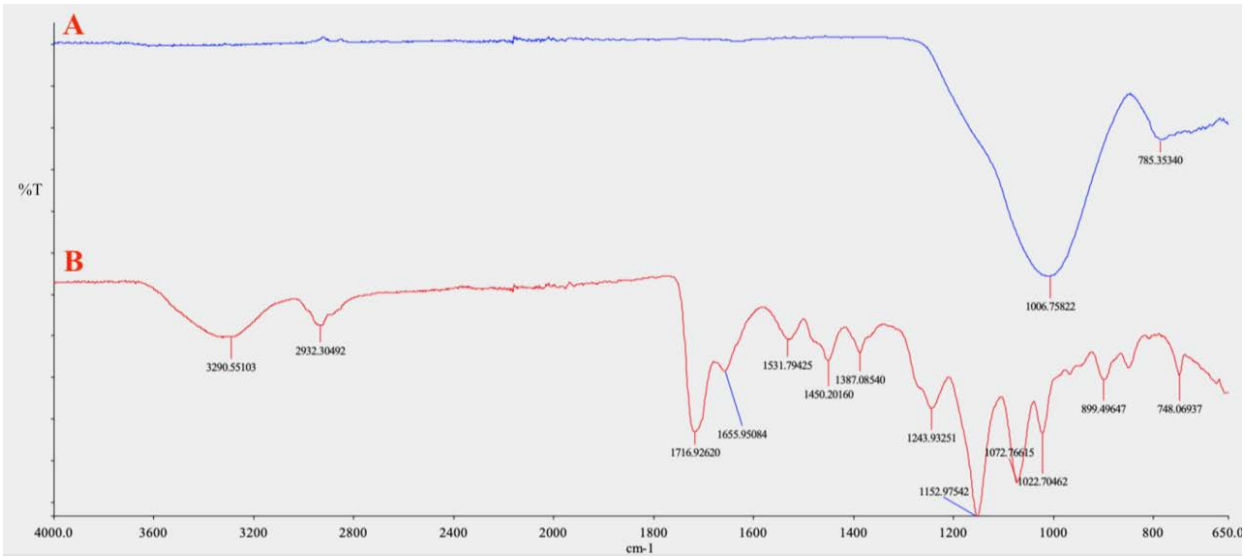

Figure 1. *FTIR spectra: Natural pumice (A) and Cu^{2+}-NP-ECDs (B).*

The structures of pristine cryogel discs and Cu^{2+}-NP-ECDs were portrayed by a scanning electron microscope to figured out surface structures in Figure 2. Even if pristine cryogel discs have perfect flow rate and unique interconnected routes, they have insufficient adsorption capacity in consequence of their low surface area. Cu^{2+}-NPs were combined with cryogel disc structures to cope with this problem of them. Cu^{2+}-NP-ECDs have highly porous and spongy morphologies as a result of uniformly dispersing of Cu^{2+}-NPs into cryogel discs. Therefore, this integrated morphological construction that high surface area fulfilled for circulation of mobile phase, enhanced the adsorption performance owing to the unification of these binary structure. Cu^{2+}-NP-ECDs displayed excellent BSA adsorption (mg/g) with respect to the adsorption capacity of pristine cryogel discs (mg/g).

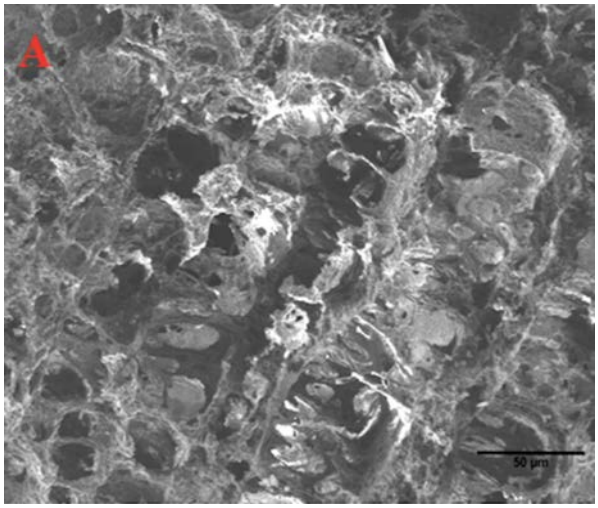

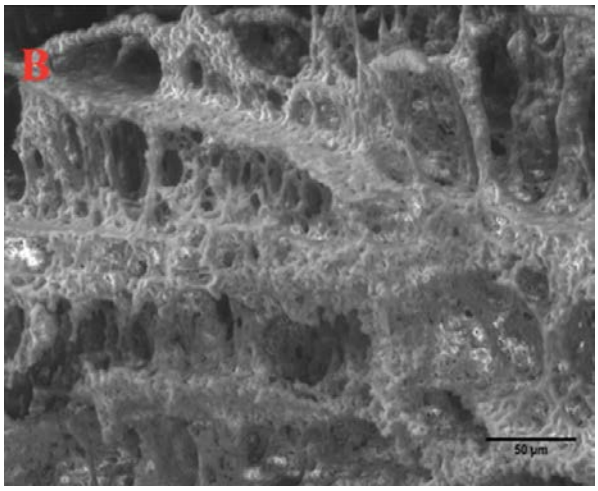

Figure 2. *SEM images of pristine cryogel discs (A) and Cu^{2+}-NP-ECDs (B).*

3.2. Effect of pH on BSA adsorption

Figure 3 indicates the effect of pH parameter on BSA adsorption. In all the occasions studied, the highest adsorption of BSA was observed at pH 7.0. Low adsorption was observed for acidic and alkaline pH regions with composite discs. The decrease in the BSA adsorption performance was seen in these regions because of electrostatic repulsion impacts between the opposite charged groups. The isoelectric pH of BSA is in the range of 4.7–5 in the literature [28]. Here, the highest adsorption was obtained at pH 7.0. Especially, the affinity between Cu^{+2} ions on natural pumice particles and BSA molecules (in particular, imidazole (histidine), thiol (cysteine), and indoyl (tryptophan)) are mainly responsible for the specific or electron donor–acceptor interactions. These specific interactions are based on the event of deprotonation of amino acid side changings (i.e., histidine and in particular primary amines such as lysine) of BSA with immobilized Cu^{+2} ions. The changings as conformational because of the specific interactions of BSA molecules at this pH point may also cause specific interaction [29].

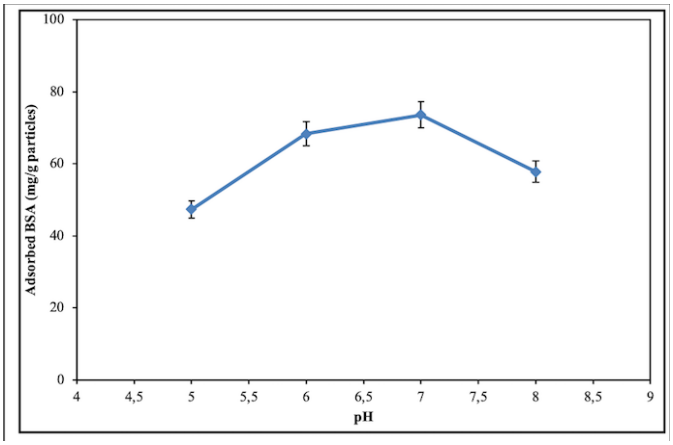

Figure 3. *Effect of pH on adsorption of BSA. (C_{BSA} 1 mg/mL, T: 25 °C)*

3.3 Effect of initial BSA concentration

The particles of natural origin with non-toxic, modifiable properties are attractive for biomedical applications. [30, 31]. The effect of initial concentration of BSA over adsorption have been shown in Figure 4. Different BSA concentrations (0.25 - 4 mg/mL) were conducted to investigate effect of initial BSA concentration on adsorption onto Cu^{2+}-NP-ECDs. Even though the adsorption of BSA pristine cryogel discs' having low adsorption performance, the power of adsorption capacity of Cu^{2+}-NP-ECDs were reasonably satisfactory (356,8 mg/g particles).

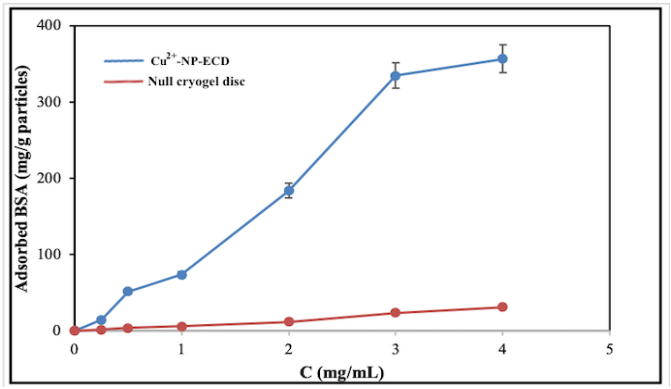

Figure 4. *The effect of initial BSA concentration on adsorption. (pH 7.0, T: 25 °C)*

The maximum adsorption capacity was obtained at 4 mg/mL. The binding sites on the Cu^{2+}-NP-ECDs for BSA were satiated. No significant increase in amount on adsorption seen after the BSA concentration of 4 mg/mL. This event can be emphasized by feeding of interaction regions on the cryogel disc occupied by BSA molecules. Consequently, Cu^{2+}-NP-ECD cryogel discs obtained a high adsorption of 356,8 mg/g particles. However, pristine cryogel discs achieved just 31,4 mg/g particles.

3.4 Effect of ionic strength

The effect of ionic strength on BSA adsorption also investigated at various concentrations (0-0.5 M) (Figure 5). As demonstrated in Figure 5, it was observed a diminish in adsorption versus boosting ionic strength. This situation is able to described as follows: The increase in salt concentration prevented the electrostatic interactions between the ligand and BSA as a result of masking the groups interacting on the adsorbent.

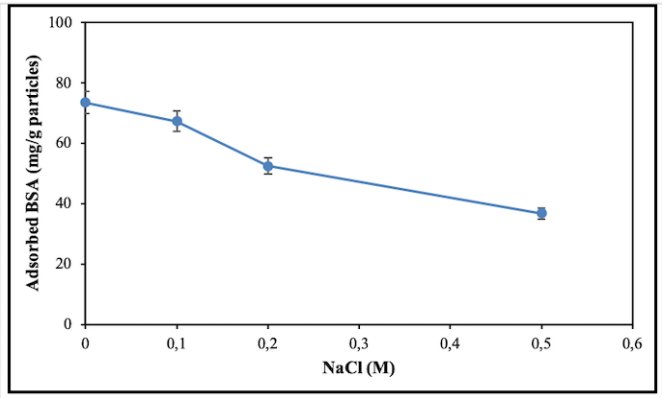

Figure 5. *The effect of ionic strength on adsorption of BSA. (pH 7.0, C_{BSA}: 1 mg/mL, T: 25 °C)*

The effect of temperature gives important information over adsorption of biomolecules on a adsorbent surface. The temperature parameter was carried out in the range of 5–35 °C. As demonstrated in Figure 6, the adsorption of BSA onto Cu^{2+}-NP-ECDs enhanced up to 25 °C, immediately after the adsorption was started to fall after 25 °C. This condition can be expressed with electrostatic interaction dominance between BSA molecules and Cu^{2+}-NP-ECDs.

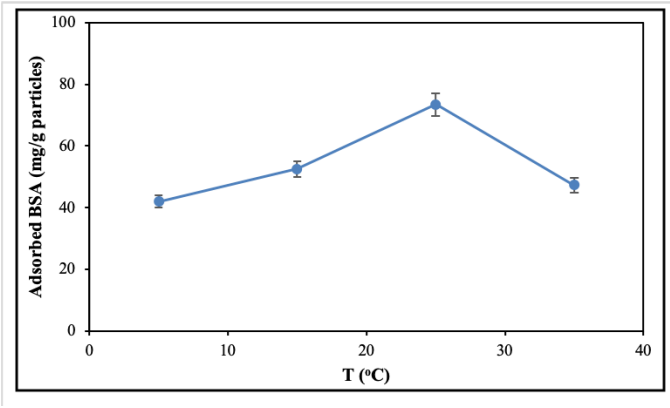

Figure 6. *The effect of temperature on adsorption of BSA. (pH 7.0, C_{BSA}: 1 mg/mL)*

The reusability of Cu^{2+}-NP-ECD composite cryogel discs presented satisfactory performance. Here, over 95% of adsorbed BSA was desorbed by 0.5 M NaCl. Adsorption-desorption stages were iterated 30 times by operating the same disc, and a considerable changing wasn't seen in cryogel disc structure.

4. Conclusion

In sum, Cu^{2+}-NP-ECDs were synthesized to study the adsorption capacity for BSA from aqueous solution. The highest adsorption value was obtained at pH 7.0 as 356,8 mg/g particles. The reusability experiments were endorsed 30 adsorption-desorption periods with 0.5 M NaCl by taking advantage of the same disc. The reusability of Cu^{2+}-NP-ECDs were extremely convenient to use for the next studies. The natural pumice particles and composite cryogel disc were characterized by SEM, FT-IR experiments. Under the light of all performed studies, it is expected that Cu^{2+}-NP-ECDs could be usefully applied for high amount separation of BSA molecules in the field of biomedicine and biotechnology.

Acknowledgements

The author would like to thank Prof. Dr. Fatma Gürbüz for supplying of natural pumice particles.

References

[1]. Hinderliter, Anne, Sylvio May., "Cooperative adsorption of proteins onto lipid membranes", Journal of Physics: Condensed Matter 18 (28), (2006), S1257.

[2]. Horbett, T. A., Brash, J. L., "Proteins at interfaces II", Washington, DC: American Chemical Society, 1995, 580.

[3]. Rauf, T. A., Anirudhan, T. S., "Synthesis and characterization of sulphonic acid ligand immobilized Aminopropyl silanetriol copolymer and evaluation of its Bovine serum albumin adsorption efficiency", Materials Today: Proceedings, (2020).

[4]. Zhang, J., Zhang, Z., Song, Y., Cai, H., "Bovine serum albumin (BSA) adsorption with Cibacron Blue F3GA attached chitosan microspheres", Reactive and Functional Polymers, 66(9), (2006), 916-923.

[5]. Ràfols, C., Zarza, S., Bosch, E. "Molecular interactions between some non-steroidal anti-inflammatory drugs (NSAID′ s) and bovine (BSA) or human (HSA) serum albumin estimated by means of isothermal titration calorimetry (ITC) and frontal analysis capillary electrophoresis (FA/CE)", Talanta, 130, (2014), 241-250.

[6]. Hage, D. S., "Affinity chromatography: a review of clinical applications", Clinical chemistry, 45(5), (1999), 593-615.

[7]. Bourassa, P., Kanakis, C. D., Tarantilis, P., Pollissiou, M. G., Tajmir-Riahi, H. A., "Resveratrol, genistein, and curcumin bind bovine serum albümin", The Journal of Physical Chemistry B, 114(9), (2010), 3348-3354.

[8]. Shah, M. T., Alveroglu, E., "Facile synthesis of nanogels modified Fe3O4@ Ag NPs for the efficient adsorption of bovine & human serum albümin",

Materials Science and Engineering: C, 118, (2021), 111390.

[9]. Acet, Ö., Aksoy, N. H., Erdönmez, D., Odabaşı, M., "Determination of some adsorption and kinetic parameters of α-amylase onto Cu+ 2-PHEMA beads embedded column", Artificial cells, nanomedicine, and biotechnology, 46(sup3), (2018), S538-S545.

[10]. Acet, Ö., Menteş, A., Odabaşı, M., "Assessment of a new dual effective combo polymer structure for separation of lysozyme from hen egg white", Polymer Bulletin, (2019), 1-17.

[11]. Serinbaş, A., Önal, B., Acet, Ö., Özdemir, N., Dzmitruk, V., Halets-Bui, I., Shcharbin, D., Odabaşı, M. "A new application of inorganic sorbent for biomolecules: IMAC practice of Fe3+-nano flowers for DNA separation", Materials Science and Engineering: C, 113, (2020), 111020.

[12]. Önal, B., Acet, Ö., Sanz, R., Sanz-Pérez, E. S., Erdönmez, D., Odabaşı, M. " Co-evaluation of interaction parameters of genomic and plasmid DNA for a new chromatographic medium", International journal of biological macromolecules, 141, (2019), 1183-1190.

[13]. Alacabey, İ., Acet, Ö., Önal, B., Dikici, E., Karakoç, V., Gürbüz, F., Alkan, H., Odabaşı, M., "Pumice particle interface: a case study for immunoglobulin G purification", Polymer Bulletin, (2020), 1-15.

[14]. Li, S., Yang, K., Liu, L., Zhao, B., Chen, Y., Li, X., Zhang, L., Zhang, Y. (2018). "Surface sieving coordinated IMAC material for purification of His-tagged proteins", Analytica chimica acta, 997, 9-15.

[15]. Rezaeeyazdi, M., Colombani, T., Memic, A., Bencherif, S. A., " Injectable hyaluronic acid-co-gelatin cryogels for tissue-engineering applications", Materials, 11(8), (2018),1374.

[16]. Hixon, K. R., Lu, T., Sell, S. A., "A comprehensive review of cryogels and their roles in tissue engineering applications", Acta biomaterialia, 62, (2017), 29-41.

[17]. Eggermont, L. J., Rogers, Z. J., Colombani, T., Memic, A., Bencherif, S. A. "Injectable cryogels for biomedical applications", Trends in biotechnology, 38(4), (2020), 418-431.

[18]. Önal, B., Odabaşı, M., "Design and application of a newly generated bio/synthetic cryogel column for DNA capturing", Polymer Bulletin, (2020), 1-18.

[19]. Ceylan, Ş., Odabaşı, M., "Novel adsorbent for DNA adsorption: Fe3+-attached sporopollenin particles embedded composite cryogels", Artificial cells, nanomedicine, and biotechnology, 41(6), (2013), 376-383.

[20]. Huseynli, S., Bakhshpour, M., Qureshi, T., Andac, M., Denizli, A., "Composite polymeric cryogel cartridges for selective removal of cadmium ions from aqueous solutions", Polymers, 12(5), (2020), 1149.

[21]. Gurbuz, F., Ozcan, A., Çiftçi, H., Acet, O., Odabasi, M., "Treatment of textile effluents through bio-composite column: Decolorization and COD reduction", International Journal of Environmental Science and Technology, 16(12), (2019), 8653-8662.

[22]. Gurbuz, F., Akpınar, Ş., Ozcan, S., Acet, Ö., Odabaşı, M., "Reducing arsenic and groundwater contaminants down to safe level for drinking purposes via Fe 3+-attached hybrid column", Environmental monitoring and assessment, 191(12), (2019), 1-14.

[23]. Persson, P., Baybak, O., Plieva, F., Galaev, I. Y., Mattiasson, B., Nilsson, B., Axelsson, A., "Characterization of a continuous supermacroporous monolithic matrix for chromatographic separation of large bioparticles", Biotechnology and bioengineering, 88(2), (2004), 224-236.

[24]. Ünlü, N., Ceylan, Ş., Erzengin, M., & Odabaşı, M., "Investigation of protein adsorption performance of Ni2+-attached diatomite particles embedded in composite monolithic cryogels", Journal of separation science, 34(16-17), (2011), 2173-2180.

[25]. Bereli, N., Şener, G., Altıntaş, E. B., Yavuz, H., Denizli, A., "Poly (glycidyl methacrylate) beads embedded cryogels for pseudo-specific affinity depletion of albumin and immunoglobulin G", Materials Science and Engineering: C, 30(2), (2010), 323-329.

[26]. Yao, K., Yun, J., Shen, S., Wang, L., He, X., Yu, X., "Characterization of a novel continuous supermacroporous monolithic cryogel embedded with nanoparticles for protein chromatography", Journal of Chromatography A, 1109(1), (2006), 103-110.

[27]. Sahiner, N., Karakoyun, N., Alpaslan, D., Aktas, N., "Biochar-embedded soft hydrogel and their use in Ag nanoparticle preparation and reduction of 4-nitro phenol", International Journal of Polymeric Materials and Polymeric Biomaterials, 62(11), (2013), 590-595.

[28]. Ajmal, M., Demirci, S., Siddiq, M., Aktas, N., Sahiner, N., "Simultaneous catalytic degradation/reduction of multiple organic compounds by modifiable p (methacrylic acid-co-acrylonitrile)–M (M: Cu, Co) microgel catalyst composites", New Journal of Chemistry, 40(2), (2016), 1485-1496.

[29]. Gurbuz, F., Ceylan, Ş., Odabaşı, M., Codd, G. A., "Hepatotoxic microcystin removal using pumice embedded monolithic composite cryogel as an alternative water treatment method", Water research, 90, (2016), 337-343.

[30]. Wang, X., Herting, G., Wallinder, I. O., Blomberg, E., " Adsorption of bovine serum albumin on silver surfaces enhances the release of silver at pH neutral conditions ", Physical Chemistry Chemical Physics, 17(28), (2015), 18524-18534.

[31]. Odabaši, M., Uzun, L., Denizli, A., "Porous magnetic chelator support for albumin adsorption by immobilized metal affinity separation", Journal of applied polymer science, 93(5), (2004), 2501-2510.

[32]. Sahiner, N., Sagbas, S., Aktas, N., "Preparation of macro-, micro-, and nano-sized poly (Tannic acid) particles with controllable degradability and multiple biomedical uses", Polymer degradation and stability, (2016), 129, 96-105.

[33]. Sagbas, S., Aktas, N., Sahiner, N., "Modified biofunctional p (tannic acid) microgels and their antimicrobial activity", Applied Surface Science, 354, (2015), 306-313.

MANAS Journal of Engineering
ISSN 1694-7398 | e-ISSN 1694-7398

Volume 9, Special Issue 1, (2021) Pages 72-81
https://doi.org/10.51354/mjen.889406

Determination and assessment of phosphorus assimilation capacity applying Vollenweider approach for Hazar Lake

Selma Ayaz*, Mehmet Dilaver

TUBITAK Marmara Research Center, Environment and Cleaner Production Institute, 41470, Kocaeli, Turkey, selma.ayaz@tubitak.gov.tr, ORCID: 0000-0001-5932-9060, mehmet.dilaver@tubitak.gov.tr, ORCID: 0000-0002-9805-9064

ABSTRACT

Eutrophication is a natural process for natural lakes and dams and the hydraulic retention time of this process is directly related to whether the assimilation capacity is exceeded depending on the current water quality and pressures consists of point and diffuse sources. Exceeding assimilation capacity is accepted good for biological productivity however this situation cannot be desired for water resources any time and preventive actions need to be taken to sustain good water quality. The Vollenweider OECD Method is a widely used and accepted approach in order to calculate current phosphorus loads for phosphorus limiting lakes and dams. In addition to OECD method, rational method is used frequently in calculating the flowrates via surface run-off after precipitation. In this study, the calculation of the assimilation capacity for phosphorus limiting lakes and dams using the Vollenweider Method and rational method for calculation of flowrates were applied for Hazar Lake's Basin example. When the apply proposed approach Hazar Lake's TP loading might be increased 3.7 times a year for desired oligotrophic upper boundary condition and 13.7 times a year for mesotrophic state boundary condition.

ARTICLE INFO

Research article

Received: 02.03.2021
Accepted: 24.03.2021

Keywords:
Hazar Lake,
phosphorus assimilation capacity,
Vollenweider method

**Corresponding author*

1. Introduction

Eutrophication is a natural process that results from accumulation of nutrients in receiving waterbodies. This process is occurred availability of plenty of least one limiting nutrient that causes excessive algal growth especially in lakes, ponds and dams. Even eutrophication occurs naturally over many decades, human activities, land use and agricultural activities may speed up the processes with additional nutrient via point and diffuse sources input. Limiting factor is determined that nutrient in shortest supply relative to plant growth requirements. Plants will grow until stopped by this limitation; for example, phosphorus in summer, temperature or light in fall or winter.

Researchers mentioned that nutrient limitation may not detectable easily with analytical methods however measured concentrations may be used for determination of nutrient limiting factor and trophic states for surface waterbodies [1-3]. When the literature studies are examined, it is seen that phosphorus becomes prominent as the limiting nutrient in many lakes [1- 5]. Determining the limiting nutrient is important in respect of controlling pollution in lakes under eutrophication threat. The use of TN:TP ratio is a general approach to determine the limiting nutrient [3,4]. As specified in the literature, the fact that TN:TP ratio is over 17 indicates that phosphorus is the limiting nutrient in the lake, and that it is less than 10 indicates that nitrogen is the limiting nutrient in the lake [3]. The TP concentration values are also used for the TN:TP ratios remaining out of these limits specified in the literature. For the lakes where TN:TP ratio is between 10 and 17, the fact that TP concentration is over 1 mg/L indicates that nitrogen is the limiting nutrient in the lake, and that it is less than 10 µg/L indicates that phosphorus is the limiting nutrient in the lake [4,6].

Different approaches have been investigated in order to calculate the assimilation capacities of the lake and dam reservoirs considered within the scope of the study. Among the main approaches considered are [1, 7-10]. Among these approaches, when Vollenweider's (1976) method is compared with the others, it is considered to be a more advantageous method since it deals with depth and surface area criteria. For this reason, the Vollenweider method has been preferred in the calculation of the assimilation capacity over the phosphorus parameter. Using the Vollenweider method, the relationship between the nutrient loads and the primary production has been calculated. In the method, the TP load and the *chlorophyll-a* parameter, among the loads coming from the

drainage basin of the lake water bodies, have been associated with each other.

Studied area Hazar Lake is a deep tectonic lake located in Eastern Anatolia [11]. Koçer and Şen (2014) was evaluate the nutrients ratio of Hazar Lake based on recent literature [12-14] and concentrations of nutrients according to OECD [15], Whittaker [16] and Vollenweider and Kerekes [17], Lake Hazar was found mesotrophic state [18]. Another local study finding lake is a typical an oligotrophic alkaline lake [11]. Even, current trophic state is between oligotrophic and mesotrophic level lake surround is getting high attraction with human activities therefore; lake is needed to be protected as mesotrophic state least in order to protect national importance wetland statute [19].

In this study, the assimilation capacity for phosphorus was calculated based on the current long data of chlorophyll-a condition of the Hazar Lake using the Vollenweider approach.

2. Materials and methods

2.1 Study area

Hazar Lake Basin, located in the Elazığ Province in Turkey. Hazar Lake Basin is geographically located between 38.359523° - 38.562718° Latitudes and 39.134583° - 39.587919° Longitudes according to ED50 Datum TM 39 Degree Projection System (Figure 1). The basin area is about 38374 hectare (ha). Study area consists of Hazar Lake, Zıkkım, Behrimaz, Kürk and Baharın rivers and the lake area is about 7897 ha based on CORINE 2018 data and at 1238 meter (m) elevation above the sea level. Behrimaz is the longest river is about 24.2 km length that connected to the Hazar Lake (Figure 2) and it contributes about 70 % of total surface flow to the Hazar Lake [20].

The lake is tectonic formed and second deepest natural lake in Turkey. Various deepest depths were reported between 80 m to 300 m in the literature [21]. Hazar Lake is having a highly alkaline and hardness characteristics and a high dissolved solids content, which results from carbonate concentrations [18]. The Lake is also having national importance wetland protection statue so far and possible candidate of RAMSAR site.

Hazar Lake Basin settlements are mainly villages and total 29 settlements located (Figure 3) within the basin with the 7831 people [22]. Usual settlements are not making pressure to the lake but this area is getting high attention and open to expansion.

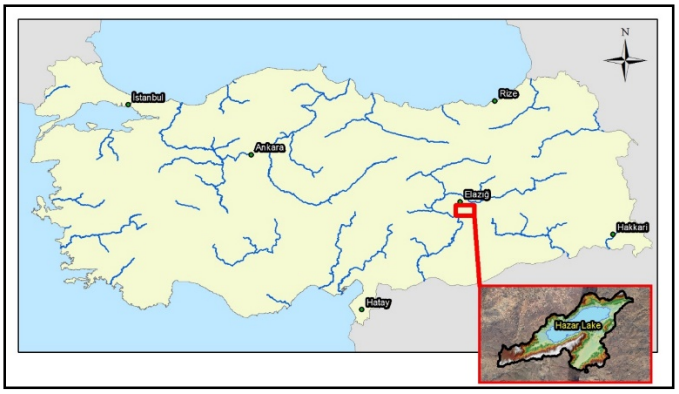

Figure 1. *Hazar Lake*

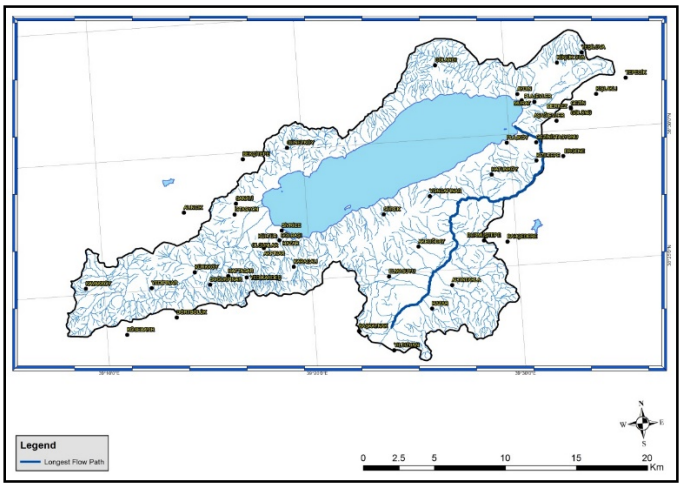

Figure 2. *Hazar Lake's Basin waterbodies*

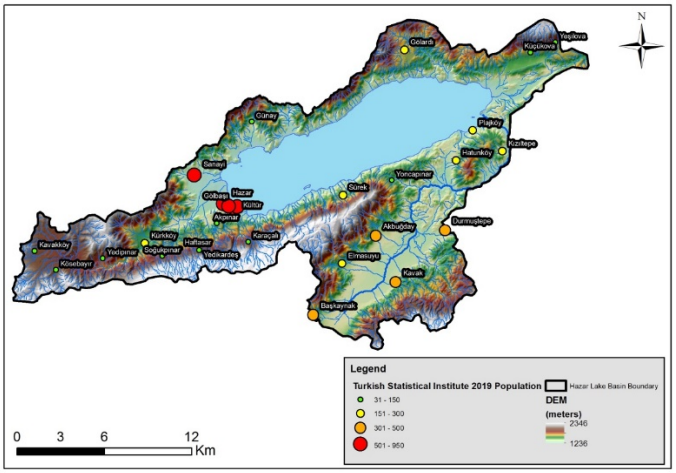

Figure 3. *Hazar Lake's settlements and population*

Detailed land use information was given in Figure 3. Forest and semi natural areas, agricultural areas and waterbodies areas are about 55.4%, 20.6% and 23.1% of total land use respectively based on CORINE 2018 data. According to this land use information that Hazar Lake's Basin is not high pressure in terms of land use (Figure 4).

It was selected as the study area that getting intention and threatening urban activities. Hazar Lake is natural deep lake and current trophic state is oligotrophic but the lake is under threat due to civilization. Therefore, lake water quality must be maintained with urgent actions.

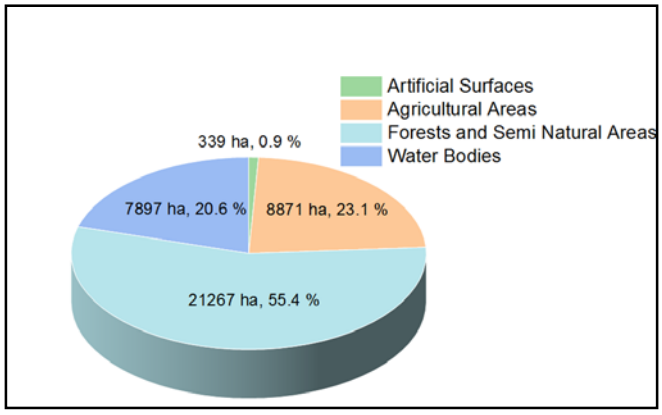

Figure 4. *Hazar Lake's Basin land use distribution (CORINE 2018)*

CORINE 2018 Code	CORINE 2018 Type	Area (Hectares)
1	Artificial Surfaces	339
2	Agricultural Areas	8871
3	Forests and semi natural areas	21267
5	Water Bodies	7897
	Total Basin Area	38374

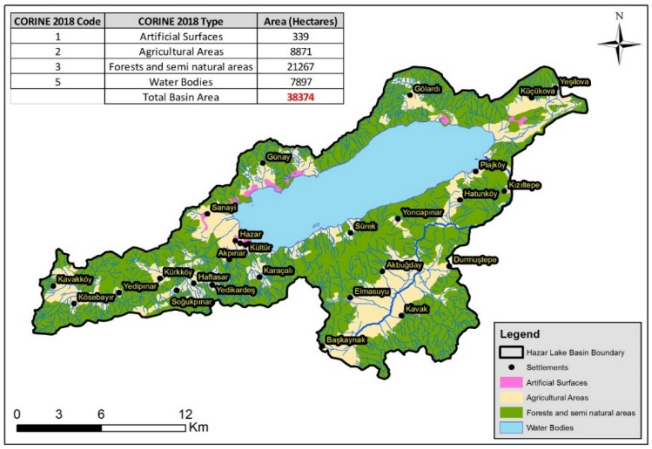

Figure 5. *Hazar Lake Land Use map (CORINE 2018)*

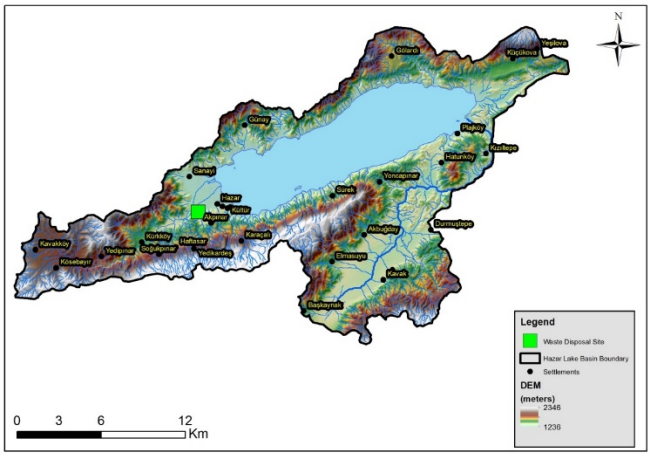

Figure 6. *Artificial Pressures*

There is no any industrialization and municipal wastewater discharge through receiving water bodies. Only pressures are one solid waste disposal site where it is located downstream of the basin and limited agricultural activities.

2.2 Peak surface run-off calculation with rational method

The rational method is one of the oldest methods used in surface runoff calculations. Although it is criticized since it does not need very detailed academic data, it is still widely applied in engineering calculations today due to this quality. Since some water bodies whose assimilation capacity has to be determined within the scope of the study is not included in the drainage basins, the rational method was preferred as the calculation method in order to determine the hydraulic retention times. As explained in the previous section, the reason for this preference is the fact that the rational method is the appropriate method in respect usability of available data. It is important to know the limitations and assumptions arising from this method in the application of the rational method.
The assumptions in the application of the rational method; i) precipitation has uniformly dispersed over the entire drainage area and is constant over time, ii) the calculated peak discharge has the same recurrence period as the statistically used precipitation intensity (I), iii) the surface runoff coefficient (c) is constant during the whole precipitation. On the other hand; the warning that should not be ignored in the application are the smaller the drainage area, the more accurate the results are and the rational method points to only one peak point in the unit hydrograph.
Equation used in the rational method:

$$Q = ciA/3600 \qquad \text{(Equation 1)}$$

Q: Maximum surface runoff (peak discharge) (m^3/s)
c: surface runoff coefficient (land cover/coefficient according to use)
i: Intensity of precipitation falling in the drainage time of water according to 10-year recurrence
A: Basin area (ha)

3600 number found out in the equation is the multiplier used during transition from the imperial units into the SI metric units.

The surface runoff coefficients decrease as the water leakiness increases according to land cover use. Its value is between 0-1. While the coefficient for the soil surfaces with vegetation cover approaches to 0, it approaches to 1 since the leak proof surfaces increases due to settlement and commercial activities. In the event there are mixed land use types within the basin, the surface runoff coefficients calculated according to the land use are calculated by the weighted average method. Since this is the case in all separate land uses within the basin, the weighted surface runoff coefficients have been determined according to the following formulation (Eq.2.).

$$C_w = \frac{\sum_{i=0}^{n} Cj\ Aj}{\sum_{i=0}^{n} Aj} \quad \text{(Equation 2)}$$

C_W = weighted surface runoff coefficient, C_j = surface runoff coefficient for j area
A_j = surface area (m^2), n = number of land use type

The simplified rational method used in this study has been presented in Table 1, the surface runoff coefficients (c) table.

Table 1. *Surface runoff coefficients (c) depending on the land cover use*

Land Cover Use	Surface Runoff Coefficient, c
Grass (garden)	0.05 – 0.35
Forest	0.05 – 0.25
Cultivable area	0.08 – 0.41
Grassland	0.1 – 0.5
Parks,	0.1 – 0.25
Undeveloped	0.1 – 0.3
Pasture land	0.12 – 0.62
Settlement	0.3 – 0.75
Commercial	0.5 – 0.95
Industrial areas	0.5 – 0.9
Asphalt roads	0.7 – 0.95
Covering roads	0.7 – 0.85
Roofs	0.75 – 0.95
Concrete roads	0.7 – 0.95

The water drainage time (Tc) is the time that passes until the precipitation falling to the top of the basin reaches at the output point, after the soil is saturated with precipitation and the small depressions in the area are filled with water. The basin varies according to the watercourse slope, vegetation cover status and other hydrological conditions.

$$K = L/\sqrt{S} \quad \text{(Equation 3)}$$

L: longest runoff length in the basin (m), S: slope along runoff (%)

$$Tc = 0.0195xK^{0.77} \quad \text{(Equation 4)}$$

The 10-year recurring 1-hour precipitation intensity (mm/h) values presented in Table 2 are the figures obtained from the lecture notes of Prof. Dr. Orhan Doğan, and use of the rational method in calculation of the precipitation intensity (I) has been found to be appropriate for the conditions in Turkey.

Table 2. *10 year recurring 1-hour precipitation intensity (mm/h)*

Station Name	Precipitation Intensity	Station Name	Precipitation Intensity (mm/h)	Station Name	Precipitation Intensity
İzmir	33,5	Kemalpaş	29,7	Manisa	41,8
Muğla	56,7	Aydın	23,0	Denizli	32,0
Mersin	38,5	Adana	36,0	Hatay	65,0
Dörtyol	58,0	Gaziantep	30,0	İslâhiye	19,9
Florya	25,0	Sarıyer	34,0	Çorlu	50,0
Edirne	36,4	Ankara	30,0	Bolu	17,2
Zonguldak	68,0	Niğde	32,2	Kastamonu	40,0
İnebolu	46,0	Çankırı	25,0	Çorum	35,0
Antalya	60,0	Isparta	32,4	Konya	13,0
Diyarbakır	22,0	Şanlıurfa	28,6	Ceylanpınar	19,5
Siirt	23,0	Kayseri	23,0	Kırşehir	21,5
Yozgat	16,0	Erzurum	21,4	Erzincan	25,0
Malatya	22,5	***Elazığ***	***28,5***	Samsun	40,0
Samsun	40,0	Merzifon	25,4	Van	23,0
Sivas	21,5	Trabzon	36,0	Rize	70,0
Eskişehir	33,4	Afyon	30,3	Kütahya	29,5
Uşak	26,5	Bilecik	22,7	Bursa	28,5
Balıkesir	33,5	Bandırma	50,0	Çanakkale	52,0
Kocaeli	38,0				

The values, the length (L) of the main runoff and the slope (S) along the runoff, have been calculated by using GIS for Hazar Lake's Basin. Tc values have been calculated by placing these values in equations (3) and (4), respectively. For the meteorological station closest to the basin where the Tc value has been calculated, the value present in the table above has been selected. Later on, the correction coefficient has been applied according to Tc value (**Table 3**).

Table 3. *Correction coefficients corresponding to Tc values*

Duration (minute)	Correction Coefficient
5	0,29
10	0,45
15	0,57
20	0,66
30	0,79
40	0,88
50	0,95
60	1,00

The values seen in **Table 2** are one-hour precipitation correction coefficients, and the values in **Table 3** have been subjected to correction according to the calculated Tc values duration.

$$\text{Corrected I value (mm/h)} = I \times 1.00 \times \left(\frac{I}{Tc}\right) \quad \text{(Equation 5)}$$

After the precipitation intensity (I) value is calculated in this way, the flow rate calculations have been completed by locating all the requirements of the equation (1) into their places.

2.3. Determining normalized total phosphorus with Vollenweider approach

While Vollenweider developed this method, he carried out examinations on phosphorus load and the ecosystem's response to this for 5 years in Western Europe, North America, Japan and Australia, in a total of 22 countries, on about 200 different water bodies (Figure 7). As a result of this study, a statistical correlation has been developed, which normalizes the annual areal total phosphorus (TP) load (Lp) falling on surface a lake with average depth (Z) and hydraulic retention time (Tw) [5].

$$\text{Normalized TP load (mg/m3)} = \frac{\text{L(P)/qs}}{1+\sqrt{Tw}} \qquad \text{(Equation 6)}$$

L(P) = Annual TP load on the area drained into the lake water body (mg P/m^2/y)
q_s = Value obtained by dividing depth (m) into hydraulic retention time (y)
T_w = Hydraulic retention time (y)

These values have been placed in their places in Equation (6), and the value of normalized phosphorus load for each basin has been found.

Hydraulic retention times, one of the most important parameters that have to be known when this method is used, have been calculated by using the values of the Current Flowrate Observation Stations (CFOS) obtained from the General Directorate of State Hydraulic Works (DSİ). If the CFOS output values of the dam reservoir and/or lake water bodies are in the water bodies that do not have output values, the annual runoff has been determined by using the total input AGİ values, and the hydraulic retention times have been calculated by proportioning this amount to the volume of water body. The total current values required for calculation of the hydraulic retention time of the lake or dam reservoir water bodies without any AGI values have been calculated by applying the "Rational Method" among the methods used for surface runoff calculation in the literature.

The calculated flow rates are the peak discharge values that may occur every 10 years in each basin, and a transition from these values into the annual total surface runoff value has been carried out. The lake and dam reservoir volumes have been divided into the calculated annual surface runoff values, and the hydraulic retention time (Tw) value required for the Vollenweider method for each water body has been calculated.

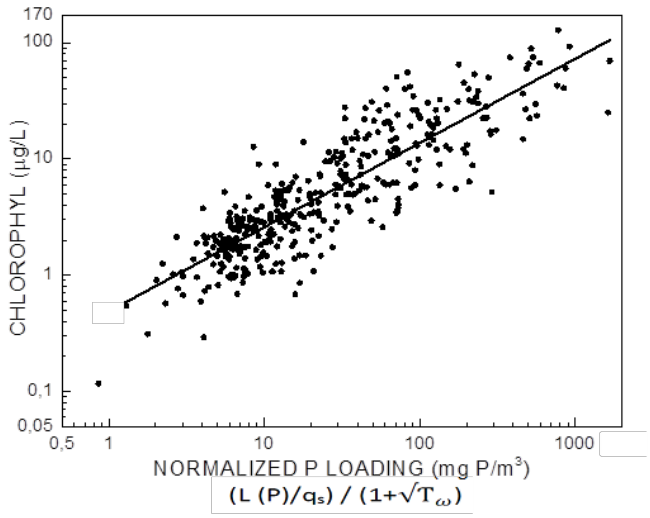

Figure 7. *Association of Chlorophyll a parameter and TP load [5]*

2.4. Water quality monitoring studies

Lake water samples were taken monthly (from April 2015 to April 2016) from 7 sampling points (Figure 8) and 3 different depths (surface, middle depth and deep depth) during 1-year period in the scope of HHAP Project [23]. Sampling locations and each depth of sampling for each sampling points were given in Table 4. These sampling locations and depths were chosen on site by monitoring team and previous studies considered too. Water samples were analyzed according to Standard Methods [24]. Alkalinity (mg/L $CaCO_3$) [2320 B. Titration Method], Secchi Disc (m) Chlorophyll-a analysis [S.M 10200 H. Spectrophotometric method], Total Nitrogen and Total Phosphorus (mg/L) [4500- P A, 4500- P J.]. Only, TN, TP and chlorophyll -a results were evaluated in order to calculate assimilation capacity with proposed approach.

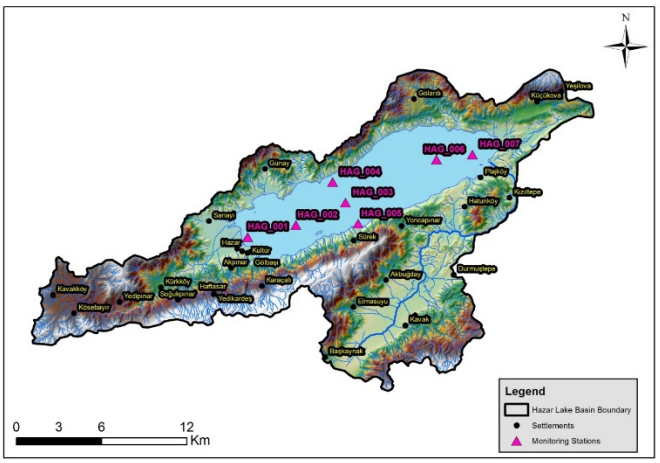

Figure 8. *Monitoring stations* [23].

Table 4. *Water quality sampling stations' information*

Station	Latitude	Longitude	Sampling Depth
HAG_1	38°27'27.02" N	39°18'29.75" E	1 20 40
HAG_2	38°27'53.77" N	39°20'49.91" E	1 30 60
HAG_3	38°28'44.55" N	39°23'14.10" E	1 40 80
HAG_4	38°29'31.64" N	39°22'37.46" E	1 15 30
HAG_5	38°27'56.43" N	39°23'50.52" E	1 20 40
HAG_6	38°30'21.87" N	39°27'39.71" E	1 40 80
HAG_7	38°30'33.22" N	39°29'23.66" E	1 40 80

2.5. Determining the Hazar Lake total phosphorus assimilation capacity

According to the approach given in *section 2.3*, calculations have been made and the normalized TP load corresponding to the value given for *"chlorophyll-a"* parameter. For this purposes 3 different TP values were calculated with applying oligotrophic and mesotrophic limit values of *chlorophyll-a* is specified in *Table 9: Limit Values of the Trophic Classification System in Lakes, Ponds and Dam Reservoirs*) of the Surface Water Quality Regulations, Appendix-6 in the lakes and dam reservoirs [25] and observed values of *chlorophyll-a* during monitoring studies. The L (P) phosphorus load corresponding to the determined normalized TP load has been calculated and accepted as the assimilation capacity.

3. Results and discussion

3.1 *Flow results*

Although obtained site observations flowrates values were used for assimilation capacity calculations, flow results were also calculated by rationale method in order to show absence of required and satisfied flowrate data. In order to apply rational method Hazar Lake Basin's land use was taken out CORINE 2018 data, average long path was calculated by GIS tool, "c" coefficients were taken from Table 1. Calculated weighted surface runoff coefficients were given in Table 5.

Table 5. *Hazar Lake Basin's surface runoff coefficients and areas based on CORINE 2018 land use data*

Code 2018	Area (ha)	Surface Runoff Coeff., c	Weighted surface runoff coeff. (C_iA_i , ha)
Industrial or commercial units (121)	26,85	0,85	22,82
Pastures (231)	143,48	0,35	50,22
Land principally occupied by agriculture, with significant areas of natural vegetation (243)	3188,95	0,3	956,69
Coniferous forest (312)	274,31	0,12	32,92
Natural grassland (321)	13442,50	0,3	4032,75
Transitional woodland/shrub (324)	1787,55	0,4	715,02
Beaches, dunes, sands (331)	246,89	0,25	61,72
Sparsely vegetated areas (333)	6125,99	0,4	2450,40
Water bodies (512)	7892,57	0,001	7,89
Discontinuous urban (1121)	151,96	0,55	83,58
Discontinuous rural (1122)	66,26	0,45	29,82
Non-irrigated arable land (2111)	141,05	0,45	63,47
Permanently irrigated land (2121)	2249,96	0,35	787,48
Complex cultivation patterns (2421)	330,41	0,4	132,16
Irrigated complex cultivation patterns (2422)	2113,47	0,3	634,04
Bare rock (3321)	161,17	0,9	145,05
Total	**38.343,38**		**10.206,04**

GIS analyses of Hazar Lake's Basin show that longest runoff length in the basin is 24199 m (Behrimaz River) and its' 1.507924 slopes as percentage which means every 100-meter-long distance makes 1.507924-meter elevation difference.

Flowrate were calculated by using rational method via Equation 1 after Equation 2-Equation 5 was calculated respectively and C_w, K, Tc and corrected I values obtained. After required values inserted in Equation 1 calculated flowrate value is 5.9 m^3/s. General Directorate of Water Affairs (DSİ) has long time flowrate data and annual average flowrate was 1.26 m^3/s for between 1984 and 2011 years. Most recent study reported the maximum flow was 2.95 m^3/s was in March and minimum flow was 0.35 m^3/s in October with a mean flowrate 1.40 m^3/s [20]. In this study DSİ data were used in order to determine hydraulic retention time and then normalized TP values.

3.2 Monitoring results

As mentioned in section 2.4, water quality samples were taken at 3 different depth and 7 different sampling locations and during April 2015-April 2016 period monthly. Since the stratification is over 10 meters and it is a deep lake, surface sampling has been taken into consideration (Figure 9). Another reason was why surface data used that deep lake may not allow mixing and stratification apart from temperature profile. This approach was supported by recent conducted study in Hazar Lake that lake was dimictic with completely mixed in spring and autumn and stratified during summer session forming a thermocline below 10 meter [18,21].

One of the best way the assessment of chlorophyll-a in order to apply proposed approach researchers mentioned that growing season and/or average summer epilimnetic algal chlorophyll need to be taken [14,26]. Therefore, instead of use all year data, 9 sampling periods between March to September including 2016 March and April months were taken consider for assessment of water quality.

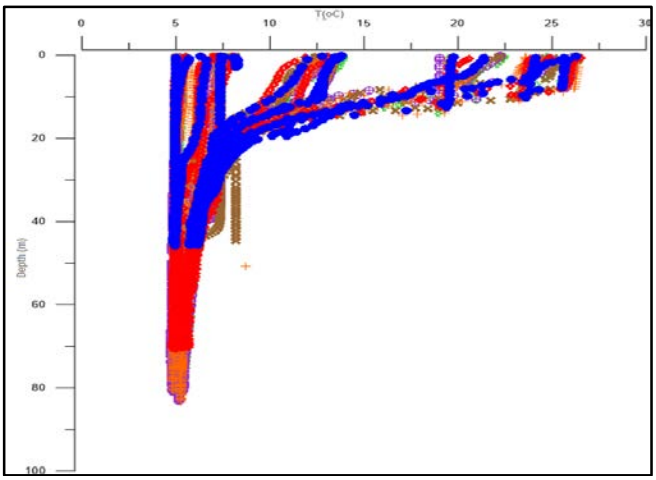

Figure 9. *Temperature profile assessment*

When the surface data were evaluated Hierarchical Cluster analysis was done with 63 data. Based on this cluster analysis of chlorophyll -a, TN, TP values of 7 sampling points could be used as one set. As a result of cluster analyses and temperature profile assessment was conducted with number of 63 surface data for each considered water quality parameters; alkalinity, chlorophyll-a, TN and TP.

Table 6. *Statistical analysis of monitoring data*

		Alkalinity (mg/L $CaCO_3$)	Chlorophyll -a (mg/m^3)	TN (mg/L)	TP (mg/L)
N	Valid	63.00	63.00	63.00	63.00
	Missing	0.00	0.00	0.00	0.00
Mean		***689.68***	***1.46***	***0.32***	***0.02***
Std. Error of Mean		2.24	0.09	0.02	0.00
Median		690.00	1.30	0.27	0.02
Std. Deviation		17.78	0.72	0.12	0.01
Variance		316.03	0.52	0.01	0.00
Range		140.00	3.70	0.57	0.04
Minimum		580.00	0.10	0.14	0.00
Maximum		720.00	3.80	0.71	0.04

Total numbers of 63 water samples were assessed in order to evaluate lake water quality in terms of alkalinity, Chlorophyll-a, TN and TP. Alkalinity results showed that the lake has moderately hard water. Total concentrations of alkalinity varied between 580 and 720 mg $CaCO_3$/L during the study, similar results were reported by Feray et.al, 2011 [27]. Same similarities were seen for Chlorophyll concentrations with 0.1 to 3.80 mg/m^3 varied and average is 1.46 mg/m^3 in previous studies [11,18,21]. Koçer, et.al, 2012 were reported annual average concentration of Chlorophyll-a was found between 1.2-1.4 µg/L with a 2.2 µg/L maximum concentration [21]. Koçer and Şen were reported 1.07-1.33 µg/L Chlorophyll concentrations first 10 meter among the 53 samples [18].

These amounts of Chlorophyll-a concentration mean that low productivity of phytoplankton which was related alkali conditions of lake [8]. Trophic state of lake was found between oligotrophic and mesotrophic according to national legislation (YSKY, 2016, Appendix VI, Table 9) when considering to growing season concentrations data of TN, TP and Chlorophyll-a. Another important finding was TN:TP ratio of Hazar Lake. Proposed approach can be applied only when the lake limiting nutrient is phosphorus. In this study, phosphorus was found as limiting nutrient with 16 TN:TP ratio for Hazar Lake.

3.4 Calculated NP loads based on Vollenweider approach

In this section 3 different TP values were calculated. First one is for current situation (observed chlorophyll -a results, 1.46 µg/L), second one is upper oligotrophic conditions (<3,5 µg/L Chl-a) and last one is for upper mesotrophic conditions (<9 µg/L Chl-a).

Table 7. *NP values for each corresponding chlorophyll-a values based on Vollenweider approach*

Chlorophyll -a (µg/L)	NP (mg/m^3)
1.46	4
3.5	9
9	55

In order to applying Vollenweider approach Hazar Lake required specifications were given below in Table 8. Lake Volume and surface area obtained from DSİ that in charge of operations of the lake. Hazar Lake average depth is determined to be 98 m [28].

Table 8. *Hazar Lake's required data for applying Vollenweider approach*

Lake Vol. (hm^3)	Lake Volume (m^3)	Lake Surface Area (m^2)	Aver. Depth (m)	Flow rate (m^3/s) *	Flow rate (m^3/y)	T_w (y)
7.000	7.000.000.000	78.970.000	98	1,26	39.735.360	176,17

*Long term annual average flowrate.

Average chlorophyll-a is 1.46 mg/L and NP is 4 based on Vollenweider graph. When the Eq 6 was applied Lp was 2.27 ton P/y. This amount is referred current TP situation. After Lp was obtained assimilation capacity of Hazar Lake might be calculated easily in order to meet desired trophic state.

3.5 Calculated phosphorus assimilation capacity of Hazar Lake

Required information were calculated previous sections applying Equations 1-6 in order to calculate assimilation capacity of Hazar Lake in line with Vollenweider OECD approach. In this study, 3 different scenarios were assumed, conserving current trophic state, allowing the increasing of TP load up to oligotrophic boundary condition and mesotrophic boundary condition. Calculated annual ton TP capacities are 2.51, 9.41 and 34.5 for current, oligotrophic and mesotrophic situation respectively. These findings point that the lake TP assimilation capacity might be increased 3.7 times in order to sustain oligotrophic situation or having 13.7 times higher capacity for mesotrophic situation. Obtained results were given in Table 9.

Table 9. *NP values for each corresponding chlorophyll-a values based on Vollenweider approach*

	Chlorophyll -a (µg/L)	Lp (mg/m^2/y)	TP (ton/y)	Assimilation Capacitive (ton P/y)*
Current Situation	1.46	31.8	2.51	-
Oligotrophic Situation	3.5**	119	9.41	6.90
Mesotrophic Situation	9.0**	437	34.50	32.00

*Assimilation capacity= Observed TP - Calculated TP
** YSKY, 2016 Appendix VI, Table 9

4. Conclusions

The aim of this study is to calculate the phosphorus assimilation capacity in phosphorus limiting lakes and dams semi-empirically using the available data and Vollenweider approach without model software. Therefore, Hazar Lake were chosen as a case study in order to plenty of available water quality data especially chlorophyll -a, TN and TP. As a result of applying Vollenweider approach that Hazar Lake's TP capacity has been already not filled and might have annually 6.90 ton TP to sustain oligotrophic condition or annually 32.00 ton TP for being mesotrophic lake. Current literature and in this study shows Hazar Lake is in good water quality and able to handle almost 13.7 times more TP loading a year. However, we suggest the Lake current water quality should sustain and new studies should be done next decades. In fact, that due to protection statute of Lake and having good potential being RAMSAR site the lake needs to be protected. Water Framework Directive required areas designated for the protection of habitats or species where the maintenance or improvement of the status of water is an important factor in their protection, including relevant Natura 2000 sites.

Acknowledgements

This study was prepared within the scope of the project "Determination of Sensitive Areas and Water Quality Objectives for Turkish River Basin Districts" (2012–2015) conducted by the former Ministry of Forestry and Water Affairs/Directorate General for Water Management in collaboration with TUBITAK MRC Environment and Cleaner Production Institute. The authors thank the General Directorate of Water Management for financial support. The lake monitoring studies were carried out by Fırat University (Prof. Dr. Bülent Şen, Prof. Dr. Feray Sönmez and their team). The authors also thank TUBITAK MRC Environment and Cleaner Production Institute's laboratory staff and GIS team for their valuable support.

References

[1]. Vollenweider R.A., "Advances in defining critical loading levels for phosphorus in lake eutrophication", Mem. 1st ital. Idrobiol., 33, (1976), 53–58.

[2]. Håkanson L., Bryhn A.C., Hytteborn J.K., "On the issue of limiting nutrient and predictions of cyanobacteria in aquatic systems", Sci. Total Environ., 379, (2007), 89–108.

[3]. Ekholm P., "N: P ratios in estimating nutrient limitation in aquatic systems", Finnish Environ. Inst., (2008), 11–14.

[4]. Sterner R.W., "On the phosphorus limitation paradigm for lakes", Int. Rev. Hydrobiol., 93, (2008), 433–445.

[5]. Jones R.A. Lee G.F., "Use of Vollenweider-OECD modeling to evaluate aquatic ecosystem functioning", Funct. Test. Aquat. Biota Estim. Hazards Chem., ASTM STP 988, J. Caims, Jr., and J.R. Pratt, Eds., American Society for Testing Materials, Philadephia, (1988), 17-27.

[6]. Ryding S.-O., Forsberg C., "Short-term load-response relationships in shallow, polluted lakes", In Hypertrophic Ecosyst., Springer, (1980), 95–103.

[7]. Jones J.R., Bachmann R.W., "Prediction of phosphorus and chlorophyll levels in lakes", J. (Water Pollut. Control Fed., (1976), 2176–2182.

[8]. Schindler D.W., "Factors regulating phytoplankton production and standing crop in the world's freshwaters", Limnol. Oceanogr. 23, (1978), 478–486.

[9]. Chapra S.C., "Total phosphorus model for the Great Lakes", J. Environ. Eng. Div., 103, (1977), 147–161.

[10]. Canfield Jr D.E., Bachmann R.W., "Prediction of total phosphorus concentrations, chlorophyll a, and Secchi depths in natural and artificial lakes", Can. J. Fish. Aquat. Sci., 38, (1981), 414–423.

[11]. Sonmez F., Kocer M.A.T., Alp M.T., Sen B., "An Evaluation On Characterıstıc Diatoms Of Alkaline Lake Hazar (Turkey)", Feb-Fresenıus Environ. Bull., (2018), 8519.

[12]. Håkanson L., Jansson M., "Principles of lake sedimentology", vol. 109, Springer-verlag, Berlin, (1983), pp. 24-31.

[13]. Emmanuel E., Keck G., Blanchard J.-M., Vermande P., Perrodin Y., "Toxicological effects of disinfections using sodium hypochlorite on aquatic organisms and its contribution to AOX formation in hospital wastewater", Environment international, 30, (2004), 891-900.

[14]. Nürnberg G.K., "Trophic state of clear and colored, soft-and hardwater lakes with special consideration of nutrients, anoxia, phytoplankton and fish", Lake Reserv. Manag., 12, (1996), 432–447.

[15]. Vollenweider R. A., "Eutrophication of waters: monitoring, assessment and control". Organisation for Economic Co-operation and Development; Washington, DC: Sold by OECD Publications and Information Center, 1982.

[16]. Whittaker R.H., "Communities and ecosystems", Communities Ecosyst., Macmillan Publishing Co., Inc., New York, USA, 1975.

[17]. Vollenweider R.A., Kerekes J., "OECD cooperative programme for monitoring of inland waters (eutrophication control)", Synth. Report. OECD, Paris, 1980.

[18]. Kocer M.A.T., Şen B., "Some factors affecting the abundance of phytoplankton in an unproductive alkaline lake (Lake Hazar, Turkey)", Turk. J. Botany., 38, (2014), 790–799.

[19]. Ayaz S., "Hazar Lake Management Plan Project I. Stage", TÜBİTAK MRC, Energy Systems and Environment Institute, 2002.

[20]. Varol M., "Stream Inputs To Lake Hazar (Eastern Anatolia-Turkey)", Environ. Eng.Manag. J., 18, 1, (2019), 185-194.

[21]. Kocer M.A.T., Şen B., "The seasonal succession of diatoms in phytoplankton of a soda lake (Lake Hazar, Turkey)", Turk. J. Botany., 36, (2012), 738–746.

[22]. TURKSTAT, "Turkish Statistical Institute 2020 Reports", Available: https://www.tuik.gov.tr/ [Accessed:April 13, 2021]

[23]. TÜBİTAK MRC, "HHAP Project Determination of Sensitive Areas and Water Quality Objectives for Turkish River Basin Districts Project (2012–2015)", TÜBİTAK MRC, Environment and Cleaner Production Institute, 2016

[24]. Baird R.B., "Standard Methods for the Examination of Water and Wastewater", 23rd ed., Water Environment Federation, American Public Health Association, American Water Works Association, 2017.

[25]. YSKY, "Regulation on Surface Water Quality (RSWQ) (Turkey) (2016) 29797/ 16.8.2016", Ministry of Forestry and Water Affairs, Available: https://www.resmigazete.gov.tr/eskiler/2016/08/20160810-9.htm. [Accessed: April 13, 2021]

[26]. Phillips G., Pietiläinen O.-P., Carvalho L., Solimini A., Solheim A.L., Cardoso A.C., "Chlorophyll–nutrient relationships of different lake types using a large European dataset", Aquat. Ecol., 42, (2008), 213–226.

[27]. Sonmez, F., Sen, B., "Seasonality and Distribution of Epilithic Diatoms in an Alkaline Lake (Lake Hazar,

Elazig, Turkey)", Fresenius Environmental Bulletin, 20, (6), 1458-1464.

[28]. Şen B., Alp M.T., Özrenk F., Ercan Y., Yıldırım V., "A study on the amount of plant nutrients and organic matters carried into the Hazar Lake (Elazığ-Türkiye)", Fresenius Environ. Bull., 8, (1999), 272–279.

MANAS Journal of Engineering
ISSN 1694-7398 | e-ISSN 1694-7398

Volume 9, Special Issue 1, (2021) Pages 82-96
https://doi.org/10.51354/mjen.780716

A novel numerical implementation for solving time fractional telegraph differential equations having multiple space and time delays via Delannoy polynomial

Ömür Kıvanç Kürkçü

Department of Engineering Basic Sciences, Konya Technical University, Konya, Turkey,
omurkivanc@outlook.com, ORCID: 0000-0002-3987-7171

ABSTRACT

This paper is concerned with solving numerically the time fractional telegraph equations having multiple space and time delays by proposing a novel matrix-collocation method dependent on the Delannoy polynomial. This method enables easy and fast approximation tool consisting of the matrix expansions of the functions using only the Delannoy polynomial. Thus, the solutions are obtained directly from a unique matrix system. Also, the residual error computation, which involves the same procedure as the method, provides the improvement of the solutions. The method is evaluated under some valuable error tests in the numerical applications. To do this, a unique computer module is devised. The present results are compared with those of the existing methods in the literature, in order to oversee the precision and efficiency of the method. One can express that the proposed method admits very consistent approximation for the equations in question.

ARTICLE INFO

Research article

Received: *20.04.2020*

Accepted: *14.10.2020*

Keywords:
delannoy polynomial,
matrix-collocation method,
multiple delays,
telegraph equation.

1. Introduction

In this study, we aim to implement a novel matrix-collocation method dependent on the Delannoy polynomial to solve efficiently and precisely the time fractional telegraph differential equations having multiple space and time delays

$$ {}_t^C\mathcal{D}_0^{\alpha} u(x,t) + {}_t^C\mathcal{D}_0^{\beta} u(x-\tau_1, t-\tau_2) + p_1 u(x-\tau_3, t-\tau_4) = p_2\, {}_xD^2 u(x,t) + g(x,t), \tag{1} $$

subject to the initial condition $u(x,c) = \lambda_1(x)$ in Ω and the boundary conditions $u(a,t) = \lambda_2(t)$ and $u(b,t) = \lambda_3(t)$ on $\partial\Omega$,

where $u(x,t)$ and $g(x,t)$ are analytic functions on the domain

$$ \Omega = \{(x,t) : a \le x \le b,\ c \le t \le d\}, $$

${}_t^C\mathcal{D}_0^{\alpha}$ (similarly ${}_t^C\mathcal{D}_0^{\beta}$) $(1 < \alpha \le 2,\ 0 < \beta \le 1)$ is the time fractional derivative operator in the Caputo sense [1]; $\{p_1, p_2\}$ are the real constants; $\{\tau_1, \tau_3\}$ and $\{\tau_2, \tau_4\}$ are the spatial and temporal delays, respectively.

It is explicit to state that the partial differential equations (PDEs) govern physical and mathematical modelling of many natural phenomena arising in real world applications. PDEs can easily built a model into a mathematical formation

by enclosing time and space variables on specific domains of this model, such as rectangular plate or elliptic domain. In particular, the fields of application of PDEs have been spread due to the inclusion of the time or space fractional manner of partial derivatives. In fact, there is a growing interest and attention in the fractional PDEs (FPDEs), with the developments of real world hybrid models occurring especially in fluid mechanics [2], electrical circuits [3], viscoelasticity [4], heat transfer [5], finance [6], diffusion phenomena [7] and so on. In addition to these composite structured equations, temporal or spatial lags may also be encountered due to the indeterminable physical conditions. These complexities can be detected via delay arguments in FPDEs. Inherently, the variational combinations of these instruments make FPDEs too severe problems to handle them analytically. Therefore, the numerical implementations have been proposed to acquire the approximate solutions of FPDEs of delay types so far. For example, Kürkçü et al. [8] have applied a matrix method based on the matching polynomial of complete graph to solve the space-time FPDEs of delay type. Dehestani et al. [9] have employed the Genocchi hybrid collocation method for solving several FPDEs containing delay arguments. Rihan [10] has constructed the semi-discrete and ϑ-methods for delay FPDEs of parabolic type. Usman et al. [11] have utilized an operational matrix method dependent on the shifted Gegenbauer polynomials to treat FPDEs of delays. Motivating by these mentioned studies, we introduce a novel methodology consisting of the matrix expansions of the functions via the Delannoy polynomial for solving equation (1). The main advantage of the proposed method is that it directly converts the functions in equation (1) into the matrix expansions, applying the Delannoy polynomial base. This inventive tool provides easy and fast computation to get the approximate solutions.

On the other hand, the telegraph differential equations (TDEs) can be appeared differently in the study of the wave propagation theory on the behaviour of electrical signals found in a cable transmission system [12, 13], particle transport applications [14] and Brownian motion processes [15]. As a fractional sense of TEs, some numerical studies can be detailed as follows: Kumar et al. [16] have studied a local meshless method to acquire the solutions of time fractional TDEs with one and two dimensional forms. Hosseini et al. [3] have deployed the radial basis function method for time fractional TDEs. Wang et al. [17] have solved a class of time fractional TDE subjected to the initial conditions by implementing the reproducing kernel method. Pandey and Mishra [18] have established the numerical simulation of the time-space fractional TDEs using the homotopy analysis method and Sumudu transform. For the numerical solutions of TDEs of integer order, the Galerkin-type method [19], the thin plate splines radial basis method [20], the Chebyshev cardinal function method [21], the Crank–Nicolson finite difference scheme and Haar wavelet method [22], and the cubic B-spline collocation method [23] have been deployed up to now. We here draw attention to the fact that TEs of equation (1) type are hardly found in the literature. Indeed, we establish and solve equation (1) efficiently via this study.

The layout of this paper is shaped as follows: Section 1.1 presents a brief information about the Delannoy numbers and their polynomial form. Section 2 admits the details of the proposed method and its matrix expansions related to the equation (1). Section 3 reveals the properties of the residual error computation to improve the obtained solutions emerged from Section 2. Section 4 applies three specific problems to exhibit the efficiency and precision of the method. Section 5 emphasizes on a competitive innovation and developments via the method, interpreting the results obtained in Section 4.

1.1. Preliminary to Delannoy numbers and their polynomial form

The Delannoy numbers $D(n,k)$ $(n,k \in \mathbb{N})$, which are named after Henri Delannoy [24], are related to the lattice path enumeration (n,k) using the number of walk from the initial point $(0,0)$ to (n,k) with $(0,1)$, $(1,1)$ or $(1,0)$ increments [24, 25]. The generating function of the Delannoy walks is formulated as

$$F[x,y,t] = \sum_{n\geq 0}(xt + yt + xyt)^n = \frac{1}{1 - t(x + y + xy)},$$

where x, y and xy imply the three steps $(0,1)$, $(1,1)$ and $(1,0)$, respectively, and t implies the length of the walk [25].

The main implicit formulation of the Delannoy numbers can be stated as follows [25, 26]:

$$D(n,k)=\sum_{i=0}^{n}\binom{n}{i}\binom{k}{i}2^i=\binom{n+k}{k}{}_2F_1\left(-n,-k;-(n+k);-1\right),$$

where ${}_2F_1\left(a,b;\ c;\ t\right)$ is a hypergeometric function.

A fundamental recurrence relation of $D(n,k)$ is defined to be

$$D(n,k)=D(n-1,k)+D(n-1,k-1)+D(n,k-1),$$

where $D(0,0)=1$ [26, 27] and this relation can provide the generating function (see [27])

$$\sum_{n,k=0}^{\infty}D(n,k)x^n y^k=(1-x-y-xy)^{-1}.$$

The central Delannoy numbers, which are denoted by $D(n,n)$ or briefly $D(n)$ instead of k, can be defined to be (see [28])

$$D(n,n)=D(n)=\sum_{i=0}^{n}\binom{n}{i}\binom{n+i}{i},$$

or another expression (see [28])

$$D(n)=\sum_{i=0}^{n}\binom{n}{i}^2 2^i.$$

Their recurrence relation stands for (see [29])

$$nD(n)=3(2n-1)D(n-1)-(n-1)D(n-2),$$

and also their generating function has the form (see [26, 27])

$$\sum_{n=0}^{\infty}D(n)x^n=(1-6x+x^2)^{-1/2}.$$

$D(n)$ yields an algebraical relation between the Legendre polynomial $P_n(x)$ as (see [25])

$$D(n)=P_n(3),$$

and more uniquely, $D(n)$ stands for the equality

$$D(n+\alpha,n)=P_n^{(\alpha,0)}(3),\ \forall\alpha\in\mathbb{Z},\ \ni\ \alpha\geq -n,$$

where $P_n^{(\alpha,0)}(x)$ is the Jacobi polynomial with the parameters $(\alpha,0)$ [30].

As a combinatorial purpose, $D(n)$ is equivalent to the generalized central trinomial coefficients $T_n(3,2)$, where $T_n(b,c)$ implies the coefficient of x^n when $(x^2+bx+c)^n$ is expanded algebraically [31].

Indeed, the Delannoy numbers can occur in the applications of lattice and posets [25], number theory [32] and the formulation of the alignments between DNA sequences [33].

In view of the Delannoy numbers, their polynomial implicit form was established by Sun [31] as

$$D_n(x) = \sum_{i=0}^{n} \binom{n}{i}\binom{n+i}{i} x^i. \tag{2}$$

In particular, the Delannoy polynomial can be associated with the Legendre polynomial $P_n(x)$ and the generalized central trinomial coefficients $T_n(b,c)$ [31], so

$$D_n(x) = P_n(2x+1) = T_n(2x+1, x^2+x), \ \forall x \in \mathbb{Z}.$$

In addition to these coincides, the Delannoy polynomial has also a natural connection with the Schmidt polynomial $S_n(\alpha, x)$ for $\alpha = 1$ [34].

2. Foundation of the matrix expansions for method of solution

In this section, the matrix expansions of the functions in equation (1) are derived to form a fundamental basis of the proposed method. Supposing that $u(x,t)$ be an analytic function on Ω and ${}_xD^n$ (or ${}_tD^n$) is a differential operator of integer order n with respect to x (or t). Firstly, the Delannoy polynomial solution of equation (1) is found to be

$$u(x,t) \cong u_N(x,t) = \sum_{m=0}^{N}\sum_{n=0}^{N} z_{mn} D_m(x) D_n(t), \tag{3}$$

where z_{mn}'s are the unknown Delannoy coefficients to be identified via the method and $D_m(x)$ represents the Delannoy polynomial (2).

The matrix expansion of the Delannoy polynomial solution (3) can be constructed as

$$u_N(x,t) = \boldsymbol{D}(x)\overline{\boldsymbol{D}(t)}\boldsymbol{A}, \tag{4}$$

where

$$\boldsymbol{D}(x) = \begin{bmatrix} D_0(x) & D_1(x) & \cdots & D_N(x) \end{bmatrix},$$

$$\overline{\boldsymbol{D}(t)} = \begin{bmatrix} \boldsymbol{D}(t) & 0 & \cdots & 0 \\ 0 & \boldsymbol{D}(t) & \cdots & 0 \\ \vdots & \vdots & \ddots & \vdots \\ 0 & 0 & \cdots & \boldsymbol{D}(t) \end{bmatrix},$$

and

$$\boldsymbol{A} = \begin{bmatrix} a_{00} & a_{01} & \cdots & a_{0N} & a_{10} & \cdots & a_{1N} & a_{N0} & \cdots & a_{NN} \end{bmatrix}^T,$$

such that $\overline{\boldsymbol{D}(t)}$ is spanned by $\boldsymbol{D}(t)$ with dimensional $1 \times N+1$.

Inserting properly the spatial delay $x \longrightarrow x-\tau_3$ and temporal delay $t \longrightarrow t-\tau_4$ into the matrix expansion (4), it holds

$$u(x-\tau_3, t-\tau_4) = \boldsymbol{D}(x-\tau_3)\overline{\boldsymbol{D}(t-\tau_4)}\boldsymbol{A}, \tag{5}$$

where

$$\boldsymbol{D}(x-\tau_3) = \begin{bmatrix} D_0(x-\tau_3) & D_1(x-\tau_3) & \cdots & D_N(x-\tau_3) \end{bmatrix},$$

and

$$\overline{\boldsymbol{D}(t-\tau_4)} = \begin{bmatrix} \boldsymbol{D}(t-\tau_4) & 0 & \cdots & 0 \\ 0 & \boldsymbol{D}(t-\tau_4) & \cdots & 0 \\ \vdots & \vdots & \ddots & \vdots \\ 0 & 0 & \cdots & \boldsymbol{D}(t-\tau_4) \end{bmatrix}.$$

Now, using the time fractional Caputo derivative operator in terms of α, which is of the form:

Definition 2.0.1 *[1] Suppose that $t > a$ and $\alpha, t \in \mathbb{R}$. Then the time fractional Caputo derivative of order α is defined to be*

$${}_t^C\mathcal{D}_0^\alpha u(x,t) = \begin{cases} \frac{1}{\Gamma(\lceil\alpha\rceil-\alpha)} \int_0^t (t-s)^{\lceil\alpha\rceil-\alpha-1} \left({}_sD^{\lceil\alpha\rceil}u(x,s)\right) ds, & \lceil\alpha\rceil - 1 < \alpha < \lceil\alpha\rceil \\ \partial^\alpha u(x,t)/\partial t^\alpha, & \alpha \in \mathbb{N} \end{cases}.$$

We can insert this operator on the matrix expansion (4) as

$${}_t^C\mathcal{D}_0^\alpha u(x,t) = \boldsymbol{D}(x)\overline{\boldsymbol{D}^{(\alpha)}(t)}\boldsymbol{A}, \ 1 < \alpha \leq 2, \tag{6}$$

where

$$\boldsymbol{D}^{(\alpha)}(t) = \begin{bmatrix} {}_t^C\mathcal{D}_0^\alpha(D_0(t)) & {}_t^C\mathcal{D}_0^\alpha(D_1(t)) & \cdots & {}_t^C\mathcal{D}_0^\alpha(D_N(t)) \end{bmatrix},$$

and

$$\overline{\boldsymbol{D}^{(\alpha)}(t)} = \begin{bmatrix} \boldsymbol{D}^{(\alpha)}(t) & 0 & \cdots & 0 \\ 0 & \boldsymbol{D}^{(\alpha)}(t) & \cdots & 0 \\ \vdots & \vdots & \ddots & \vdots \\ 0 & 0 & \cdots & \boldsymbol{D}^{(\alpha)}(t) \end{bmatrix}.$$

Using analogously the matrix expansions (5) and (6), we can write

$${}_t^C\mathcal{D}_0^\beta u(x-\tau_1, t-\tau_2) = \boldsymbol{D}(x-\tau_1)\overline{\boldsymbol{D}^{(\beta)}(t-\tau_2)}\boldsymbol{A}, \ 0 < \beta \leq 1, \tag{7}$$

where

$$\overline{\boldsymbol{D}^{(\beta)}(t-\tau_2)} = \begin{bmatrix} \boldsymbol{D}^{(\beta)}(t-\tau_2) & 0 & \cdots & 0 \\ 0 & \boldsymbol{D}^{(\beta)}(t-\tau_2) & \cdots & 0 \\ \vdots & \vdots & \ddots & \vdots \\ 0 & 0 & \cdots & \boldsymbol{D}^{(\beta)}(t-\tau_2) \end{bmatrix}.$$

In addition, by making use of the matrix expansion (4), we can inherently state the following matrix expansion with respect to the spatial partial derivative of integer order:

$$ {}_xD^2u(x,t) = \boldsymbol{D}^{(2)}(x)\overline{\boldsymbol{D}(t)}\boldsymbol{A}, \tag{8}$$

where

$$\boldsymbol{D}^{(2)}(x) = \begin{bmatrix} D_0^{(2)}(x) & D_1^{(2)}(x) & \cdots & D_N^{(2)}(x) \end{bmatrix}.$$

We are now ready to constitute a fundamental matrix form of the equation (1) by means of the matrix expansions (5)-(8). Thereby, collecting them under a unique form, it follows that

$$\boldsymbol{W}(x_i,t_j)\boldsymbol{A} = \boldsymbol{G}(x_i,t_j), \tag{9}$$

where

$$\boldsymbol{W}(x_i,t_j) = \left[\boldsymbol{D}(x_i)\overline{\boldsymbol{D}^{(\alpha)}(t_j)} + \boldsymbol{D}(x_i-\tau_1)\overline{\boldsymbol{D}^{(\beta)}(t_j-\tau_2)} + p_1\boldsymbol{D}(x_i-\tau_3)\overline{\boldsymbol{D}(t_j-\tau_4)} - p_2\boldsymbol{D}^{(2)}(x_i)\overline{\boldsymbol{D}(t_j)}\right],$$

and

$$\boldsymbol{G}(x_i,t_j) = \begin{bmatrix} G(x_0,t_0) & \cdots & G(x_0,t_N) & \cdots & G(x_N,t_0) & \cdots & G(x_N,t_N) \end{bmatrix}^T,$$

such that x_i and t_i are the Chebyshev-Lobatto collocation points on Ω defined to be (see [8])

$$x_i = \frac{a+b}{2} + \frac{a-b}{2}\cos\left(\frac{\pi i}{N}\right),\ t_j = \frac{c+d}{2} + \frac{c-d}{2}\cos\left(\frac{\pi j}{N}\right),\ i,j = 0,1,\ldots,N.$$

For more brief form of the matrix form (9), it can be summarized as

$$\boldsymbol{W}\boldsymbol{A} = \boldsymbol{G} \Rightarrow \left[\boldsymbol{W} \ : \ \boldsymbol{G}\right], \tag{10}$$

where

$$\boldsymbol{W} = \begin{bmatrix} W(x_0,t_0) & \cdots & W(x_0,t_N) & \cdots & W(x_N,t_0) & \cdots & W(x_N,t_N) \end{bmatrix}^T.$$

On the other hand, using the main matrix expansion (4), we can form the matrix expansions of the initial and boundary conditions at the Chebyshev-Lobatto collocation points, respectively, as

$$\begin{aligned} u(x_i, c) &= \boldsymbol{D}(x_i)\overline{\boldsymbol{D}(c)}\boldsymbol{A} = \lambda_1(x_i), \\ u(a, t_j) &= \boldsymbol{D}(a)\overline{\boldsymbol{D}(t_j)}\boldsymbol{A} = \lambda_2(t_j), \\ u(b, t_j) &= \boldsymbol{D}(b)\overline{\boldsymbol{D}(t_j)}\boldsymbol{A} = \lambda_3(t_j), \end{aligned} \tag{11}$$

where $i, j = 0, 1, \ldots, N$.

After replacing the conditional matrix expansions (11) by the last $3N + 3$ rows in the matrix system (10), we can now state the augmented matrix system as

$$\left[\widetilde{\boldsymbol{W}} : \widetilde{\boldsymbol{G}}\right] = \begin{bmatrix} \boldsymbol{W}^* & ; & \boldsymbol{G}^* \\ \boldsymbol{D}(x_i)\overline{\boldsymbol{D}(c)} & : & \lambda_1(x_i) \\ \boldsymbol{D}(a)\overline{\boldsymbol{D}(t_j)} & : & \lambda_2(t_j) \\ \boldsymbol{D}(b)\overline{\boldsymbol{D}(t_j)} & : & \lambda_3(t_j) \end{bmatrix},$$

where $\boldsymbol{W}^*$ and $\boldsymbol{G}^*$ are of $(N^2 - N - 2) \times 1$ matrix structures, this system is consistent as long as rank$\widetilde{\boldsymbol{W}}$= rank $\left[\widetilde{\boldsymbol{W}} : \widetilde{\boldsymbol{G}}\right] = (N + 1)^2$. If this situation is satisfied, then the system can be solved via Gaussian elimination method or

$$\boldsymbol{A} = \widetilde{\boldsymbol{G}}(\widetilde{\boldsymbol{W}})^{-1}, \ \det\widetilde{\boldsymbol{W}} \neq 0.$$

Eventually, the unknown Delannoy coefficients (z_{mn}) are obtained and then substituted into the solution form (3), the Delannoy polynomial solution of equation (1) is acquired.

3. Residual error computation

Formerly, the residual error analysis technique was employed to improve the approximate solutions of the space-time fractional PDEs involving multi delays [8] and one dimensional TDE of integer order [19]. In this paper, we shall construct a residual error computation based on the Delannoy polynomial. Basically, the residual error computation is made up of the same procedure as the proposed method and a residual function obtained by substituting the Delannoy polynomial solution into equation (1). A residual function corresponding to N can be described on Ω as

$$R_N(x, t) = {}_t^C\mathcal{D}_0^{\alpha} u_N(x, t) + {}_t^C\mathcal{D}_0^{\beta} u_N(x - \tau_1, t - \tau_2) + p_1 u_N(x - \tau_3, t - \tau_4) - p_{2\,x} D^2 u_N(x, t) - g(x, t). \tag{12}$$

After taking the initial and boundary conditions, the error problem can be stated as (see [8])

$$L[e_N(x, t)] = L[u(x, t)] - L[u_N(x, t)] = -R_N(x, t), \tag{13}$$

where $e_N(x, t)$ is an error function under the linear operator.

Equation (13) can be solved by following the algorithmic structure of the proposed method. Then, the estimated error function $e_{N,K}(x, t)$ is derived by

$$e_{N,K}(x, t) = \sum_{m=0}^{K}\sum_{n=0}^{K} z_{mn}^* D_m(x) D_n(t), \ K > N,$$

and using this function, the corrected Delannoy polynomial solution and the corrected error function can be constructed, respectively, as

$$u_{N,K}(x,t) = u_N(x,t) + e_{N,K}(x,t) \text{ and } E_{N,K}(x,t) = u(x,t) - u_{N,K}(x,t).$$

4. Numerical problems

In this section, three problems are dealt numerically with the proposed method. To do this, a practical module is uniquely devised on Mathematica 11.3 run on a standard personal computer with 6 GB RAM and 2.50 GHz i5-2450M CPU. For this clearness, the computation results can be acquired sensitively from the mentioned problems. In addition, graphical and numerical tools, such as a root mean squared error (E_{RMS}) computation, are deployed to interpret the precision and accuracy of the method. E_{RMS} is formulated as follows [21]:

$$E_{RMS} = \sqrt{\frac{1}{N}\sum_{i=0}^{N}[u(x_i,T) - u_N(x_i,T)]^2},$$

where $u(x_i,T)$ and $u_N(x_i,T)$ are the exact and Delannoy polynomial solutions at the spatial collocation points x_i and specific time T, respectively.

Problem 4.1. [3, 16, 17] Consider the time fractional TDE having non-polynomial exact solution

$${}_t^C\mathcal{D}_0^{\alpha}u(x,t) + {}_t^C\mathcal{D}_0^{\beta}u(x,t) + u(x,t) = {}_xD^2u(x,t) + g(x,t),$$

with $1 < \alpha \leq 2$, $0 < \beta = \alpha - 1 \leq 1$ and $\Omega = [0,1]^2$,

subject to the initial condition $u(x,0) = x\cos(x^2)$ in Ω and boundary conditions $u(0,t) = 0$ and $u(1,t) = \cos(1+t^2)$ on $\partial\Omega$. The exact solution is formulated as $u(x,t) = x\cos(x^2+t^2)$. The force function $g(x,t)$ can be easily determined in accordance with α. Solving this problem by employing the proposed method, the Delannoy polynomial solutions are acquired. At first, the solution $u_{13}(x,t)$ is demonstrated along with its contour curves, which represent the absolute error values, in Figure 1. From Figure 1, this solution takes five decimal accuracies (10^{-5}). Besides, Table 1 compares the computation results of E_{RMS} in terms of the proposed (PM), the local meshless (LMM) [16], the radial basis function (RBF) [3] and the reproducing kernel (RKM) [17] methods. It can be noticed from Table 1 that the proposed method achieves far more accurate approximation than the other methods with respect to the low computation limit (N) and each specified fractional derivative. Also, in Table 2, the proposed method ($N = 20$) takes 10^{-9} of accuracy, while RKM ($h = 0.001$) [17] enables 10^{-5} of accuracy on average.

Table 1. *Numerical computation results of E_{RMS} at $T = 1$ with respect to the proposed and existing methods for Problem 4.1.*

Methods	$\alpha = 1.25$	$\alpha = 1.5$	$\alpha = 1.75$	$\alpha = 1.95$
PM ($N = 20$)	2.1583e–12	5.2895e–12	1.9302e–13	2.7054e–10
LMM ($M = 50$) [16]	2.2992e–05	1.0880e–04	6.8631e–04	2.4189e–03
RBF ($N = 50$) [3]	2.6551e–03	4.1743e–03	5.4164e–03	3.8800e–03
RKM ($h = 0.001$) [17]	-	-	-	4.3309e–04

Problem 4.2. [16] Consider the time fractional TDE having non-polynomial exact solution

$${}_t^C\mathcal{D}_0^{\alpha}u(x,t) + {}_t^C\mathcal{D}_0^{\beta}u(x,t) + u(x,t) = {}_xD^2u(x,t) + g(x,t),$$

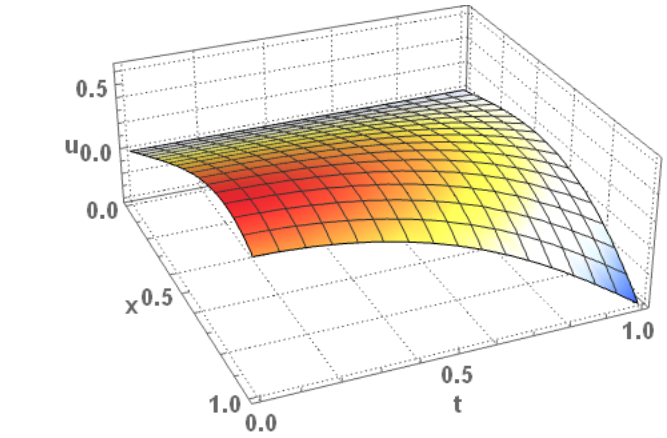

(a) $u_{13}(x, t)$

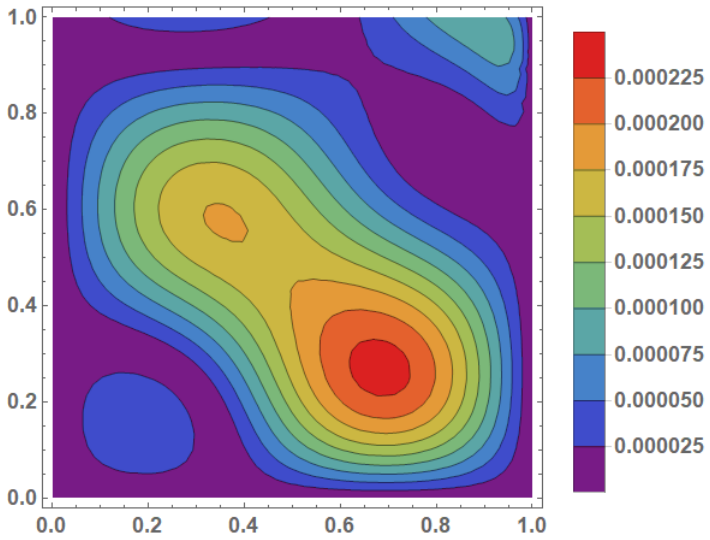

(b) The absolute error plot via contour curves

Figure 1. *The Delannoy polynomial solution and its error plot for Problem 4.1 having $\alpha = 1.9$ and $\beta = 0.9$.*

Table 2. *Absolute error history in terms of PM and RKM for Problem 4.1 having $\alpha = 1.95$.*

x_i	t_i	$\lvert e_{20}(x_i, t_i)\rvert$ $N = 20$	RKM $h = 0.001$ [17]
0.1	0.1	$3.69731e-10$	$1.49994e-07$
0.2	0.2	$1.33009e-09$	$2.39840e-06$
0.3	0.3	$2.75515e-09$	$1.21090e-05$
0.4	0.4	$4.15103e-09$	$3.79919e-05$
0.5	0.5	$4.46054e-09$	$9.13299e-05$
0.6	0.6	$3.41082e-09$	$1.84091e-04$
0.7	0.7	$1.89897e-09$	$3.25310e-04$
0.8	0.8	$7.62644e-10$	$5.15381e-04$
0.9	0.9	$1.40729e-10$	$7.38682e-04$
1.0	1.0	$9.33087e-13$	$9.56449e-04$

with $1 < \alpha \leq 2$, $0 < \beta = \alpha - 1 \leq 1$, $\Omega = [0,1]^2$ and

$$g(x,t) = \sin^2 x \left(\frac{6t^{3-\alpha}}{\Gamma(4-\alpha)} + \frac{6t^{4-\alpha}}{\Gamma(5-\alpha)} \right) - 2t^3 \cos 2x + t^3 \sin^2 x,$$

subject to the initial condition $u(x,0) = 0$ and boundary conditions $u(0,t) = 0$ and $u(1,t) = t^3 \sin^2 1$. The exact solution of the problem is given as $u(x,t) = t^3 \sin^2 x$. The problem is immediately and accurately solved by the proposed method for different N and α. As seen in Figure 2, the Delannoy polynomial solution $u_{10}(x,t)$ has a good approximation to the exact solution, yielding 10^{-8} of accuracy for $\alpha = 1.7$. Besides, Table 3 reveals that the proposed method (PM) performs much more accurate computations than LMM [16], as well as much faster. It is explicit to say from Figure 3 that the L_2 and L_∞ errors are decreased when N increases and so this situation confirms the precision of the method in accordance with the results given in Table 3.

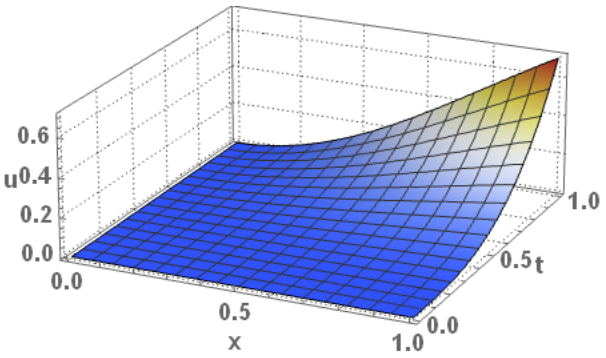

(a) $u_{10}(x,t)$

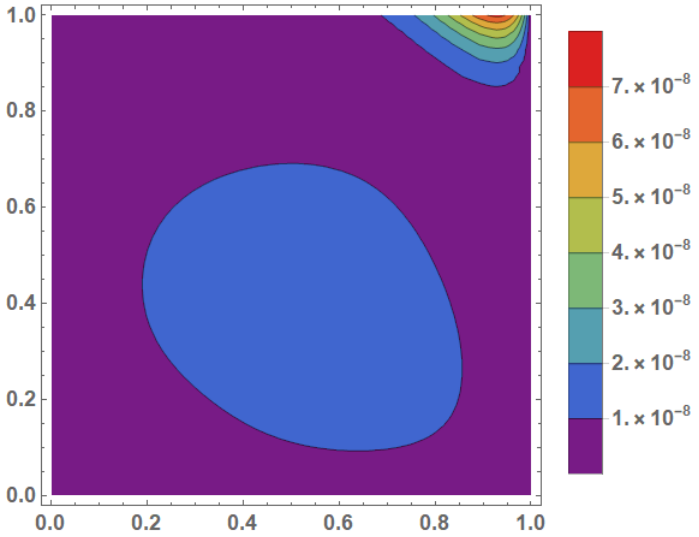

(b) The absolute error plot via contour curves

Figure 2. *The Delannoy polynomial solution and its error plot for Problem 4.2 having $\alpha = 1.7$ and $\beta = 0.7$.*

Problem 4.3. Consider the time fractional TDE with multiple space and time delays

$${}_t^C\mathcal{D}_0^{1.6} u(x,t) + {}_t^C\mathcal{D}_0^{0.9} u(x-1,t-1) + 0.3u(x-0.5,t-0.1) = 0.5\, {}_xD^2 u(x,t) + g(x,t),$$

with $\Omega = [0,1]^2$ and

Table 3. *Numerical comparisons of E_{RMS} (at $T = 1$) and CPU running time (in seconds) in terms of PM and LMM for Problem 4.2 having $\alpha = 1.9$.*

PM			LMM [16] m & $N = 1000$		
N	E_{RMS}	Timing	m	E_{RMS}	Timing
6	4.0353e–05	0.906	3	6.5786e–05	34.249
7	2.8692e–05	1.250	7	6.5785e–05	35.542
9	5.0556e–07	2.359	9	6.5804e–05	37.021
11	3.2466e–09	4.672	11	6.5794e–05	37.380
13	1.8760e–09	9.625	15	6.5796e-05	38.332

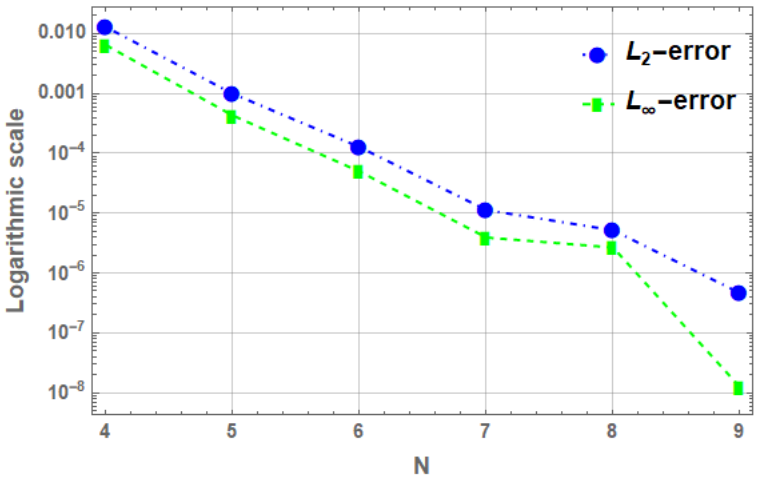

Figure 3. *The decreasing error computations on logarithmic scale versus N for Problem 4.2 having $\alpha = 1.2$.*

$$g(x,t) = e^t(-0.135726 + 0.271451x + t^{0.1}(-0.386692 + 0.386692x)\,{}_1F_1(0.1; 1.1; -t) + 1.12706xt^{0.4}\,{}_1F_1(0.4; 1.4; -t)),$$

such that ${}_1F_1(a_1;\, a_2;\, t)$ is the confluent hypergeometric function of Kummer type [35],

subject to the initial condition $u(x,0) = x$ and boundary conditions $u(0,t) = 0$ and $u(1,t) = e^t$. The exact solution of the problem is $u(x,t) = xe^t$. After solving this problem by arranging $N = 4(1)11$ in the method, the Delannoy polynomial solution is illustrated along with its contour curves specifying 10^{-9} of accuracy in Figure 4. Besides, Figure 5 indicates the L_2 and L_∞ error computations and CPU running time versus N. It is worth clarifying from Figure 5 that the method gets much clearer precision to the exact solution and returns the solutions by consuming short time at most 12 seconds, as N is increased from 4 to 11. On the other hand, the Delannoy polynomial solution for $N = 6$ is easily improved by employing the residual error computation with its limit $N = 7$, as seen in Table 4.

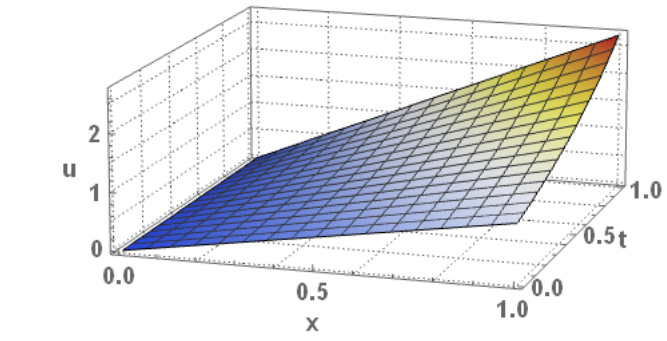

(a) $u_{11}(x,t)$

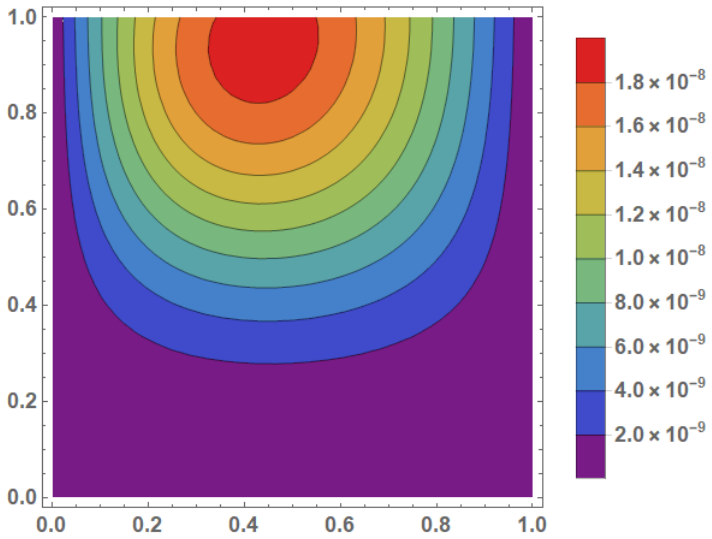

(b) The absolute error plot via contour lines

Figure 4. *The Delannoy polynomial solution and its error plot for Problem 4.3.*

5. Conclusions

A novel matrix-collocation method dependent on the Delannoy polynomial has been productively implemented to treat the time fractional telegraph differential equations of space and time delays. To do this, the inventive and pure matrix structures containing the fractional derivative forms have been developed to easily extend the functions in equation (1)

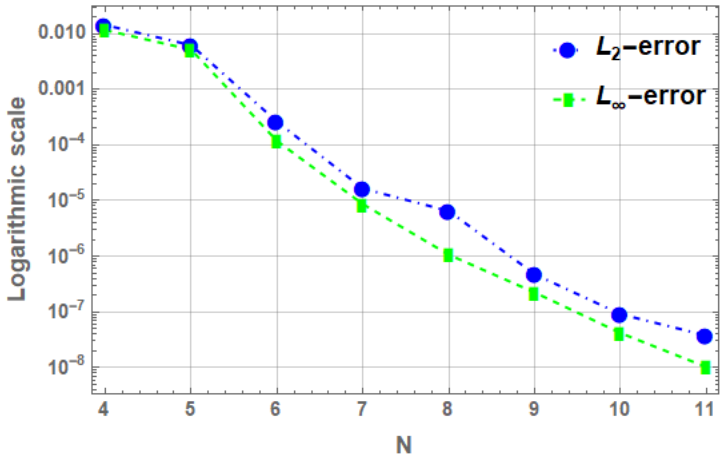

(a) The error computations on logarithmic scale

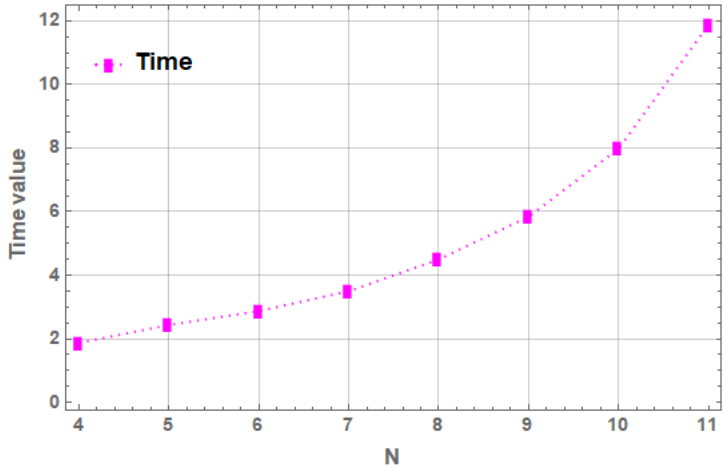

(b) CPU running time

Figure 5. *Displacements of the error computations and timing tool versus N for Problem 4.3.*

Table 4. *History of the absolute and corrected absolute error results for Problem 4.3.*

(x_i, t_i)	$\lvert e_6(x_i, t_i)\rvert$	$\lvert E_{6,7}(x_i, t_i)\rvert$
(0.2, 0.2)	3.4034e–05	1.9525e–05
(0.4, 0.4)	9.2624e–05	6.2166e–05
(0.6, 0.6)	1.1806e–04	1.0044e–04
(0.8, 0.8)	1.0941e–04	8.3094e–05

using the collocation points. With the involvement of the Delannoy polynomial in these matrix profiles, the proposed method has enabled to obtain persistent numerical solutions, which are often in good agreement with the analytical solutions corresponding to the specific problems. In addition, as noticed in the error and time complexity comparisons given in Tables 1, 2 and 3, the method has yielded very remarkable results compared to the existing methods. As N increases, the precision of the method becomes much clear as in Table 3, Figures 3 and 5.

When all computations are investigated, the findings reveal that the method is very competitive and provides a novel approximation into the literature by treating the delay form of TDEs. In fact, we can specify that the method would be applicable tool for some generations of the fractional partial differential equations. Inherently, this specification is regarded as a next vision for incoming works.

References

[1] Caputo, M., Elasticità e Dissipazione, Bologna, Zanichelli, 1969.

[2] Moaddy, K., Momani, S., Hashim, I., The non-standard finite difference scheme for linear fractional PDEs in fluid mechanics, Comput. Math. Appl., 61, (2011), 1209–1216.

[3] Hosseini, V.R., Chen, W., Avazzadeh, Z., Numerical solution of fractional telegraph equation by using radial basis functions, Eng. Anal. Bound. Elem., 38, (2014), 31–39.

[4] Faraji, M, Ansari, O.R., Linear and nonlinear vibrations of fractional viscoelastic Timoshenko nanobeams considering surface energy effects, Appl. Math. Model., 43, (2017), 337–350.

[5] Arqub, O.A., Numerical solutions for the Robin time-fractional partial differential equations of heat and fluid flows based on the reproducing kernel algorithm, Int. J. Numer. Method H., 28(4), (2018), 828–856.

[6] Koleva, M.N., Vulkov, L.G., Numerical solution of time-fractional Black–Scholes equation, Comp. Appl. Math., 36, (2017), 1699–1715.

[7] Soori, Z., Aminataei, A., A new approximation to Caputo-type fractional diffusion and advection equations on non-uniform meshes, Appl. Numer. Math., 144, (2019), 21–41.

[8] Kürkçü, Ö.K., Aslan, E., Sezer, M., An advanced method with convergence analysis for solving space-time fractional partial differential equations with multi delays, Eur. Phys. J. Plus, 134, (2019), 393.

[9] Dehestani, H., Ordokhani, Y., Razzaghi, M., A numerical technique for solving various kinds of fractional partial differential equations via Genocchi hybrid functions, Rev. R. Acad. Cienc. Exactas, Fis. Nat. Madr., 113, (2019), 3297–3321.

[10] Rihan, F.A., Computational methods for delay parabolic and time-fractional partial differential equations, Numer. Methods Partial Differ. Equ., 26, (2010), 1556–1571.

[11] Usman, M., Hamid, M., Zubair, T., Haq, R.U., Wang, W., Liu, M.B., Novel operational matrices-based method for solving fractional-order delay differential equations via shifted Gegenbauer polynomials, Appl. Math. Comput., 372, (2020), 124985.

[12] Pozar, D.M., Microwave Engineering in Addison-Wesley, 1990.

[13] Mainardi, F., Paradisi, P., Fractional diffusive waves, J. Comput. Acoust., 9(4), (2001), 1417–1436.

[14] Abdou, M.A., Adomian decomposition method for solving the telegraph equation in charged particle transport, J. Quant. Spectrosc. Radiat. Transf., 95, (2005), 407–414.

[15] Orsingher, E., Beghin, L., Time-fractional telegraph equations and telegraph processes with brownian time, Probab. Theory Relat. Fields, 128, (2004), 141–160.

[16] Kumar, A., Bhardwaj, A., Dubey, S., A local meshless method to approximate the time-fractional telegraph equation, Eng. Comput., (2020), https://doi.org/10.1007/s00366-020-01006-x.

[17] Wang, Y.L., Du, M.-J., Temuer, C.-L., Tian, D., Using reproducing kernel for solving a class of time-fractional telegraph equation with initial value conditions, Int. J. Comput. Math., 95(8), (2018), 1609–1621.

[18] Pandey, R.K., Mishra, H.K., Numerical simulation for solution of space-time fractional telegraphs equations with local fractional derivatives via HAFSTM, New Astronomy, 57, (2017), 82–93.

[19] Yüzbaşı, Ş., Karaçayır, M., A Galerkin-type method to solve one-dimensional telegraph equation using collocation points in initial and boundary conditions, Int. J. Comput. Methods, 15(1), (2018), 1850031, (16 pages).

[20] Dehghan, M., Shokri, A., A numerical method for solving the hyperbolic telegraph equation, Numer. Methods Partial Differ. Equ., 24, (2008), 1080–1093.

[21] Dehghan, M., Lakestani, M., The use of Chebyshev cardinal functions for solution of the second-order one-dimensional telegraph equation, Numer. Methods Partial Differ. Equ., 25, (2009), 931–938.

[22] Pandit, S., Kumar, M., Tiwari, S., Numerical simulation of second-order hyperbolic telegraph type equations with variable coefficients, Comput. Phys. Commun., 187, (2015), 83–90.

[23] Sharifi, S., Rashidinia, J., Numerical solution of hyperbolic telegraph equation by cubic B-spline collocation method, Appl. Math. Comput., 281, (2016), 28–38.

[24] Delannoy, H., Emploi de l'echiquier pour la resolution de certains problμemes de probabilites, Assoc. Franc. Bordeaux, 24, (1895), 70–90.

[25] Banderier, C., Schwer, S., Why Delannoy numbers?, J. Stat. Plan. Infer., 135(1), (2005), 40–54.

[26] Weisstein, E.W., Delannoy Number, from MathWorld–A Wolfram Web Resource, https://mathworld.wolfram.com/DelannoyNumber.html.

[27] Comtet, L., Advanced Combinatorics: The Art of Finite and Infinite Expansions, Rev. enl. ed. Dordrecht, Netherlands, Reidel, (1974), 80-81.

[28] Sulanke, R.A., Objects counted by the central Delannoy numbers, J. Integer Seq., 6, (2003), Article 03.1.5.

[29] Peart, P., Woan, W.-J., A bijective proof of the Delannoy recurrence, Congressus Numerantium, 158, (2002), 29–33.

[30] Hetyei, G., Shifted Jacobi polynomials and Delannoy numbers, (2009), ArXiv e-prints arXiv:0909.5512v2.

[31] Sun, Z., Congruences involving generalized central trinomial coefficients, Sci. China Math., 57, (2014), 1375–1400.

[32] Sun, Z.-W., On Delannoy numbers and Schröder numbers, J. Number Theory, 131, (2011), 2387–2397.

[33] Torres, A., Cabada, A., Nieto, J.J., An exact formula for the number of alignments between two DNA sequences, DNA Seq., 14, (2003), 227–430.

[34] Guo, V.J.W., Zeng, J., Proof of some conjectures of Z.-W. Sun on congruences for Apery polynomials, J. Number Theory, 132, (2012), 1731–1740.

[35] Abramowitz, M., Stegun, I.A., Handbook of Mathematical Functions, with Formulas, Graphs, and Mathematical Tables, Nat. Bureau of Standards, Appl. Math. Series, 55, 1964.